Experimental analysis of mass transfer of Taylor bubble flow in small channels

von der Fakultät Maschinenwesen

der Technischen Universität Dresden

zur Erlangung des akademischen Grades

Doktoringenieur (Dr.-Ing.)

genehmigte Dissertation

von

M.Sc. Mohammadreza Haghnegahdar

geboren am 06. November 1984 in Shiraz Iran

Dresden 2018

Abstract

Multiphase flows in chemical reactors with micro- and millimeter-size channel structures such as monolith froth reactors, compact heat exchangers and fuel cells have received great attention in the last years. They are considered as a promising alternative to conventional reactors, such as fixed bed reactors and bubble columns which are mainly used for gas absorption, catalytic hydrogenation and biochemical conversions. Slug or Taylor bubble flow is a desired operating state for this type of contactors due to the frequent change of efficient gas-liquid contacting in the film around the bubbles and the enhanced mixing in the liquid slugs behind the bubbles. Consequently, capillary Taylor flow is currently a target of intensive investigations. However, a full understanding of design parameters and optimum operating conditions are still lacking.

For milli- and microreactors mass transfer between gas and liquid phases depends upon various parameters such as bubble shape, relative velocity between the two phases, degree of liquid contamination and many more. To further advance the fundamental understanding of micro- and milli-channel reactors with Taylor flow, main design parameters and operating conditions were investigated, which include (a) the effect of bubble size, channel diameter and cross sectional shape of channel on the mass transfer coefficient of dissolving bubbles, (b) the influence of the presence of surface active agents on the bubble shape, velocity and also on the mass transfer rate of bubbles and (c) the intensification effect of oscillation of channels on the mass transfer performance of Taylor bubbles.

For the study of gas-liquid mass transfer high-resolution X-ray radiography and tomography were used as measurement techniques. The X-ray imaging methods were chosen as their accuracy is less affected by changes in the refractive index, as it is the case for conventional optical methods. The mass transfer was calculated by measuring the changes in the size of the bubbles at constant pressure. The utilization of X-ray visualization enabled the acquisition of a series of radiographic images of bubbles. The images gave the volume, interfacial area and length of the bubble with high accuracy as a function of time and were used to evaluate the mass transfer coefficient using the mass conservation equations.

In case of circular channels, the results show that Sherwood numbers have a large dependency on the bubble length and also equivalent diameter which is in accordance with previous results for larger channel diameters. However, the values of measured Sherwood numbers could not be predicted by available correlations which are valid only for larger pipes. As a result, a new mass transfer correlation in the form of Sherwood number as a function of Peclet number as well as bubble size ratio was derived. The proposed correlation is applicable for a large range of bubble sizes with high accuracy.

The comparison of the results for the square and circular channels showed that despite the fact that the rise velocity of bubbles in the square channel is about three times higher than in the circular channel, the mass transfer coefficient is about the same. Furthermore, the results show that in square channels the dissolution curves are relatively even, while the dissolution curves of circular channels exhibit some distinguishable change in the slope. In addition, the results show that the calculated mass transfer coefficient based on the measured data show good agreement with the data predicted by the penetration theory.

Regarding the influence of surfactants on the mass transfer in small channels with Taylor flow, it was shown that a small amount of surfactant reduces the mass transfer and its impact is more pronounced on small bubbles. Furthermore, it was demonstrated that the presence of surfactants causes the change of the bubble shape and leads to a slight increase of the liquid film thickness around the bubble and as a result the elongation of contaminated bubbles.

Intensification of mass transfer in small channels with Taylor bubbles was investigated by measuring the motion, shape and dissolution rate of individual elongated Taylor bubbles of air and CO_2 in water. The comparison of the results for the stationary and oscillating channel showed that mechanical vibration of the channel is able to enhance the mass transfer coefficient from 80% to 186%. Moreover, the mass transfer rate positively correlates with frequency and amplitude of oscillation, which is more pronounced at higher amplitudes. In addition, it was shown that the intensification of mass transfer with increase of amplitude/frequency of vibration is mainly attributed to the increase of bubble surface wave oscillations that causes an enlargement of contact area between the phases and also a reduction of mass transfer resistance in the liquid-side boundary layer.

Major results of this doctoral work have been published in peer-reviewed journals (see list of publications).

Keywords: mass transfer coefficient, Taylor bubble, small channel, microfocus X-ray technique, liquid film thickness, surfactant, channel vibration

Kurzbeschreibung

Mehrphasenströmungen in chemischen Reaktoren mit mikro- und millimetergroßen Kanalstrukturen wie Monolithschaumreaktoren, kompakten Wärmetauschern und Brennstoffzellen haben in den letzten Jahren große Aufmerksamkeit erfahren. Sie gelten als eine vielversprechende Alternative zu herkömmlichen Reaktoren, wie Festbettreaktoren und Blasensäulen, die hauptsächlich für die Gasabsorption, katalytische Hydrierung und biochemische Umwandlungen verwendet werden. Die Pfropfen- oder Taylorblasenströmung ist ein erwünschter Betriebszustand für diese Art von Reaktoren aufgrund des häufigen Wechsels des wirksamen Gas-Flüssigkeits-Kontakts in dem Film um die Blasen und des verstärkten Mischens in den Flüssigkeitspfropfen hinter den Blasen. Folglich ist die Kapillar-Taylorströmung gegenwärtig Gegenstand intensiver Forschungen. Ein umfassendes Verständnis der Designparameter und der optimalen Betriebsbedingungen fehlt jedoch noch.

Für Milli- und Mikroreaktoren hängt der Stofftransport zwischen Gas- und Flüssigkeitsphasen von verschiedenen Parametern wie Blasenform, Relativgeschwindigkeit zwischen den beiden Phasen, Grad der Flüssigkeitskontamination und vielem mehr ab. Um das grundlegende Verständnis von Mikro- und Milli-Kanal-Reaktoren mit Taylorströmung weiter voranzutreiben, wurden die wichtigsten Designparameter und Betriebsbedingungen untersucht, darunter (a) der Einfluss der Blasengröße, des Kanaldurchmessers und der Querschnittsform des Kanals auf den Stoffübergangskoeffizienten, (b) der Einfluss der Anwesenheit von oberflächenaktiven Stoffen auf die Blasenform, -geschwindigkeit und auch auf die Stofftransportrate der Blasen und (c) der Verstärkungseffekt der Oszillation von Kanälen auf die Stofftransportleistung von Taylorblasen.

Für die Untersuchung des Stofftransports von den Taylorblasen zu den Flüssigkeitspfropfen wurde die hochauflösende Röntgenradiographie und -tomographie als Messtechnik verwendet. Die Röntgenmethode wurde gewählt, da sie weniger durch Brechungsindexänderungen beeinträchtigt wird. Daher ist sie im Vergleich zu herkömmlichen optischen Mess- und Bildgebungsverfahren am genauesten. Der Stofftransport wurde berechnet, indem die Größenänderungen der Blasen bei konstantem Druck gemessen wurden. Die Verwendung der Röntgenvisualisierung ermöglichte die Erfassung einer Reihe von Röntgenbildern der Blasen. Die Bilder gaben das Volumen, die Grenzfläche und die Länge der Blase mit hoher Genauigkeit als eine Funktion der Zeit und wurden verwendet, um den Stofftransportkoeffizienten unter Verwendung der Massenerhaltungsgleichungen zu bewerten.

Im Fall von runden Kanälen zeigen die Ergebnisse, dass die Sherwood-Zahlen eine große Abhängigkeit von der Blasenlänge und auch dem äquivalenten Durchmesser haben, was in

Übereinstimmung mit früheren Ergebnissen für größere Kanaldurchmesser ist. Jedoch konnten die Werte der gemessenen Sherwood-Zahlen nicht durch verfügbare Korrelationen vorhergesagt werden, die nur für größere Rohre gültig sind. Als Ergebnis wurde eine neue Stofftransportkorrelation in Form der Sherwood-Zahl als Funktion der Peclet-Zahl sowie des Blasengrößenverhältnisses abgeleitet. Die vorgeschlagene Korrelation ist für einen großen Bereich der Blasengrößen mit hoher Genauigkeit anwendbar.

Der Vergleich der Ergebnisse für die quadratischen und runden Kanäle zeigte, dass trotz der Tatsache, dass die Aufstiegsgeschwindigkeit der Blasen im quadratischen Kanal etwa dreimal höher ist als im runden Kanal, der Stofftransportkoeffizient ungefähr gleich ist. Außerdem zeigen die Ergebnisse, dass in quadratischen Kanälen die Auflösungskurven relativ gleichmäßig sind, während die Auflösungskurven von runden Kanälen eine unterscheidbare Änderung der Steigung zeigen. Darüber hinaus zeigen die Ergebnisse, dass der berechnete Stofftransportkoeffizient basierend auf den gemessenen Daten eine gute Übereinstimmung mit den von der Penetrationstheorie vorhergesagten Daten zeigt.

Im Hinblick auf den Einfluss von Surfactants auf den Stofftransport in kleinen Kanälen mit Taylorströmung wurde gezeigt, dass eine geringe Menge an Surfactant den Stofftransport reduziert und seine Auswirkung auf kleine Blasen stärker ausgeprägt ist. Darüber hinaus wurde gezeigt, dass die Anwesenheit von Surfactants die Veränderung der Blasenform bewirkt und zu einem leichten Anstieg der Flüssigkeitsfilmdicke um die Blase herum und als Folge zur Verlängerung der kontaminierten Blasen führt.

Die Verstärkung des Stofftransports in kleinen Kanälen mit Taylorblasen wurde untersucht, indem die Bewegung, Form und Auflösungsgeschwindigkeit einzelner lang gestreckter Taylorblasen aus Luft und CO_2 im Wasser gemessen wurde. Der Vergleich der Ergebnisse für den stationären und den oszillierenden Kanal zeigte, dass mechanische Schwingungen des Kanals den Stoffübergangskoeffizienten von 80% bis 186% erhöhen können. Darüber hinaus korreliert die Stofftransportrate positiv mit der Frequenz und Amplitude der Oszillation, was bei höheren Amplituden ausgeprägter ist. Zusätzlich wurde gezeigt, dass die Verstärkung des Stofftransports mit der Erhöhung der Vibrationsamplitude und -frequenz hauptsächlich auf die Zunahme der Oszillationen der Blasenoberflächenwellen zurückzuführen ist, die eine Vergrößerung der Kontaktfläche zwischen den Phasen und auch eine Verringerung des Stoffübergangswiderstandes in der flüssigkeitsseitigen Grenzschicht verursacht.

Wesentliche Ergebnisse dieser Arbeit wurden in referierten Fachzeitschriften veröffentlicht (siehe Liste der Publikationen).

VI

Acknowledgments

I would like to take this opportunity to express my gratitude to all those who offered me their help in any way during the entire course of my graduate study.

I would like to express my special appreciation and thanks to my advisor Prof. Dr.-Ing. habil. Uwe Hampel, who has been a tremendous mentor for me. I would like to thank him for encouraging my research and for allowing me to grow as a research scientist. Meanwhile, I deeply appreciate all the time and attention he devoted, all the suggestions and ideas he provided in supervising me.

My sincere thank also goes to Dr. Stephan Boden for his continuous supports, motivation and his priceless guidance and comments that without his precious supports it would not have been possible to conduct this research.

I am grateful that Prof. Dr.-Ing. habil. J. Brandner agreed to be my co-examiner immediately and I really appreciate his time, devotion and expertise. Furthermore, I would like to thank Prof. Dr.-Ing. habil. R. Lange for his approval as examiner.

I would like to thank Dr. Markus Schubert for his help and suggestions during my work. I appreciate the excellent work of our lab manager Mr. Eckhard Schleicher for his assistance in this project.

My sincere thanks also go to all the doctoral students as well as all the members who work in Institute of Fluid Dynamics at Helmholtz-Zentrum Dresden-Rossendorf for such a pleasant, friendly and helpful working atmosphere.

Last but not least, I would like to thank my family: My parents, my sister and brothers for their continuous supports with endless love. At the end, I would like to express appreciation to my beloved wife, for her loving kindness and support throughout all the years of my education.

Table of contents

X

Nomenclature

Dimensionless groups

Bo	Bond number ($=\rho g D^2 / \sigma$)	
Ca	capillary number ($=\mu U_b / \sigma$)	
Eo	Eötvös number ($=\Delta\rho g D^2 / \sigma$)	
La	Langmuir number ($=C_s \beta / \alpha$)	
Pe	Peclet number ($=d_{eq} U_b / D_c$)	
Pe_D	Peclet number ($=D U_b / D_c$)	
Re	gas Reynolds number ($=\rho d_{eq} U_b / \mu$)	
Re_L	liquid Reynolds number ($=\rho d_{eq} U_L / \mu$)	
Sc	Schmidt number ($=\mu / \rho_L D_c$)	
Sh	Sherwood number ($=d_{eq} k_L / D_c$)	
Sh^*	modified Sherwood number ($=A_{eq} k_L / D_c D$)	
We	Weber number ($=\rho d_{eq} U_b^2 / \sigma$)	

Notations

a	specific interfacial area	1/m
A	amplitude of channel vibration	mm
a_{air}	angle of incidence of laser at the surface of air	deg
A_{eq}	bubble surface area based on d_{eq}	mm^2
a_f	flow acceleration	m/s^2
a_L	angle of incidence of laser at the surface of liquid	deg
A_L	available cross sectional area for the liquid between the bubble and the channel wall	mm^2
$a_0 \ldots a_{20}$	polynomial coefficients	-
C	concentration of gas in the liquid bulk	mol/m^3
C_L	water molar concentration	mol/m^3
C_s	concentration of surfactant in the liquid bulk	mol/m^3
C^*	concentration of gas at interface	mol/m^3
d	bubble diameter	mm
D	channel diameter	mm
D_c	gas molecular diffusion coefficient	m^2/s
d_{cc}	distance between the X-ray source and the nearest channel wall	mm
d_{cd}	distance between the X-ray source and the detector	mm

XII

d_{ch}	distance between the X-ray source and the furthest internal channel wall	mm
d_{eq}	sphere-volume equivalent bubble diameter	mm
d_{max}	bubble diameter at its maximum cross section in the channel	mm
dev_{max}	the maximum deviation in absolute distance between the interface sampling points extracted from the x-ray images and their nearest points on the fitted polynomial curve	mm
D_h	channel hydraulic diameter	mm
E	radiographic extinction image	-
E_b	radiographic extinction image of bubble only	-
E_g	radiographic extinction image of a bubble in the liquid-filled tube	-
E_{ref}	radiographic extinction image of liquid-filled tube	-
f	channel vibration frequency	Hz
g	gravitational acceleration	m/s^2
h	distance from the liquid surface	m
H	Henry's constant	MPa
h_{eva}	evaporation heat transfer coefficient	W/m^2.K
I	X-ray intensity	W/m^2
$I(L/D)$	integral function	-
K	thermal conductivity of liquid phase	W/m.K
k_L	liquid-side mass transfer coefficient	m/s
$k_L a$	liquid-side volumetric mass transfer coefficient	1/m
k_s	calibration function	-
$k_{s,3D}$	calibration function for square channel	-
k_v	calibration function	-
$k_{v,3D}$	calibration function for square channel	-
L	bubble length	mm
L_c	channel length	mm
l_{px}	pixel length	mm
M	magnification ratio	-
n	total moles of gas inside the bubble	mol
n_{air}	refractive index of air	-
n_L	refractive index of liquid	-
n_w	refractive index of channel wall	-
P	pressure inside the bubble	Pa
P_{atm}	atmospheric pressure	Pa
Q_L	liquid flow rate	m^3/s

Nomenclature

r	radial coordination	-
r_b	bubble radius	mm
r_c	channel radius	mm
R	universal gas constant	$Pa.m^3/mol.K$
R_{dia}	dimensionless bubble radius in diagonal direction	-
R_{lat}	dimensionless bubble radius in lateral direction	-
$s_{\sum E_b}$	standard deviation of the integral extinction signal	-
S_b	measured interfacial area of bubble	mm^2
$S_{b,2D}$	measured bubble interfacial area obtained from the radioscopic two-dimensional diagonal projection images	mm^2
$S_{b,3D}$	measured interfacial area of bubble for square channel	mm^2
S_e	surface coverage ratio	-
t	time	s
T	gas temperature in bubble	K (or °C)
t_c	contact time between gas and liquid	s
U_b	bubble terminal velocity	m/s (or mm/s)
U_L	mean velocity of liquid phase	m/s
u_r	relative velocity between the bubble and liquid in the channel	m/s
V_b	measured bubble volume	mm^3 (or ml)
$V_{b,2D}$	measured bubble volume obtained from the radioscopic two-dimensional diagonal projection images	mm^3
$V_{b,3D}$	measured bubble volume for square channel	mm^3
V_0	bubble initial volume	mm^3 (or ml)
W	partial amount of liquid remained on the internal surface of tube	-
x	lateral direction	-
y	lateral direction	-
y	mole fraction of CO_2 in the gas phase	-
z	axial direction	-

Greek symbols

α	desorption rate constant	1/s
β	adsorption rate constant	$m^3/mol.s$
δ	liquid film thickness	mm
μ	liquid dynamic viscosity	Pa.s
μd	radiographic attenuation	-
ρ_L	liquid density	Kg/m^3
σ	surface tension of liquid	N/m

XIV

Abbreviations

ANKA	Angströmquelle Karlsruhe (synchrotron light source facility at the Karlsruhe Institute of Technology)
CCD	charged coupled device
CFD	computational fluid dynamics
CMC	critical micelle concentration
DEA	diethanolamine
DNS	direct numerical simulation
FFT	fast Fourier transformation
HPTS	8-Hydroxypyrene-1,3,6-Trisulfonic Acid, Trisodium Salt (Pyranine)
LCDM	laser confocal displacement meter
LIF	laser-induced fluorescence
LSM	laser scanning microscopy
PEG	polyethylene glycol
PIV	particle imaging velocimetry
PLIFI	planar laser induced fluorescence
SDS	sodium dodecyl sulfate
TOC	total organic carbon
TOPO/TOMO	topography, microradiology and microtomography using polychromatic light and X-rays

1. Introduction

1.1.   Introduction and motivation

Processing of multiphase fluids is widely encountered in the industry. Examples are contactors in the chemical and petrochemical, food, power production and water industries. A main aspect that significantly governs the performance, efficiency and the sustainability of such systems is the way different phases are contacted. As a result, developing new processes and apparatuses for a more efficient way of contacting phases is always demanding. For gas-liquid systems in the chemical process industries, different types of contactors (reactors) have been developed. They are mainly categorized into column contactors such as fixed or fluidized beds; stirred-tank reactors in which the phases are mixed by agitation; membrane contactors; film reactors, and others.

In the last two decades, gas-liquid two-phase chemical reactors with micro- and millimeter-size channel structures have attracted great research interest from the industry and academia. They are considered as a promising alternative to conventional multiphase reactors, such as bubble columns and fixed bed reactors, which are widely used for gas absorption, catalytic hydrogenation, biochemical conversions, direct fluorination and others. The main advantage of small channel multiphase reactors is creation of a large volumetric interfacial area. In comparison with common column contactors like trickle bed reactors, they also provide lower pressure drop for a given specific contact area. The dominant flow pattern in such channels is segmented slug flow (Taylor flow) or bubble-train flow of elongated bubbles and slugs [1]. Taylor flow is a gas-liquid two-phase flow in small channels where liquid slugs are separated by bullet-shaped elongated gas bubbles (Fig. 1.1). The bubble shape is a

cylinder with spherical cap and tail with the cap somewhat stretched and the tail somewhat compressed [2].
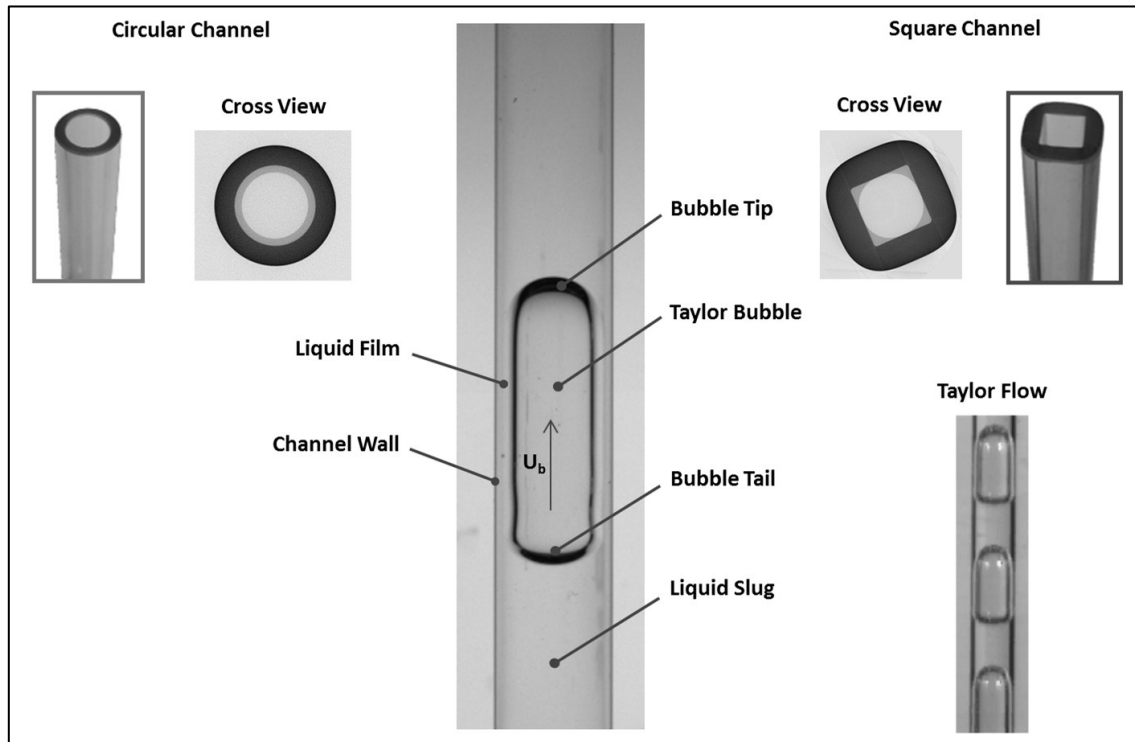

Fig. 1.1 Taylor bubble flow in a small channel.

The key advantages of Taylor flow are good mixing of species within the bubble, large interfacial area per unit volume, the thin liquid film between bubble and wall, reduced axial dispersion of liquid, good mixing and recirculation in liquid slug and wall-normal convective transport in laminar flow. These features make Taylor flow an ideal flow regime to improve heat and mass transfer performance [3], [4]. This flow regime is applied in various applications, including production of hydrocarbons in petroleum wells, steam boilers, transportation of cryogenic fluids, heat exchangers, and air-lift apparatuses [5].

A deep understanding of momentum, heat and mass transfer in small channel two-phase flow is crucial from the viewpoint of basic science as well as for practical design and operation of new chemical reaction devices, such as microfluidic and monolithic microreactors [2]. To develop models for transport phenomena and interface-resolving computational fluid dynamic techniques [6], it is vital to

have detailed data of three-dimensional bubble shape, liquid film thickness and velocity distribution in the liquid slug and around the bubbles.

In many industrial processes involving disperse gas and liquid, the mass transfer rate between the contacting phases is an essential parameter for the efficient design and control of the processes. Mass transfer between gas and liquid phases depends upon various parameters such as bubble size, fluid properties, relative velocity between the two phases, degree of liquid contamination, bubble shape, presence of a channel wall and many more.

So far several experimental and theoretical studies are known in which the effect of various parameters on mass transfer between Taylor bubbles and liquid slugs were investigated. However, there is only coarse knowledge on Taylor bubble shape in micro- and milli-channels available. Recent experimental investigations explored slug length and slug velocity using high-speed imaging, liquid velocity fields using PIV/LIF and film thickness using confocal laser scanning microscopy and laser focus displacement scanning. But the widely used optical measurement techniques have limitations in two-phase flow conditions and particularly they often have problems to resolve the full 3D shape of bubbles. Photographic measurement of bubble shape, requires careful refractive index matching to correct for image distortions due to optical refraction at the glass and liquid interfaces. Optical techniques are further constrained to transparent channels and fluids and diffraction limits the achievable spatial resolution to about one micrometer. These drawbacks may be overcome by the application of microfocus X-ray radiography and tomography.

Microfocus X-ray imaging is based on the application of X-ray sources with a focal spot size in the micrometer range. The measuring section is located inside the divergent X-ray beam which is coming from the source. High magnification ratios can be used to obtain the X-ray images with available two-dimensional flat panel image detectors with relatively coarse pixel spacing of few hundreds micrometers edge length. Since X-rays penetrates object on straight paths, refractive index matching is not required, and therefore, the internal structure of non-transparent media can be disclosed. The acquired X-ray images are correlated to the length of the X-ray paths in the medium, however, radiography is only a two-dimensional visualization technique. However, the acquisition of a set of projected images around the object can be used for reconstruction of the three-dimensional shape of

object at high resolution. This can be done via application of tomographic reconstruction algorithms [6],[7].

In capillary two-phase flow the surface tension and viscosity forces govern the hydrodynamics of the system. For larger channels ($D > 10$ mm) the surface tension forces are negligible in comparison with other body forces like inertial or buoyancy forces. It has been shown that for example for air bubbles in water in channels with $D > 5$ mm, the surface tension and buoyancy forces are comparable, though the buoyancy forces are dominant and bubbles can rise freely. In this thesis the focus is on millimeter-size channels with a hydraulic diameter between 5.5 mm – 8.5 mm. This range of diameters is widely unexplored with respect to fluid dynamics, while it addresses structured reactors, which can be made of tubes rather than of micro-structured components. This is an attractive concept for reaction engineers, as such structures can be produced with rather conventional manufacturing technologies.

1.2. Objective

The main goal of this work was to deepen the basic knowledge of Taylor bubble flow in small channels. For micro-channels with hydraulic diameters below 1 mm, intensive investigations have already been carried out by numerous researchers in the past decades. However, in this thesis the focus is on mini-channels and small pipes with a hydraulic diameter below 10 mm where both the surface tension forces and body forces are governing the bubble's motion and transport phenomena. Such channel sizes have been less explored in the past. In more detail, the mass transfer and the hydrodynamics of Taylor bubbles were investigated and the influence of different parameters and operating conditions such as channel size, bubble length, presence of contamination, and channel oscillation on the dissolution behavior and motion of bubbles was examined. To achieve these goals, a combination of microfocus X-ray technique and optical videometery was applied to disclose the three dimensional shape, volume, interfacial area, surface waves and free rise velocity of bubbles in millimeter-size channels.

The experimental setup was designed and constructed to be able to use both measurement techniques at the same time for different channel size and channel cross sections. The detailed goals of this study were as following:

1. To investigate the effect of channel size and channel cross section on the mass transfer of Taylor bubbles in millimeter-size channels. It includes the design and preparation of experimental setup for generation, injection, control and observation of Taylor bubbles of different sizes in different channel sizes and cross sections for investigation of mass transfer, bubble shape and free rise velocity of bubbles. Furthermore, to compare the measured experimental data with available experimental data and proposed models in the literature.

2. Liquid film thickness measurement for circular and square channel cross section.

3. To examine the effect of presence of contamination on the mass transfer of bubbles which includes the investigation of the effect of presence of surface active agents in the liquid phase on the bubble shape, liquid film thickness and mass transfer rate of Taylor bubbles.

4. To study the intensification of bubble dissolution by studying the effect of channel vibration. It involves the design and preparation of experimental setup to trace the shape and size of Taylor bubbles in presence of horizontal oscillation of the test section.

1.3.   Outline of the thesis

The thesis consists of eight chapters. In *chapter 2* a comprehensive review of recent experimental and theoretical investigations on Taylor bubble flow in small channels and microchannels is given. The chapter starts with an introduction of most important relevant works and reports the state of the art regarding the mass transfer studies of Taylor flow in both circular and square cross sectional channels. Moreover, a review of Taylor flow studies dealing with surfactants is given. Also a focused literature review regarding the intensification of mass transfer in small channels using oscillation is presented. Finally the chapter ends with the report of the most relevant works done on the liquid film thickness measurement for Taylor flow. In *chapter 3* a complete description of the experimental setup, is presented. Also detailed information about the start and procedure for doing the experiments are given. At the end the X-ray image acquisition process is presented. *Chapter 4* begins with the investigation of channel size and channel cross section on the bubble motion and mass transfer rate. It follows with the results of bubble rise velocity, shape and also the gas dissolution model. Finally the results of mass

transfer measurements are discussed. In *chapter 5*, the results of liquid film thickness measurements around the Taylor bubbles in circular and square channels are presented and compared with the available data in the literature. *Chapter 6* deals with the contamination of liquid phase and its influence on the motion and dissolution rate of Taylor bubbles in small channels. In *chapter 7*, the intensification of mass transfer of Taylor bubbles in small channels is investigated by applying vibration to the channel. The modifications in experimental setup and measurements devices are described and the impact of channel oscillation on the bubble shape and free rise velocity was studied. In *chapter 8* the results obtained in this study are summarized and open questions and challenges of future studies are discussed.

2. Theoretical background

2.1. Introduction

New developments in microreactors, compact heat exchangers, micro-condensers and fuel cells require precise knowledge of fluid dynamics in channels with small hydraulic diameters. Parameters of practical interest are pressure drop and heat and mass transfer per unit channel length. Especially in microreactor applications, slug or Taylor bubble flow is a desired operation state, due to the frequent change of efficient gas-liquid contacting in the film around the bubbles and the enhanced turbulent mixing in the liquid slugs behind the bubbles. Consequently, capillary slug flow is currently a target of intensive theoretical and experimental investigation.

A comprehensive overview of the state of art of different aspects of Taylor flow investigations is presented in this chapter and the most relevant experimental and theoretical studies on Taylor bubbles in small channels are summarized. First the relevant literature regarding the mass transfer studies of Taylor flow in circular and square cross sectional channels are presented and then a review of Taylor flow investigations in the presence of surface active agents is given. Furthermore, recent studies on the application of ultrasound and vibration in gas-liquid contacting systems for enhancement of mass transfer are shortly reviewed. And finally related theoretical and experimental works done on the liquid film thickness measurement for Taylor flow are briefly presented.

Fig. 2.1 illustrates the main parameters and dimensional quantities playing a role in the Taylor bubble flow in a small channel. Here U_b is the bubble velocity, D the channel diameter, L the bubble length,

U_L the liquid velocity and δ the liquid film thickness. By combining these quantities and the physico-chemical parameters of gas and liquid phases, dimensionless numbers can be derived. Dimensionless numbers are very beneficial to relate the variables of the system for different fluids in different operating conditions [8].
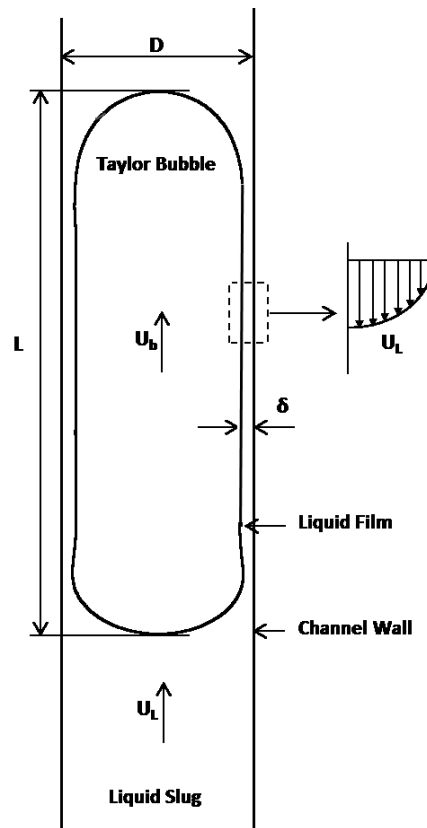

Fig. 2.1 Parameters and dimensional quantities playing a role in the Taylor bubble flow in a small channel

For our gas-liquid two-phase system where the surface tension, inertial, viscous and buoyancy forces are important, the following dimensionless numbers are relevant:

Reynolds number,

$$Re = \frac{U_b d_{eq} \rho_L}{\mu},$$ Eq. 2.1

which is defined as the ratio of inertial forces to the viscous forces and is used to determine the fluid flow pattern. Here d_{eq} is the diameter of a sphere with equivalent volume, ρ_L the liquid density and μ the liquid dynamic viscosity.

Capillary number,

8

$$Ca = \frac{\mu U_b}{\sigma},$$ Eq. 2.2

represents the relative effect of viscous forces to the surface tension forces in the interface of two phases. Here σ is the surface tension of liquid.

Sherwood number,

$$Sh = \frac{k_L d_{eq}}{D_c},$$ Eq. 2.3

is the ratio of mass transfer due to the convection to the mass transfer due to the diffusion. Here k_L is the liquid-side mass transfer coefficient between gas bubble and liquid slug and D_c the gas molecular diffusion coefficient.

Schmidt number,

$$Sc = \frac{\mu}{\rho_L D_c},$$ Eq. 2.4

is defined as the ratio of the momentum diffusivity to the mass diffusivity. This dimensionless number is used to determine the ratio of thickness of the momentum boundary layers to the concentration boundary layers.

Peclet number,

$$Pe = Re\ Sc = \frac{U_b d_{eq}}{D_c}.$$ Eq. 2.5

is the product of Reynolds and Schmidt numbers and represents the importance of transport of mass due to the convection to the transport of mass due to the diffusion.

2.2. Mass transfer in milli- and microchannels

2.2.1. Circular channel

One of the earliest investigations in mass transfer for single bubbles in small circular channels has been performed by Adeney and Becker [9],[1]. They measured the absorption rate of a single air bubble in water in a closed narrow vertical tube and concluded a single correlation from their findings. Filla [10] measured the liquid phase mass transfer resistance using a photographic method by means of holding a CO_2 bubble fixed in a down-flow of liquid [11]. He used aluminum powder and showed that the base (tail) of the bubble is covered by a stagnant layer of aluminum powder for both small and

large slugs and this stagnant portion of bubble interface reduced as the bubble becomes larger. Results were summarized by the following empirical equation:

$$Sh^* = 5.1 Pe_D^{0.5} \left(\frac{L}{D}\right)^{0.8},$$

Eq. 2.6

where Sh^* and Pe_D are modified Sherwood and Peclet numbers respectively, defined as

$$Sh^* = \frac{k_L A_{eq}}{D_c D},$$

Eq. 2.7

$$Pe_D = \frac{U_b D}{D_c},$$

Eq. 2.8

where A_{eq} is the surface area of sphere with equivalent bubble volume.

Baird and Davidson [12] measured the absorption rate of carbon dioxide from single rising bubbles of equivalent diameter 0.8-4.2 cm in water and Lissapol. They compared the results with a theoretical equation for absorption at the upper surface of a spherical cap bubble. They showed that absorption rates in tap water are about 50 percent higher than the ones predicted by their theory due to the absorption by the rippling rear surface of the bubble. Koide et al. [13] used the constant volume technique developed by Calderbank and Lochiel [14] for measuring the instantaneous mass transfer rates for single carbon dioxide bubbles and observed the influence of the bubble age on k_L even in clean pure liquids. They reported that the aging effect is more severe when the bubbles are small. Van Heuven and Beek [15] proposed for the first time a systematic analysis based on the assumption of a concentration boundary layer along the nose of a bubble and evaluated their theory by measuring the mass transfer of carbon dioxide from a large bubble of a mixture of CO_2-N_2 into water in gas lifts of different diameters. They proposed the following empirical correlation:

$$k_L = \pi D L D_c^{0.5} \left(\frac{g}{L}\right)^{0.25} I \left(\frac{L}{D}\right),$$

Eq. 2.9

where g is acceleration by gravity and $I(L/D)$ is an integral function to be evaluated numerically, whose values depends on the shape of the bubble [10],[16]. Redfield and Houghton [17] investigated the mass transfer rate of CO_2 single bubbles of 5–16 mm in diameter, rising in pure water and aqueous solutions of dextrose. They measured the volumetric change of gas bubbles in a system open to the atmosphere via displacement of water indicated by a mercury marker piston. They compared their results with the theoretical models and concluded that the experimental error is small enough that differences between the rigid sphere and the circulating sphere models are readily discernible [18]. Niranjan et al. [16] measured the change of pressure within the bubble due to gas dissolution. They

10

used the tube inversion technique originally demonstrated by Davidson and Kirk [11] to generate the bubbles. They carried out their investigations using water and aqueous solutions of glycerol, giving a range of viscosity from 10^{-3} to 1.6 Pa.s, and also aqueous carboxymethyl cellulose solutions. They correlated their experimental data in the following form:

$$Sh^* = 2.6 Pe_D^{0.5} \left(\frac{L}{D}\right)^{0.96}. \hspace{3cm} \text{Eq. 2.10}$$

Schulze and Schluender [18] measured the absorption rate of both weakly and highly soluble gases using a photographic method and showed that gases with high solubility give an absorption rate which is three times higher at the beginning and the rest can be described with the same liquid-side mass transfer coefficients k_L as found for the gases with low solubility. They observed that the measured k_L agrees well with the calculated one when assuming bubbles as rigid spheres. Influence of NaCl for high pressure absorption of a single CO_2 bubble was investigated by Tsuchiya et al. [19] both experimentally and theoretically. They showed that addition of NaCl reduces the absorption rate of CO_2 significantly and concluded that this effect arises from the suppression of wavy fluctuations along the gas-liquid interface. For small diameter bubbles of CO_2, Takemura and Yabe [20] used a charged-coupled device (CCD) camera coupled with a microscope to measure drag coefficient and Sherwood number. They carried out their experiments for Reynolds numbers below 100 in the transient regime, where the bubble changes from behaving as a fluid sphere to behaving as a solid particle and showed that the stagnant cap model can explain the mechanism of the transient process. Tsuchiya et al. [21] used high-speed imaging to investigate the effect of surface oscillations on the dissolution of a single CO_2 bubble into a liquid. The dissolution rate, which is claimed to be largely influenced by the liquid-phase contamination level, was found to be more inherently dependent on the extent of wave motion. Takemura et al. [22] investigated the dissolution rate of single carbon dioxide bubbles in sodium hydroxide (NaOH) solution. They numerically estimated the drag coefficient and Sherwood number *Sh* corresponding to the stagnant cap model by directly solving the Navier-Stokes and the convection diffusion-equations for a CO_2 bubble. They compared their results with the experimentally measured rising speed and dissolution rate and showed that the experimental and numerical results are in good agreement. Vasconcelos et al. [23] considered the effect of surface contamination on the dissolution of gases of low solubility in clean and untreated water. In clean water they detected two regimes.

Initially, the process is fast, consistent with the theory for circulating bubbles. Then, the mass transfer rate falls sharply to that predicted for solid spheres. Contrary to clean water, only the second regime was found in untreated water and they explained the results in terms of the kinetics of trace surfactant accumulation at the interface. Abe et al. [24] considered the effect of the liquid Reynolds number Re_L and surfactants on mass transfer of individual CO_2 bubbles in a vertical pipe of 25 mm diameter. They observed that the Sherwood number does not depend on Re_L because the magnitude of turbulent fluctuation velocity is much smaller than the relative velocity. Their results were summarized by following empirical correlation:

$$Sh = 0.081 Re^{0.872} Sc^{0.5} .$$
Eq. 2.11

Recently Donaldson et al. [25] carried out a systematic numerical analysis to investigate the impact of the underlying assumptions and the numerical complexity on the predicted mass transfer between a Taylor bubble and liquid slug in circular capillaries. They evaluated separate influences of bubble velocity and film length, slug length, and bubble film thickness on $k_L a$. They observed that the slug film model, which accounts for diffusion-limited mass transfer between the slug film and circulating bulk, has a reasonable agreement with empirical and CFD-based predictions. Kundu et al. [26] investigated the chemisorption of CO_2 Taylor bubbles into diethanolamine (DEA) solutions. They considered the influence of DEA concentration, gas composition and pipe diameter on the absorption of CO_2. They showed that CO_2 removal increases while absorption rate reduces with decreasing pipe diameter. Jimenez et al. [27] measured the mass transfer of rising small air bubbles ranging from 0.90 to 2.24 mm equivalent diameters by planar laser induced fluorescence (PLIF). They could show that the bubble shape is a crucial parameter which affects the mass transfer. Concerning the influence of the liquid composition, they observed that few changes in surface tension and/or viscosity are able to drastically alter the mass transfer behavior of the transferring bubble up to 88%. Hosoda et al. [28] measured the dissolution of single carbon dioxide bubbles with various bubble shapes such as spheroidal, wobbling, cap, and Taylor bubbles in vertical pipes using a stereoscopic image processing method and developed a correlation applicable to a wide range of bubbles. Their observations revealed that Sherwood numbers, Sh, strongly depend on bubble shape. Results can be summarized by the following empirical correlation:

$$Sh = \left(0.489(d_{eq}/D)^2 - 0.691(d_{eq}/D) + 2.064\right)Pe^{0.5} \quad for \quad 0.61 \leq (d_{eq}/D) \leq 2.0 , \qquad \text{Eq. 2.12}$$

$$Sh = \frac{2}{\sqrt{\pi}}\left(1.021(d_{eq}/D)^2 + 0.396(d_{eq}/D) + 1.0\right)Pe^{0.5} \quad for \quad 0 < (d_{eq}/D) < 0.61. \qquad \text{Eq. 2.13}$$

Table 2-1 summarizes the main parameters of the known previous studies on the mass transfer of single bubbles in channels. In comparison with the number of studies on the mass transfer from bubbles in infinite liquid, the number of investigations on the effect of wall on mass transfer rate is limited [29]. Almost all of the studies are for the channels larger than 12 mm inner diameter and so far little attention have been paid to smaller diameters. For small diameters (5.5 – 8 mm), the importance and role of interfacial forces on the hydrodynamics and mass transfer of bubbles are not negligible and should be considered.

Table 2-1 Previous studies on mass transfer of single bubbles in channels

Reference	Experimental method	Gas / Liquid properties	Bubble / Channel dimensions
Van Heuven and Beek, [15]	Photographic measurement of volume change	CO_2, N_2 / water	$1.6 < d_{eq}/D < 3.9$ D = 0.238, 0.48 mm
Filla, [10]	Photographic measurement of volume change	CO_2 / tap water	~$0.8 < d_{eq}/D < 2.4$ D = 24, 28, 35 mm
Schulze and Schluender, [18]	Photographic measurement of volume change	CO_2, N_2O, C_2H_2, O_2, N_2, H_2, Ne, He / 2-propanol, degassed water	$0.15 < d_{eq}/D < 0.3$ D = 10 mm
Niranjan et al. [16]	Measurement of pressure change of bubble	CO_2 / water, glycerol, CMC	$2 < d_{eq}/D < 8$ D = 13, 19.4, 25.7, 38.5, 51.5 mm
Koide et al. [13]	Constant volume technique	CO_2 / n-propanol, i-butanol, acetic acid, n-octanol, water	$4.6 < d_{eq} < 8.5$ mm D = 70 mm
Takemura and Yabe, [20]	Photographic measurement of volume change	O_2, CO_2 / water, silicone	$0.1 < d_{eq} < 0.5$ mm D = 40 mm square
Vasconcelos et al. [23]	Photographic measurement of volume change	Air / clean and untreated water	$1 < d_{eq}/D < 9$ D = 10, 40 mm square
Vandu et al. [30]	Photographic measurement of volume change	Air / demineralized water	~ $1.6 < d_{eq}/D < 3.9$ D = 1, 2, 3 mm, circular and square
Abe et al. [24]	Photographic measurement of volume change	CO_2 / Triton X-100, water	$0.2 < d_{eq}/D < 1$ D = 25 mm
Kundu et al. [26]	Photographic measurement of volume change	CO_2 / DEA, NaOH, water	D = 6 -10 mm
Jimenez et al. [27]	Planar laser induced fluorescence	Air / glucose, glycerol, NaCl, water	$0.9 < d_{eq}/D < 2.24$ D = 100 mm
Hosoda et al. [28]	Photographic measurement of volume change	CO_2 / water	$0.2 < d_{eq}/D < 1.8$ D = 12.5, 18.2, 25 mm

2.2.2. Square channel

For milli- and microreactors the bubble shape and relative velocity between the two phases are mainly governed by the cross-sectional shape of the channel. For channels with circular cross section (pipes) great attention has been paid in the last decades. However, other channel cross sections than circular ones were a subject of only a few studies [31].

Regarding the hydrodynamic investigations, Kolb and Cerro [32] presented experimental data for the flow of an open ended air bubble in a square capillary. They looked at the fluid-fluid interface in both the axial and radial directions for a wide range of capillary numbers, Ca, and showed that the transition from a non-axisymmetric to axisymmetric bubble occurs at $Ca \sim 0.1$. Thulasidas et al. [33] performed extensive experimental investigations in circular and square capillaries to measure bubble size and shape, bubble velocity, and volume fraction of gas inside capillaries for a large range of capillary numbers and also developed a mass balance model to compute the flow parameters with an iteration scheme. In another work [34] they used high-speed video imaging and particle image velocimetry (PIV) to characterize liquid flow patterns and velocity distributions inside liquid slugs. They observed that depending on the capillary number of the flow, counter rotating vortices or a complete bypass flow inside the liquid slug exist. Fries et al. [35] used Laser Induced Fluorescence (LIF) and confocal Laser Scanning Microscopy (LSM) to characterize gas–liquid phase distribution in rectangular microchannels. They did their experiments for low Ca in the range $2 \times 10^{-4} \leq Ca \leq 1 \times 10^{-2}$. They showed that the film thickness in the corners slightly decreases with Ca and that for low Ca values the film thickness at the wall is nearly constant. Taha and Cui [31] used the volume of fluid (VOF) method to study the hydrodynamics of slug flow inside square and circular capillaries containing Newtonian liquids by numerical computations. Their computed values of the velocity field and bubble diameter were in good agreement with published experimental data. Recently, Kuzmin et al. [36] reported on a simulation study of three-dimensional channels with square cross sections in the range $0.05 \leq Ca \leq 6.0$. By resolving the liquid film thickness as twice the interface thickness, they showed that the predicted axial and the diagonal bubble radius are consistent with those reported by Hazel and Heil [37]. They also investigated the existence of a vortex in front of the bubble and the

transition from the non-axisymmetric to symmetric case, and showed that the lattice Boltzmann binary liquid model are capable to be used for simulation of gas bubbles in microchannels.

Regarding mass transfer studies, the dissolution of oxygen into water in 1, 2 and 3 mm square and circular capillaries was investigated by Vandu et al. [30]. They used oxygen absorption dynamics to measure the volumetric mass transfer coefficient of O_2 as a function of channel diameter and showed that the experimental k_La values are in good agreement with the model developed by van Baten and Krishna [38] for circular capillaries when the dominant mass transfer contribution is assumed to be from the film surrounding the bubble. Dietrich et al. [39] focused on the characterization of gas–liquid mass transfer in a straight millimetric square channel. They developed a new colorimetric technique using an oxygen sensitive dye. They studied various hydrodynamic conditions, compared the equivalent oxygen concentration fields and measured the mass transfer coefficients. Their results were satisfactorily comparable with the measurements using oxygen microsensors. Recently Yue et al. [40] measured flow and mass transfer properties of air–water Taylor flow in square microchannels. Their data showed a large deviation from the available correlations in the literature, which mainly were developed for millimeter-size channels. They attributed this discrepancy to short liquid slugs produced in their microchannel and rather poor mixing between the liquid film and the liquid slug, which was not in accordance with assumptions associated with the available mass transfer correlations. As a result they applied modifications to the available correlations to be applicable for microchannels with reasonable predicting accuracy.

Concerning the role and importance of square channels in various existing and potential industrial applications such as micro-electromechanical systems and monolith froth reactors, there exist still some gaps particularly in related aspects of transport phenomena in these channels and further experimental work is needed to provide detailed heat and mass transfer data for model validation.

2.3. Presence of surfactant

For gas-liquid two-phase systems, one of the main factors, which is known to have a significant influence both on the hydrodynamics and mass transfer rate of phases, is presence of surface active

agents (surfactants). Surfactants are adsorbed at gas–liquid interfaces and decrease the surface tension. The presence of surfactants in multiphase systems, either in the form of unavoidable impurities or as additives, has a great effect on the shape and the dynamics of the interfaces [41]. In the following, the most relevant studies on the effect of surfactants on the gas-liquid systems are shortly reviewed.

2.3.1. Theoretical investigations

Regarding theoretical studies, Weber [42] investigated the effect of surfactant on the mass transfer of spherical-cap bubbles at Reynolds number higher than 100. It was supposed that the surfactant forms a stagnant film on the spherical surface near the rim of the bubble and its effect was attributed to a balance between surface forces and shear forces. Comparison of their results with experimental data showed agreement within 25%. Stokes flow due to the motion of a liquid drop or bubble in a contaminated immiscible fluid was analyzed by Sadhal and Johnson [43]. An exact solution was found for the resulting problem for an arbitrary cap angle and an expression for the drag force in terms of viscosities and the cap angle was for the first time developed. The dissolution of spherical bubbles at low Reynolds numbers was studied by Dani [44] using Direct Numerical Simulation (DNS) for fully contaminated, partially contaminated and clean bubbles by applying the conventional stagnant cap model. The comparison of results with classical relations showed the good scaling of Sherwood number with $Pe^{1/3}$ and $Re^{1/2}$ respectively for solid sphere and clean bubble in creeping flow.

In a comprehensive study, Muradoglu and Tryggvason [45] developed a finite-difference/front-tracking method to simulate the interfacial flows with soluble surfactants. In their method both the interface and bulk surfactant concentration evolution equations were solved and coupled with the incompressible flow equations. The simulation was done to predict the influence of surfactant on the hydrodynamics of buoyant viscous bubbles in a straight channel. It was found that the contaminated bubble behaves like a solid sphere in the limit of very low Reynolds number $Re < 1$ and the results were found to be in a good agreement with the experimental correlations collected by Clift et al. [46]. Tasoglu et al. [47] used the same approach to study the unsteady motion and deformation of a bubble rising in an otherwise quiescent liquid. They showed that the surfactant generally decreases the terminal velocity of the bubble but this reduction is most noticeable in the nearly spherical regime in which the bubble behaves like a solid sphere and its terminal velocity reaches that of a solid sphere.

Cuenot et al. [48] considered the similar problem and confirmed the validity of the well-known stagnant-cap model for describing the flow around a bubble contaminated by surfactants. Their results indicated a considerable rise of the drag which in several cases reaches the value corresponding to a rigid sphere. Hayashi and Tomiyama [49] investigated the effect of surfactant on the terminal velocity of Taylor bubbles in vertical pipes. They applied an interface tracking method and simulated for various Eötvös numbers ($Eo = \Delta \rho g D^2 / \sigma$), different surfactant concentration and two different surfactants, where $\Delta \rho$ is the density difference between two phases. They showed that the terminal velocity of bubbles increased because of reduction of surface tension near the bubble nose and since the bubbles at high Eötvös numbers are independent of surface tension, the presence of surfactant does not affect the terminal velocities of high Eötvös number bubbles.

Ghadiali and Gaver [50] utilized a numerical model of semi-infinite air bubbles in a capillary to analyze the continual interfacial expansion dynamics that occur during the opening of collapsed pulmonary airways. They showed that the surfactant properties can strongly affect the interfacial pressure drop through modification of the surface tension and the creation of Marangoni effect. In addition, they showed that, depending upon the range of parameters, either film thickening or film thinning responses are possible.

In case of liquid film thickness around the bubble, Ginley and Radke [51] presented a regular perturbation expansion in large adsorption rates within the low capillary number, singular perturbation hydrodynamic theory of Bretherton. They considered surface transport of the surfactants and neglected all concentration gradients in the bulk phase and showed that by addition of soluble surfactant to the liquid phase, the surface concentration increases in the thin film region and leads to a decrease in the film thickness compared to the surfactant-free case. In contrary, in a more comprehensive analysis and for a semi-infinite bubble in a capillary, Ratulowski and Chang [52] carried out an asymptotic analysis for various convective, diffusive and kinetic timescales and showed that, if transport in the film is mass-transfer limited, the film thickness increases by a maximum factor of $4^{2/3}$ over Bretherton's result at low bubble velocities. Stebe and Barthes-Biesel [53] considered the same problem for a viscous surfactant solution at high concentration. They considered the case where the surfactant flux is adsorption-desorption controlled and the equations of momentum and mass transfer are coupled to

leading order. The results showed that interfaces with surface viscosities require larger pressure drops to aspirate the flow and leave thicker wetting layers along the capillary walls. For finite length bubbles in capillaries, Park [54] studied the influence of soluble surfactant on the steady motion of inviscid bubbles. Both front and rear ends of the bubble were examined in the limit of small capillary number and it was shown that due to the accumulation of the surfactant at the rear end of the bubble, the film thickening effect of the surfactant occurs only when the bubble length is greater than a certain critical value.

Daripa and Pasa [55] presented a theoretical proof for the thickening phenomenon in Bretherton problem applying perturbation theory and a lubrication analysis of the flow equations in a horizontal capillary. In another work [56], they investigated the influence of surfactant in a vertical capillary tube containing a viscous fluid and sealed at one end. They only considered interfacial surfactant on the interface of bubbles and ignored the presence of surfactant in the bulk. However, they showed that the presence of surfactant on the bubble interface gives a thinning effect on the thickness of the liquid layer behind the bubble. Recently, Olgac and Muradoglu [57] considered the impact of both insoluble and soluble surfactants on the motion of long bubbles in horizontal axisymmetric capillaries computationally using a finite-difference method. The results showed that both the insoluble and soluble surfactant have a thickening effect on the film thickness, which is especially prominent at low capillary numbers.

2.3.2. Experimental investigations

In case of experimental studies, Mancy and Okun [58] studied the various factors involved in the influence of surfactant on the rate of oxygen dissolution in aeration process. They used Aerosol O.T. as surfactant and showed that addition of small amounts of Aerosol O.T. causes to reduction of oxygen transfer to a minimum. Griffith [59] investigated the impact of surfactants on the terminal velocity of bubbles and drops. They showed that terminal velocity at small Reynolds numbers are related to the cap size and then to the type and amount of surfactant. Using high speed photography technique, Raymond and Zieminski [60] studied the influence of aliphatic alcohols on mass transfer and drag coefficients of a single carbon dioxide bubble. The results showed that the concentration, molecular size, and structure of the investigated alcohols have a great effect on mass transfer as well as drag

18

coefficients of the rising bubble. In a stirred tank, Vazquez et al. [61] measured the volumetric mass transfer coefficients, $k_L a$, for the absorption of bubbled and unbubbled CO_2 in presence of surfactants. The results of experiments showed a dependency of $k_L a$ on stirring rate, type of bubbling device and surfactant concentration in the liquid phase. In another work [62], they considered the impact of surfactant in the bubble columns, and showed that the presence of the surfactant induces reduction of the interfacial area as well as the mass transfer coefficient of bubbles.

For Reynolds numbers below 100, Takemura and Yabe [20] investigated the bubble rise velocity and dissolution rate of carbon dioxide bubbles in slightly contaminated water. They compared the experimental results with numerical results developed by stagnant cap model and proposed equations for estimating the drag coefficient and Sherwood number and clarified that the gas–liquid interface of the carbon dioxide bubbles in the range 0.2 mm $< d <$ 1 mm in water are immobile. For bubble columns and air lift, Vasconcelos et al. [63] indicated that the values of liquid-side mass transfer coefficient, k_L, always lie between the theoretical values for fully mobile and rigid interfaces. The results were analyzed based on the modelling of the kinetics of single bubble contamination and in accordance with the stagnant cap model. Calculated and experimental k_L values agreed within ±30%. Loubière and Hébrard [64] studied the effect of liquid surface tension on the bubble formation from both rigid and flexible orifice. The results showed that the effect of surface tension on the generated bubbles cannot be considered only in terms of the static surface tension and also depends on whether the bubbles are produced from a rigid orifice or from a flexible orifices. Alves et al. [65] systematically investigated individual stationary air bubbles of 1–5 mm in a downward liquid flow. They interpreted both the drag coefficient and mass transfer coefficient based on the bubble contamination using the stagnant cap model and showed that the mass transfer coefficient for clean front and stagnant cap are consistent with theoretical prediction of Higbie´s and Frössling´s equations, respectively. In another study [66] they investigated the effect of Polyethylene glycol (PEG) on the average mass transfer coefficient in an aerated stirred tank. The results indicated that bubbles in surfactant (PEG) solution behave as rigid bubbles, while bubbles in tap water behave closer to having a mobile interface and bubbles in salt solution have intermediate k_L values.

The buoyancy-driven motion of bubbles and drops in a vertical small tube was studied by Almatroushi and Borhan [67]. The results showed that the presence of a surfactant slows down the motion of small bubbles due to the development of adverse Marangoni stresses, while it increases the motion of large bubbles by allowing them to deform away from the tube wall more easily. Painmanakul et al. [68] investigated the effect of surfactant on bubble generation, interfacial area and the mass transfer rate in the dynamic bubble regime (Re = 150-1000). It was clearly shown that the presence of surfactants affects the bubble generation and thus the interfacial area, and the liquid-side mass transfer coefficient. It was proved that the surface coverage ratio is crucial for predicting the changes of k_L in aqueous solutions with surfactants. The effect of anionic, cationic and non-ionic surfactants on the mass transfer rate of bubbles in a small-scale bubble column was examined by Sardeing et al. [69]. They found three zones in the mass transfer coefficient as a function of bubble diameter and showed that Higbie´s model does not predict the k_L values for large bubbles. Rosso et al. [70] prepared an experimental apparatus to concurrently measure dynamic surface tension and mass transfer for single and multiple bubbles. They showed that for a constant contamination, interfaces with higher renewal rates have higher dissolution rate and concluded that higher interfacial flow regimes can compensate contamination.

The effect of surface tension on pressure drop in a 1mm square microchannel was investigated by English and Kandlikar [71], [72]. They applied water-surfactant mixtures of different concentrations and the accuracy of various two-phase pressure drop models was evaluated. They proposed a new model for laminar-laminar two-phase flow pressure drop. Takagi et al. [73] investigated the dependence of the motion of a 1mm bubble rising through the laminar shear flow on 1-, 3-Pentanol and Triton X-100 concentration using a high-speed camera. The results confirmed that a bubble with larger Marangoni effect has smaller lateral migration. Furthermore, it was indicated that lower contaminant level and higher shear rate lead to a remarkable bubble migration toward the wall, which causes the development of bubble clusters. The effect of high concentration of surfactants on liquid-side mass transfer coefficient in free gas–liquid interface was examined by Hebrard et al. [74]. A reduction in the mass transfer coefficient with an increase of surfactant concentrations was detected as well as a plateau when the concentration reaches critical micelle concentration (CMC); the smallest

value was observed for a pure solution of surfactant. Jamnongwong et al. [75] examined the effect of presence of various substances commonly encountered in biological media on oxygen diffusion coefficient and liquid-side mass transfer coefficient. The results indicated that for all cases, oxygen diffusion coefficients decreased when compared to clean water, and, the rate of change of oxygen diffusion coefficient, D_c, is directly related to the type of substance. In bubbly channel flow, Takagi and Matsumoto [76] reviewed the recent investigations associated with subsequent variation of bubble behavior due to the surfactant adsorption/desorption on the bubble surface and concluded that the presence of surfactants influences the small-scale behavior of each bubble, and then this variation in bubble behavior causes a large-scale variation of global bubbly flow structures, which further influences each bubble's behavior.

The influence of surfactant addition and sparger design on the mass transfer, the gas holdup and bubble size distribution in a bubble column was compared by McClure et al. [77]. The results showed that addition of both hydrophilic and hydrophobic surfactants cause an approximately threefold decrease in mass transfer coefficient and presence of surfactant has a greater effect on oxygen dissolution than do changes in the sparger design. Huang and Saito [78] applied the laser-induced fluorescence (LIF/HPTS) method to investigate the effect of bubble-surface contamination on the relationship between instantaneous mass transfer, bubble motion, and bubble-induced surrounding liquid motion. They showed that in the contaminated water, because of desorption of surfactants and the Marangoni convection on the bubble surface, the mass transfer oscillates in accordance with bubble velocity and the Marangoni convection altered both the liquid motions near the bubble surface and the bubble wake. Recently, Aoki et al. [29] investigated the effect of concentration of surfactant on the rate of mass transfer for single rising bubbles. They used Triton X-100 as surfactant and showed that for small bubbles the mass transfer rate reduces with increase of surfactant concentration and it however rises with the bubble size and approaches that of clean Taylor bubbles as for large bubble size. Furthermore, it was proven that the surfactant adsorbs only in the bubble tail region and the nose-to-side region is almost clean for large bubbles. In another work [79] they investigated the effect of type of surfactant on the mass transfer from single fully contaminated carbon dioxide bubbles. They showed that the k_L of contaminated Taylor bubbles have varying trends because of the

difference in the surfactant distributions at the bubble interfaces which strongly depend on the Hatta number.

Table 2-2 summarizes the main parameters of the known previous studies on the impact of presence of surfactant in gas-liquid two-phase interfaces. As mentioned above, most attention has been paid so far to the small spherical bubbles in infinite liquid regarding the effect of surfactant on the mass transfer rate. However, non-spherical large bubbles in small channels, which mainly exist in micro- and milli-channels in the form of Taylor bubbles, were the subject of only a few studies [79],[69]. On the other hand, regarding the influence of surfactant on the liquid film thickness for elongated bubbles in capillaries almost all of the investigations are theoretical and according to our knowledge very few experimental evidences could be found [55]. In addition, among the available theoretical investigations, in some references it was shown that surfactant has a thickening effect on the liquid film thickness whereas in others a thinning influence was found [51], [55], [80].

2.4.   Mass transfer intensification in small channels

The main advantages of small channel multiphase reactors are creation of a large volumetric interfacial area. However, because the governing flow regime in such reactors is laminar, the liquid-side mass transfer coefficient between the phases is lower than for turbulent flow in e.g. bubble columns or stirred tank reactors [81]. To enhance the individual mass transfer coefficient, one of the most recently considered methods is applying structural vibration or sound fields to agitate the fluidic phases. Such approaches were demonstrated for many conventional multiphase contactors and proven their ability to intensify the mass transport processes [81], [82]. In the following, the most relevant studies on the application of ultrasound and vibration in gas-liquid contacting systems will be shortly reviewed.

One of the first investigations on the effect of axial vibration on bubble-bed gas absorbers has been carried out by Harbaum and Houghton [83]. They demonstrated a noticeable enhancement in mass transfer performance in the frequency range 20 Hz to 200 Hz. Jaeger and Kurzweg [84] investigated the longitudinal dispersion in oscillatory pipe flow of binary gas mixtures at high axial oscillation

Table 2-2 Previous studies on the impact of presence of surfactant in gas-liquid two-phase flows

Reference	Contact device	Gas / Liquid / Surfactant	Bubble / Channel dimensions	Parameter studied
Mancy and Okun [58]	Bubble column	O_2 / water / aerosol O.T.	$1.7 < d_{eq} < 2.4$ mm $D = 220$ mm	Mass transfer coefficient, bubble volume
Griffith [59]	Bubble column	Carbon-tetrachloride / glycerine / aerosol O.T., O.S.	$D = 100$ mm	Bubble terminal velocity
Raymond and Zieminski [60]	Bubble column	CO_2 / water / aliphatic alcohols	$0.13 < d_{eq} < 0.2$ mm	Mass transfer coefficient, drag coefficient
Vizquez et al. [61]	Stirred tank	CO_2 / water / sodium lauryl solphate	$0.04 < d_{eq} < 0.2$ mm $D = 143$ mm	Mass transfer coefficient
Vizquez et al. [62]	Bubble column	CO_2 / water / sodium lauryl solphate, sodium carbonate, sodium arsenite	$4.6 < d_{eq} < 8.5$ mm $D = 113$ mm	Mass transfer coefficient, interfacial area
Takemura and Yabe [20]	Square vessel	CO_2 / water	$0.1 < d_{eq} < 0.5$ mm $D = 40$ mm square	Mass transfer coefficient, drag coefficient
Vasconcelos et al. [63]	Bubble column, rectangular airlift	O_2, air / water / antifoam Sigma 289	$3 < d_{eq} < 5$ mm $D = 92$, 17 mm	Mass transfer coefficient
Loubière and Hébrard [64]	Square vessel	Air / water / butanol sodium lauryl sulphate, fatty alcohol C12/18, lauryl dimethyl benzyl ammonium bromine	$0.5 < d_{eq} < 5$ mm $D = 400$ mm square	Bubble diameter, dynamic surface tension, bubble frequency
Alves et al. [65]	Stirred tank	Air / water / sodium sulphate, PEG	$0.8 < d_{eq} < 3$ mm $D = 29.2$ mm	Mass transfer coefficient, local gas hold-up, local bubble size
Alves et al. [66]	Vertical tube	Air / distilled water, millipore water	$0.5 < d_{eq} < 5$ mm $D = 22$, 31 mm	Mass transfer coefficient, drag coefficient, rise velocity
Almatroushi and Borhan [67]	Capillary tube	Air / water / UCON LB-165, glycerol, sodium dodecyl sulfate (SDS)	$4.0 < d_{eq} < 15$ mm $D = 7.96$ mm	Bubble terminal velocity
Painmanakul et al. [68]	Bubble column	Air / water / sodium lauryl sulphate, lauryl dimethyl benzyl ammonium bromine	$3 < d_{eq} < 9$ mm $D = 50$ mm	Mass transfer coefficient, rise velocity, interfacial area
Sardeing et al. [69]	Bubble column	Air / water / sodium lauryl sulfate, lauryl dimethyl benzyl ammonium bromine, fatty alcohol C12/18	$1 < d_{eq} < 8$ mm $D = 50$ mm	Mass transfer coefficient, rise velocity, interfacial area
Rosso et al. [70]	Square graduated column	Air / water / SDS, IAA	$d_{eq} < 5$ mm	Mass transfer coefficient, dynamic surface tension
English and Kandlikar [71],[72]	Square minichannels	Air / water / Triton DF-12	$D = 1$ mm square	Pressure drop
Takagi et al. [73], [76]	Bubble column	Air / water / 1-, 3-Pentanol, Triton X-100	$d_{eq} = 1$ mm $D = 7.27$ mm	Rise velocity, drag coefficient
Hebrard et al. [74]	Agitated vessel	Air / water / Texapon	$d_{eq} > 1$ mm $D = 65$ mm	Mass transfer coefficient, diffusion coefficient
Jamnongwong et al. [75]	Agitated vessel	Air / water / NaCl, glucose, sodium lauryl sulphate	$1 < d_{eq} < 5.3$ mm $D = 65$ mm	Mass transfer coefficient, diffusion coefficient
McClure et al. [77]	Bubble column	Air / water / sodium sulfite, 2-propanol, mannitol, antifoam	$2 < d_{eq} < 40$ mm $D = 190$ mm	Mass transfer coefficient, interfacial area
Huang and Saito [78]	Square channel	CO_2 / water / 1-pentanol	$d_{eq} = 2.9$ mm $D = 15$ mm square	Bubble shape and motion
Aoki et al. [29], [79]	Vertical tube	CO_2 / water / Triton X-100, 1-octanol	$5 < d_{eq} < 30$ mm $D = 12.5$, 18.2, 25.0 mm	Mass transfer coefficient, rise velocity, bubble shape

frequencies. It was shown that the magnitude of the dispersion coefficient is directly related to the product of the frequency and the square of oscillation amplitude. For elongated Taylor bubbles, Brannock and Kubie [85] were the first who investigated the influence of vibration on the free rise velocity of bubbles [86]. They measured the rise velocity of long bubbles while exposing the vertical pipes to an axial sinusoidal motion. It was found that an acceleration of up to 10 m/s^2 had no considerable influence on the bubble shapes while for acceleration up to 15 m/s^2 the bubbles started to distort. The bubble nose became more elongated and its curvature increased. The results indicate that the bubble rise velocity increases as the acceleration decreases. For a horizontal motion of vertical channels, Kubie [87] performed a similar study and investigated the rise velocity of elongated bubbles. It was shown that the mean bubble velocity is a function of the pipe diameter, the relative acceleration and the amplitude of the sinusoidal motion and increases as the relative acceleration increases. He also compared the increasing trend of the bubble rise velocity in horizontal direction with the decreasing rise velocity for vertical channel vibration and showed that the reason for this difference is the direction and magnitude of resulting acceleration acting on the bubbles.

Ellenberger and Krishna [88], [89] discussed the application of low-frequency vertical vibrations to the liquid phase of an air–water bubble column. They mounted a vibration exciter at the bottom of the bubble column which transfers the vibration to the liquid phase by means of a piston. They showed that vibration leads to considerably smaller bubbles at the nozzle. Also, it was shown that application of vibrations causes enhancement of mass transfer coefficient and gas hold up by a factor of two or more [90]. Furthermore, the results showed that application of vertical oscillation has the potential of enhancing the contacting of phases in fluid-fluid dispersions [91],[92]. Dillon et al. [93] investigated the pressure drop of two-phase flow in a narrow horizontal annular test section with an inner diameter of 7.93 mm. The influence of lateral mechanical oscillation of the test section on two-phase pressure drop was investigated, with vibration amplitudes up to 0.2 mm and frequencies in the range 5 Hz to 400 Hz. The results showed a negligible influence of the vibration, which was within the experimental uncertainty limits. The impact of low-frequency vertical vibrations on the hydrodynamics and mass transfer characteristics of monolith loop reactors was studied by Vandu et al. [94] and compared with conventional internal airlift reactor and bubble column configurations. The results showed that

imposing oscillation has the effect of significantly improving the ratio of volumetric mass transfer coefficient to the gas hold up for all considered reactor configurations. For monoliths, it was moreover found that vibrations additionally improve the gas–liquid distribution across the channels.

Hashmi et al. [95] reviewed current knowledge about the underlying physics of oscillating bubbles in micro-sized contactors. They critically discussed state of the art on the application of oscillation in microfluidic devices. They also highlighted the benefits and the challenges of using vibrating bubbles and argued that these investigations would be revolutionary to the progress of next-generation Lab-on-Chip systems. Madani et al. [86] considered the rise of a Taylor bubble in a vertical vibrating channel. The experiments were done for two different pipe diameters and with fluids of different viscosities and restricted to high Reynolds numbers to study the inertial effects. The results showed that for low acceleration the average velocity decreases with the relative acceleration of oscillation. Also, it was shown that, beyond a critical relative acceleration, the mean bubble velocity rises and the increase of fluctuating velocity slows down. Fernandez Rivas et al. [96] reviewed concepts of micro-sono-reactors and discussed the latest progress and future directions. They discussed that micro-sono-reactors are capable of handling small reaction volumes in a reproducible and efficient system, for which the main parameters of the system such as frequency, amplitude, acoustic power, and sonication times can be accurately adjusted. Moreover, it was argued that processes including the micro-sono-reactors are easily scalable and enable flow recirculation.

Polezhaev et al. [97] found a significant increasing evaporation rate in a tube in which the gas/liquid interface axially oscillates and reported a tenfold increase of the apparent diffusive coefficient. The dependency of the enhancing effect on the tube diameter, the frequency and the amplitude of the liquid oscillations was investigated and the parametric dependence of the apparent diffusive coefficient was correlated via the associated dimensionless Peclet number. Yao [82] gave an overview over the recent investigations on the application of power ultrasound to adsorbent regeneration, food drying, air dehumidification, water treatment and others. They concluded that although the ultrasonic treatment may cause degradation of especially biological process constituents, it can significantly help to decrease the food processing time and reduce the drying temperature. Recently, Dong et al. [98] used ultrasonic oscillation to intensify the gas-liquid mass transfer in microreactors. They applied severe

surface wave vibration on the bubbles and found that for slug bubbles confined in a smaller microchannel, surface wave oscillations require more ultrasound energy to excite due to the confinement effect. It was proven that the volumetric mass transfer coefficient increased by 3 to 20 times under oscillation. Furthermore, it was shown that for gas-liquid flow hydrodynamics, oscillation disrupts the bubble formation process and alters the initial bubble size and pressure drop [81].

As it was briefly summarized, oscillation/vibration of transferring phases is a promising and efficient approach to intensify transport processes. However, on one hand, most of the investigations are focused on the micro-sized reactors and little attention has been paid to the millimeter-size channels such as monolithic reactors. On the other hand, most reported studies were devoted to axial or vertical oscillation of channels, which has some drawbacks for process itself, such as stronger axial back mixing and decreasing the rise velocity of the gas phase.

2.5. Liquid film thickness in mini-channels

2.5.1. Circular channels

For circular channel several investigations have been done to measure the liquid film thickness around the bubbles in small channels. One of the first investigations was done by Fairbrother and Stubbs [99]. They experimentally measured the velocity of the liquid phase in a capillary and the bubble velocity and showed that the bubbles travel considerably faster than the average flow due to the deposition of a liquid layer (film) on the capillary walls. They proposed an experimental correlation for moving bubbles of sufficient length ($> 3r_c$) for $7.5 \times 10^{-5} < Ca < 0.014$

$$W \equiv \frac{U_b - U_L}{U_b} = Ca^{0.5},$$ Eq. 2.14

where W is partial amount of liquid remained on the internal surface of tube, U_L the mean velocity of liquid phase and r_c the channel radius. With the assumption that the liquid film around the bubble is at rest, they showed that

$$\frac{W}{2} = \frac{\delta}{r_c} = 0.5Ca^{0.5},$$ Eq. 2.15

where δ denotes the thickness of the liquid film around the bubble.

Taylor [100] continued their work by considering the amount of liquid left inside of the tube when air bubble passed and showed that Eq. 2.15 is valid for $Ca < 0.09$. Using the electrical conductimetery technique, Marchessault and Mason [101] measured the effective film thickness surrounding moving air bubbles in glass capillary tubes. The liquid film thickness around the air bubbles inside circular capillaries with different fluids was measured and the results showed a good agreement with Eq. 2.15. They also proposed a relation for Capillary numbers ranging from 7×10^{-6} to 2×10^{-4}:

$$\frac{\delta}{r_c} = -0.05 \left(\frac{\mu}{\sigma}\right)^{0.5} + 0.89 Ca^{0.5}.$$

Eq. 2.16

Employing the lubrication theory and assuming there is no tangential stress at the fluid-fluid interface, Bretherton [102] theoretically analyzed the displacement of long bubbles in a round capillary and showed that the wetting film thickness left behind the bubbles is proportional to $Ca^{2/3}$ for $Ca < 0.005$:

$$\frac{\delta}{r_c} = 1.337 Ca^{2/3}.$$

Eq. 2.17

In the range of $Ca < 10^{-4}$, however, his model underpredicts the liquid film thickness and shows a systematic deviation. He proposed a number of explanations for the inconsistency between theory and experiment which include surface roughness, instability of the meniscus, intermolecular forces, and adsorbed impurities [52]. By direct observation through a microscope, Goldsmith and Mason [103] measured the film thickness around the bubbles and the velocity profiles inside the bubble and in the film. They showed that for bubbles with negligible viscosity, the film surrounding the body of the bubbles was at rest as predicted by the theory of bubble flow based on parallel creeping motion in the film theory. It was found that the liquid film thickness was consistent with the data predicted by the empirical Fairbrother-Stubbs correlation.

Teletzke [104] reformulated the Bretherton model and considered the influence of a finite dispersed phase viscosity and intermolecular forces. However, his model could not describe the deviation between the theory and experiment for low Capillary numbers. For air, water, ethanol, and glycerol systems, Irandoust and Andersson [105] did experimental research on upward and downward Taylor flow in vertical pipes of $D = 1–2$ mm and a length of $L_c = 0.4$ m. The film thickness was fitted to the empirical formula

$$\delta = 0.18D_h[1 - exp(-3.1Ca^{0.54})].$$ Eq. 2.18

Moreover, the numerical solution of the Navier-Stokes and surface tension equations, showed excellent agreement with air-ethanol experimental data. Aussillous and Quere [106] investigated the averaged film thickness from the length variation of the liquid slug for varying tube radius and proposed the following inertia-dependent correlation:

$$\delta \sim D \frac{Ca^{2/3}}{1+Ca^{2/3}-We},$$ Eq. 2.19

where We is Weber number defined as

$$We = \frac{\rho U_b^2 D}{\sigma}.$$ Eq. 2.20

It was observed that due to the inertial effects, the liquid film is thicker than the Taylor's experimental data at high capillary numbers. Kreutzer et al. [107] experimentally and numerically investigated the liquid film thickness and also the pressure drop in a 2.3 mm pipe. For low Reynolds numbers their results show a good agreement with the classical lubrication analysis. Their results show the same trend for the numerical and experimental data, however, the simulation prediction deviates systematically from the experimental data. The deviation was attributed to the Marangoni effects, since this effect was not taken into account in the simulations. The predicted liquid film thickness showed almost the same trend with simulation results reported by Heil [108].

The local and instantaneous liquid film thickness in micro-scale tubes were measured by Han and Shikazono [109] using laser confocal displacement meter. They showed that at small capillary numbers, the liquid film thickness is determined only by capillary number and the effect of inertia force is negligible. However, for high Ca, the effect of inertia force cannot be neglected and liquid film thickness takes a minimum value against Reynolds number. They developed the following experimental correlation for the initial liquid film as a function of capillary number, Reynolds number and Weber number:

$$\frac{\delta}{D} = \begin{cases} \dfrac{0.670Ca^{\frac{2}{3}}}{1+3.13Ca^{\frac{2}{3}}+0.504Ca^{0.672}Re^{0.589}-0.352We^{0.629}} & (for\ Re < 2000) \\[4ex] \dfrac{106.0\left(\frac{\mu^2}{\rho\sigma D}\right)^{\frac{2}{3}}}{1+497.0\left(\frac{\mu^2}{\rho\sigma D}\right)^{\frac{2}{3}}+7330\left(\frac{\mu^2}{\rho\sigma D}\right)^{0.672}-5000\left(\frac{\mu^2}{\rho\sigma D}\right)^{0.629}} & (for\ Re > 2000) \end{cases}$$ Eq. 2.21

Youn et al. [110] using the same technique investigated the effect of initial flow velocity on the liquid film thickness in micro tubes in accelerated flows under adiabatic condition. The results showed that the initial flow velocity plays a considerable role in accelerated flows especially at large initial flow velocities and at large Bond numbers. Their results were correlated in the following equation to account for the initial liquid velocities:

for $Ca < Ca^{**}$

$$\frac{\delta}{D} = \begin{cases} min\left[\left(\frac{\delta}{D}\right)_{steady}, \left(\frac{\delta}{D}\right)_{accel}\right] & for \quad \left(\frac{\delta}{D}\right)_{steady\ at\ Ca_0} < \left(\frac{\delta}{D}\right)_{accel\ at\ Ca_0} \\ max\left[\left(\frac{\delta}{D}\right)_{steady\ at\ Ca_0}, \left(\frac{\delta}{D}\right)_{accel}\right] & for \quad \left(\frac{\delta}{D}\right)_{steady\ at\ Ca_0} > \left(\frac{\delta}{D}\right)_{accel\ at\ Ca_0} \end{cases} \qquad \text{Eq. 2.22}$$

for $Ca > Ca^{**}$

$$\frac{\delta}{D} = \left(\frac{\delta}{D}\right)_{accel\ at\ Ca^{**}}, \qquad \text{Eq. 2.23}$$

where

$$Ca^{**} = 19.8\left(\frac{\mu^2}{\rho\sigma D}\right), \qquad \text{Eq. 2.24}$$

$$\left(\frac{\delta}{D}\right)_{steady} = \frac{0.67Ca^{2/3}}{1+3.13Ca^{2/3}+0.504Ca^{0.672}Re^{0.589}-0.352We^{0.629}}, \qquad \text{Eq. 2.25}$$

$$\left(\frac{\delta}{D}\right)_{accel} = \frac{0.968Ca^{2/3}}{Bo^{0.414}+4.838Ca^{2/3}}, \qquad \text{Eq. 2.26}$$

$$Bo = \frac{\rho a_f D^2}{\sigma}, \qquad \text{Eq. 2.27}$$

and *Bo* is Bond number based on the flow acceleration a_f.

2.5.2. Square channels

In case of channels with non-circular cross section, Singhal and Somerton [111] were one of the first to measure the liquid film thickness. They theoretically investigated the flow mechanism, velocity distribution, transition conditions and amount of liquid wetting the walls within triangular shape channels and an empirical relation, similar to those obtained for circular tubes, was suggested.

Kolb and Cerro [32] used a capillary with square cross section to visualize the shape of the fluid-fluid interface inside it. Diagonal and lateral plane of square capillary were optically viewed using sequential particle tracking techniques and coating thickness of liquid deposited on the channel walls measured. The flow behavior and coating thickness in circular and square channels were compared and it was shown that the coated film fraction increases as the Capillary number increases.

For a wide range of Ca numbers, Thulasidas et al. [33] measured the liquid film thickness in circular and square channels using the same method of Kolb and Cerro [32]. Also a hydrodynamic model for bubble train flow was developed to predict bubble velocity and liquid film thickness by knowing the superficial gas and liquid velocities. Their results showed that at $Ca \sim 0.01$, the thickness of the film in lateral direction is very thin and it is hard to be measured by optical methods. However, the liquid film has not been drained entirely which could be concluded from the observation of the free surface curvature at the corners [33].

For Capillary numbers ranging from 2×10^{-4} to 1×10^{-2}, Fries et al. [35] investigated the gas-liquid distribution in a 2 mm square channel using Laser Induced Fluorescence (LIF) and confocal Laser Scanning Microscopy (LSM). It was observed that in the corner of the channel, the liquid film thickness decreases with reduction of Ca but it remains constant in the lateral direction. Furthermore, their observations showed that 70% of liquid film is distributed in the corners of the channel.

Using the finite-element free surface formulation method, Hazel and Heil [37] investigated the propagation of semi-infinite air bubbles in non-circular pipes. The results showed at small capillary numbers, because of non-uniform distribution of pressure, the liquid phase moves towards the corners of channel. Moreover, it was observed that for low Ca, the bubble cross sectional shape is always non-axisymmetric and the liquid film thickness at the wall of the channel reaches zero.

Taha and Cui [31] numerically investigated the bubble shape, terminal velocity and wall shear stress distributions of elongated bubbles in a 2 mm square channel using volume of fluid (VOF) technique. The results were compared with the experimental data in the literature and showed a good agreement. In a comprehensive study, with the Laser confocal technique, Han and Shikazono [112] measured the local and instantaneous liquid film thickness of semi-infinite Taylor bubbles in microchannels of square cross section. Three working fluids including ethanol, water and FC-40 were used for a wide range of Reynolds and capillary numbers. For water, it was observed that, the liquid film thickness in lateral direction is zero since the water did not wet the surfaces. The final results both for lateral and diagonal film thickness were correlated as a function of Weber and Capillary numbers.

$$R_{dia} = \begin{cases} 1.171 - \dfrac{2.43 Ca^{\frac{2}{3}}}{1+7.28 Ca^{\frac{2}{3}} - 0.255 We^{0.215}} & (for\ Re < 2000) \\[4mm] 1.171 - \dfrac{3869 \dfrac{\mu^2}{\rho\sigma D^{2/3}}}{1+1.156\left(\dfrac{\mu^2}{\rho\sigma D}\right)^{\frac{2}{3}} - 6.70\left(\dfrac{\mu^2}{\rho\sigma D}\right)^{0.215}} & (for\ Re > 2000) \end{cases} \qquad \text{Eq. 2.28}$$

$$R_{lat} = \begin{cases} 1 & (for\ \ R_{dia} > 1) \\ R_{dia} & (for\ \ R_{dia} \le 1) \end{cases} \qquad \text{Eq. 2.29}$$

where R_{dia} and R_{lat} are bubble radius in diagonal and lateral direction, respectively and define as

$$R_{dia} = \sqrt{2} - \frac{2\delta}{D}, \qquad\qquad \text{Eq. 2.30}$$

$$R_{lat} = 1 - \frac{2\delta}{D}. \qquad\qquad \text{Eq. 2.31}$$

Using the experimental data available in the literature, Kreutzer et al. [1] proposed a model for liquid film thickness in diagonal direction. Their results revealed that the liquid film in the corners of square capillaries does not disappear for very low Capillary numbers. By applying a high speed camera, Chaoqun et al. [113] investigated the fundamentals of slug flow in rectangular microchannels with inertia effects. It was observed that for microchannels, inertia effects cause a significant increase in the liquid film thickness. Furthermore, the results showed that with increase of liquid flow, the liquid slug length reduces, which was attributed to a high "leakage flow of the liquid film around the gas bubbles".

Kuzmin et al. [36] studied the three dimensional shape of elongated Taylor bubbles and velocity distribution of surrounding liquid in square channels using the free-energy binary liquid lattice Boltzmann method in the range of the capillary number $0.05 \le Ca \le 6.0$. For liquid film thickness, their results showed good agreement with the experimental data available in the literature.

Warnier et al. [114] considered the bubble and liquid slug lengths and the bubble velocity in a glass microchannel of rectangular cross section and observed the gas hold-up follows the Armand correlation which implies that the liquid film thickness is not dependent upon the bubble velocity. Furthermore, it was shown that for every channel diameter, the liquid film thickness occupies a constant segment of the channel cross sectional area.

As it was briefly summarized, due to the significant role of liquid film in Taylor flow in small channels, a number of studies have been done to measure and calculate the thickness and properties of the liquid film around the Taylor bubbles in circular contactors. However, on one hand, noncircular

channels were subject of a few investigations and on the other hand, almost all of the studies were focused on the measurement of film thickness in micro-sized channels and millimeter-size channels were less considered.

2.6. Summary and conclusion

In this chapter, previous studies were introduced to present the state of the art on the subject of Taylor bubbles in small channels. As it was shown, in general, most of the investigations regarding the behavior of Taylor flow in channels are mainly done in micro-sized or large channels. In detail:

- In case of mass transfer studies of dissolving bubbles, almost all of the studies have been done for channels larger than 12 mm inner diameter. For small channel diameters (5.5 – 8 mm), where the role of interfacial forces on the hydrodynamics and mass transfer of bubbles are not negligible, further investigations need to be made.

- In case of cross sectional shape of channels, there exists a large gap particularly in related aspects of transport phenomena in non-circular channels.

- Regarding the influence of impurities on mass transfer rate of Taylor bubbles in small channels, most attention has been paid so far to the small spherical bubbles in infinite liquid. On the other hand, regarding the influence of surfactant on the liquid film thickness for elongated bubbles in capillaries, almost all of the investigations are theoretical and very few experimental evidences could be found [55]. In addition, among the available theoretical investigations, some of the studies show that surfactant has a thickening effect on the liquid film thickness whereas in others a thinning effect was found [51], [55], [80]. An experimental investigation is needed to determine the validity of available theories.

- Regarding the intensification of mass transport processes for Taylor flow in small channels, it was shown that oscillation/vibration of transferring phases can be a promising approach to intensify mass transfer rate. However, most reported studies were devoted to axial or vertical oscillation of channels, which has some drawbacks for process itself, such as stronger axial

back mixing and decreasing the rise velocity of the gas phase. Therefore, further studies are needed that consider other direction/mode of oscillation/vibration of channels.

- In case of liquid film thickness measurement for Taylor flow in small channels, a number of comprehensive studies have been done to measure the thickness and properties of the liquid film around the Taylor bubbles in circular contactors. However, noncircular channels were not considered adequately specially regarding their increasing application of these channels in monolith reactors.

3. Experimental methodology

3.1.   Introduction

In this chapter a complete description of the employed experimental setup and procedure is given. The details about the devices and equipment are provided, and the operating condition and experimental range of parameters are also presented. Furthermore, detailed information about the X-ray image acquisition process including bubble shape and size measurement in circular and square channels and the tomography technique are provided.

3.2.   Experimental setup

To investigate the mass transfer between a Taylor bubble and the liquid flowing around the bubble the dynamics of the shape of a Taylor bubble was radioscopically monitored. The acquired X-ray images of the bubbles were analyzed with respect to volume, surface area and length of the bubble. The experimental setup is schematically shown in Fig. 3.1.

It consists of the observation section (glass milli-channel), lower and upper liquid reservoirs, a gas injection system, temperature gauges, an X-ray source, a rotary stage for fixation and rotation of the test section, a flat panel X-ray detector, a liquid flow controller system, CO_2 bottles and a liquid flow measurement system. The observation section is a pipe of 300 mm length. Two capillaries of 6.0 and 8.1 mm inner diameter were used to investigate the effect of the hydraulic diameter. The inner diameters of the capillaries were measured by Vernier calipers. The uncertainty in measurement was

obtained as ±0.05 mm. The capillaries are made of borosilicate glass with wall thickness of about 2 mm. Degassed deionized water with electrical conductivity < 0.5 µS/cm, surface tension 72.70×10^{-3} N/m and pH 7.0 was fed into an open-air overhead reservoir. The reservoir was covered by a plastic head to prevent intrusion of dust particles. However, air would dissolve in the water during the experiments. The temperature was fixed at about 292±1 K. A level indicator was installed in the upper reservoir to indicate the hydraulic static pressure.

The glass capillary is placed between the X-ray source and a two-dimensional flat panel X-ray image detector. The capillary is mounted at the hollow shaft of a rotary table which enables rotation between ±180°. Countercurrent liquid flow through the capillary originating from the upper reservoir to the lower reservoir enables the fixation of the bubble at a static vertical position in the capillary. Therefore, the flow rate has to be precisely adjusted. The flow rate is remotely controlled by a motorized needle valve and was measured by calculating the accumulation of outlet liquid inside of an accurate graduated cylinder by a high-resolution camera as a function of time. A Taylor bubble is generated by the injection of some finite amount of gas into the liquid through a metallic needle aligned in parallel with the capillary. The amount of gas injected into the liquid is controlled by a remotely operated fast acting solenoid valve. The various bubble equivalent diameters (1 mm – 25 mm) could be produced by changing the duty cycle parameters of the gas injection valve. Gas is provided either by a gas cylinder (O_2 and CO_2 bottles, 99.99% purity, Air Liquide GmbH) or a pressured air. For reference measurements, the solenoid valve is replaced by a syringe, and a defined volume of gas is inserted into the liquid.

3.3. Procedure of experiments

Before starting the experiments, a high countercurrent flow rate was applied and a large number of bubbles were injected into the liquid to flush the injection needle and pipes and to ensure that they were filled with the injection gas only. At the beginning of the experiments a number of reference images were acquired showing the liquid filled capillary only. A low flow rate was applied at the beginning of the experiment first. Then, a bubble was injected into the liquid. As soon as the

ascending bubble reached the field of view, the motorized valve was actuated to increase the liquid flow and to keep the bubble stationary. A sequence of X-ray images was acquired while the bubble dissolved into the liquid. As the volume of the bubble shrank, the velocity of the bubble changed. Thus, the flow rate was continuously adjusted manually.
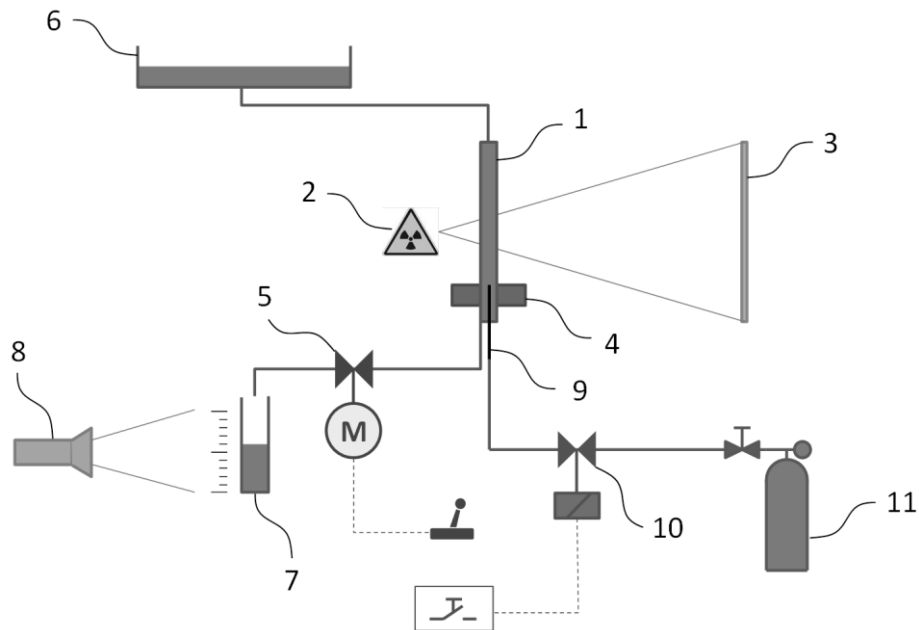
Fig. 3.1 Schematic drawing of the experimental setup: (1) observation section, (2) microfocus X-ray source, (3) flat panel X-ray image detector, (4) rotary table, (5) remotely controlled motorized needle valve, (6) upper reservoir, (7) lower reservoir, (8) video camera, (9) injection needle, (10) fast solenoid valve, (11) gas cylinder.

3.4. X-ray image acquisition

3.4.1. X-ray source

A microfocus X-ray tube (X-RAY WorX XWT-190-TC) equipped with a tungsten high energy transmission target was used as radiation source. The maximum tube voltage is 150 kV at a maximum target power of 25 W. However, a tube voltage of 135 kV and a tube current of 40 µA was used to not exceed 5 W target power and to achieve the smallest focal spot size and thus highest spatial resolution. The X-ray parameters were held fixed during all experiments.

3.4.2. X-ray detector

A two-dimensional flat panel X-ray detector (Perkin Elmer XRD 0822 AP3 IND) equipped with a high efficiency/high resolution cesium iodine (CsI) scintillation screen is used as image detector. The resolution of the detector is 1024 × 1024 px at a pixel size of 200 μm × 200 μm. Thus the detector covers an area of 20 cm × 20 cm. An integration time of 100 ms per image was chosen for the radioscopic measurements. The shrinking Taylor bubble was radioscopically monitored at an exposure time of 100 ms and a frame rate of 5 Hz.

3.4.3. X-ray image processing (circular channel)

From the acquired radioscopic data extinction images, E, were calculated according to

$$E_{ij} = \mu d_{ij} = -log\left(\frac{I_{ij}}{I_{0,ij}}\right),$$
Eq. 3.1

with μd describing the extinction along each individual ray path between the source and detector pixel ij. The reference intensity measured at the detector without any object in the X-ray beam is given by I_0, while I is the measured intensity with the capillary in view.

A single radioscopic extinction image E_{ref} showing the projected section of a glass tube with circular cross section completely filled with water is shown in Fig. 3.2a. Geometric calibration of the X-ray imaging system is best achieved by visualization of an object with known spatial dimensions. The two maxima of the horizontal extinction profile, which was vertically averaged over 600 detector rows, give the positions of the projected inner glass wall of the tube (Fig. 3.2b). The cylindricity of the circular glass channel was checked using the microfocus X-ray computed tomography and the diameter was found to vary by 0.5%, and the inner diameter of the channel was determined to be 5.92 ± 0.03 mm. With the known inner tube diameter all X-ray images were geometrically calibrated to an effective pixel spacing of 27.4 μm ± 0.5%.

Fig. 3.3a exemplarily shows an instantaneous extinction image E_g of a Taylor bubble in countercurrent liquid flow in the circular tube. The bubble was held almost stationary by adjusting the liquid flow rate. The extinction profiles along the center of the projected tube (Fig. 3.3b) are degraded by image noise due to the limited X-ray intensity and the short exposure times. The noise in the images

complicates the extraction of the projected bubble interfaces and thus the measurement of bubble volume, interfacial area and length.

(a)   (b)
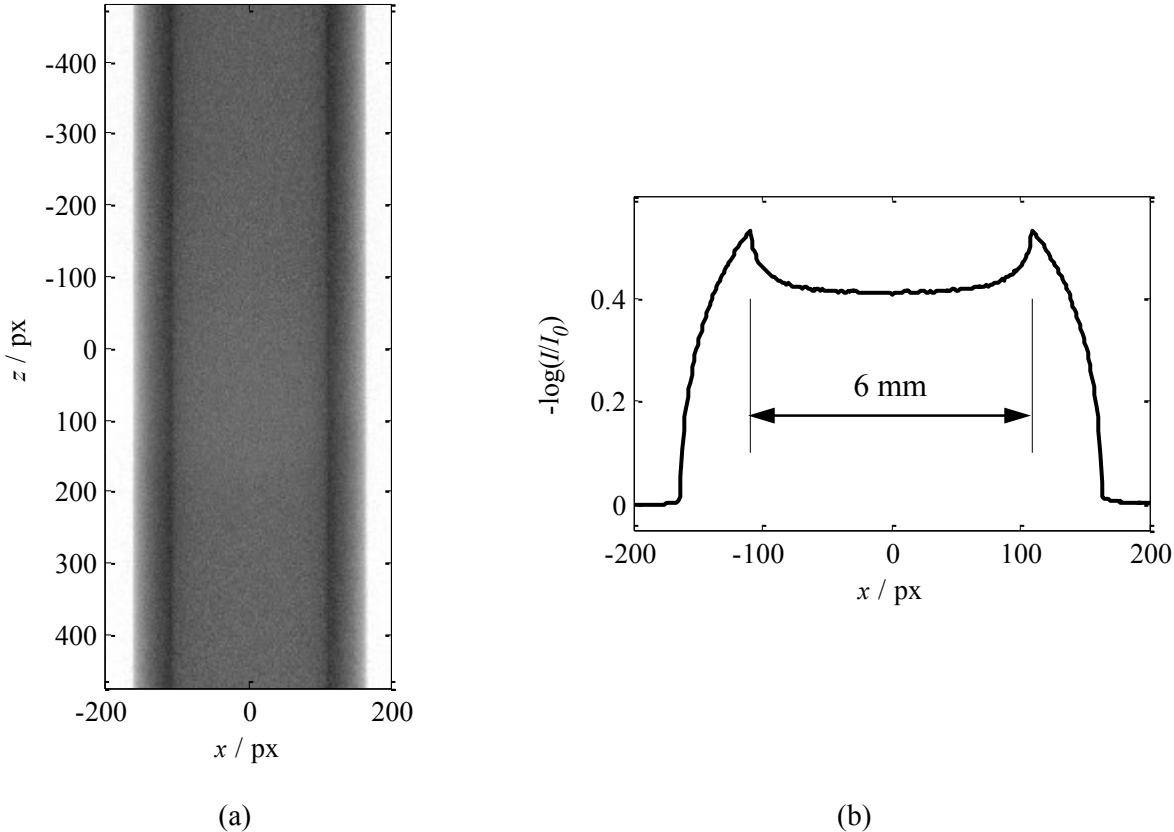
Fig. 3.2 X-ray extinction image of the liquid-filled circular tube (a), and vertically averaged extinction profile for geometric calibration (b).

(a)   (b)
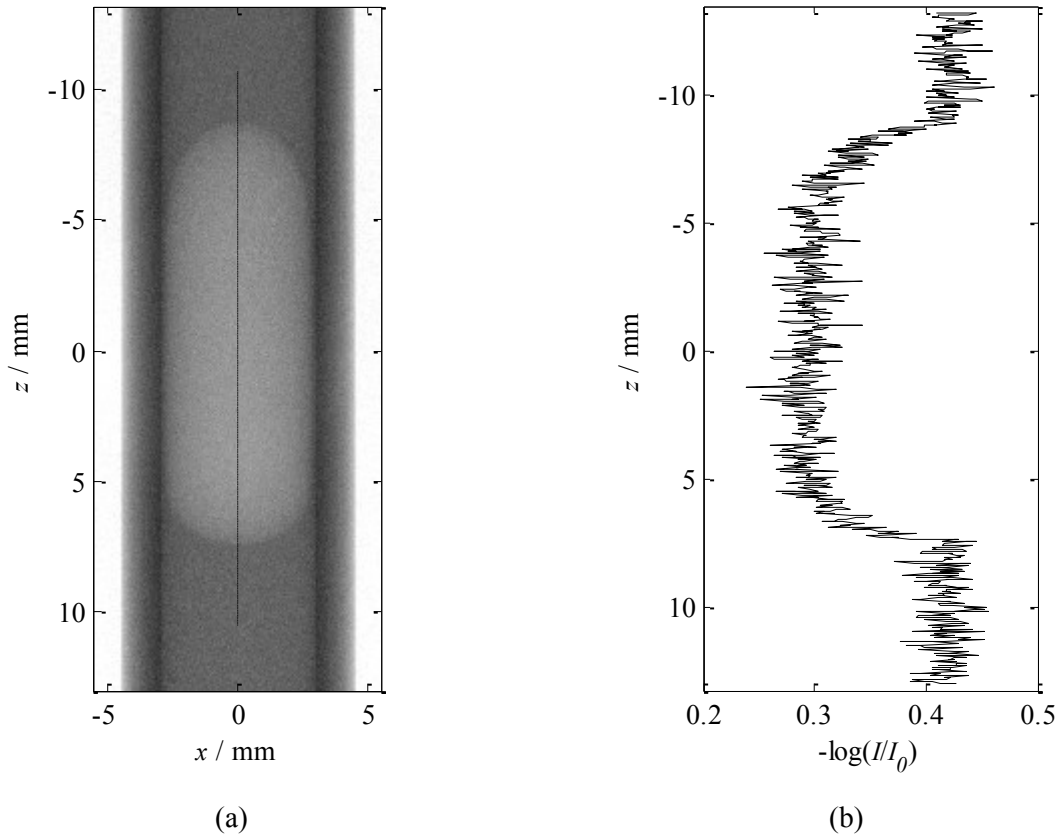
Fig. 3.3 X-ray extinction image of a Taylor bubble in the liquid-filled circular tube (a), and raw extinction profile along the vertical center line (b).

3.4.4. Bubble size measurement (circular channel)

In order to quantify the bubble's length, volume and interfacial area, an extinction image E_b showing the Taylor bubble only is computed by subtraction

$$E_b = E_g - E_{ref},$$ Eq. 3.2

as exemplarily shown in Fig. 3.4a. The two-dimensional projected bubble interface (Fig. 3.4b) is extracted from the image E_b after application of a Gaussian low-pass filter by the algorithm described below. The bubble's length L is computed by the difference of the maximum and minimum z-position of the extracted projected bubble interface. The bubble's volume V_b and the bubble's interfacial area S_b are computed by constructing a solid of revolution from the plane interfacial curve around the tube axis as shown in Fig. 3.4c. Further, for each image the bubble's center of gravity is measured and tracked over time to compute the bubble's velocity.

(a)   (b)   (c)
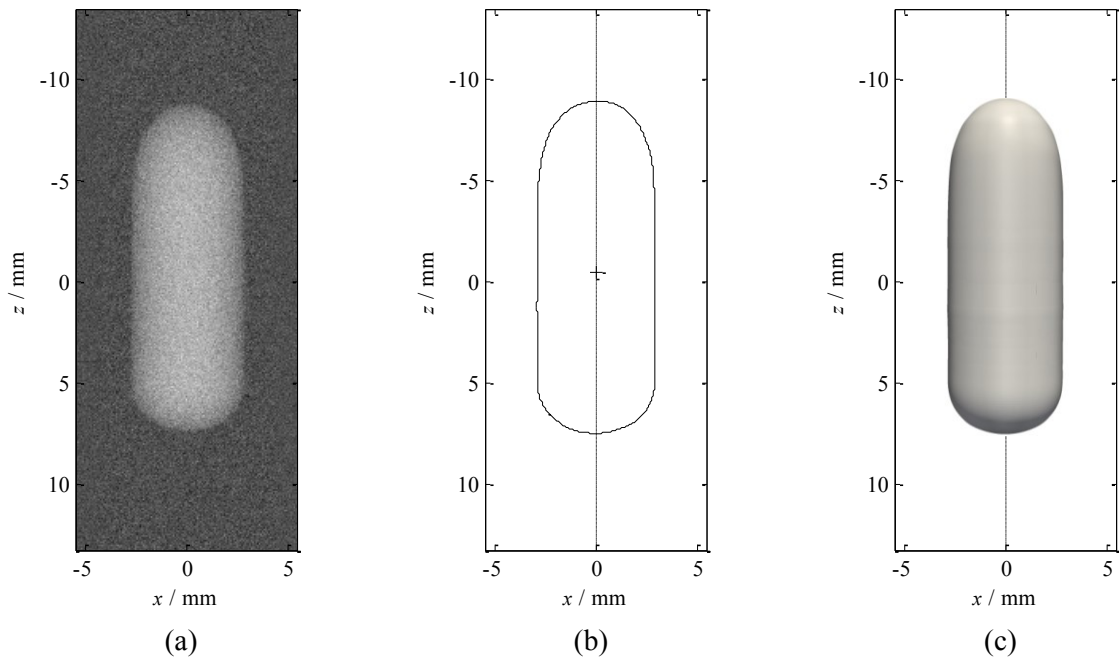
Fig. 3.4 Extinction image of a Taylor bubble only (a) and extracted projected bubble interface (solid line) with axis of revolution (chain dotted line) and the center of gravity (cross marking) (b) and solid body of revolution from the plane interfacial curve around the axis (c).

However, the fixation of the vertical position of the bubble by remote controlling of the flow rate turned out to be rather difficult and slight motion of the bubble occurred during the experiments. Due to the finite exposure times of the X-ray detector the bubble motion causes blurring of the front and rear interface in the bubble projection. This is shown in Fig. 3.5, which displays the X-ray extinction projection of a Taylor bubble under forced (controlled) motion. This blurring results in false measurement of increased bubble volume and interfacial area, since the implemented algorithm only searches for the very edge of the projected bubble. This is shown in Fig. 3.6a for a non-dissolving air bubble with constant volume at different velocities. However, if only the integral extinction $\sum_{ij} E_{ij}$ in each image is considered, no such dependency on the bubble motion can be found (Fig. 3.6b). Therefore, only the development of the integral extinction over time was considered when analyzing the bubble dissolution, and the bubble's volume and interfacial area are computed utilizing calibration function k_V and k_S,

$$V_b = k_V \sum_{ij} E_{ij}$$
<div align="right">Eq. 3.3</div>

and

$$S_b = k_S \sum_{ij} E_{ij} \; .$$

<div align="right">Eq. 3.4</div>

<div align="center">
0 mm/s   6.1 mm/s   19.6 mm/s
</div>
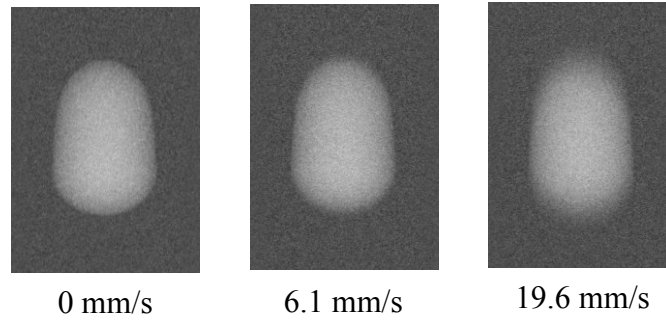
Fig. 3.5 Forced longitudinal motion results in blurred front and rear edges in the X-ray projections of the Taylor bubble.

(a)

(b)
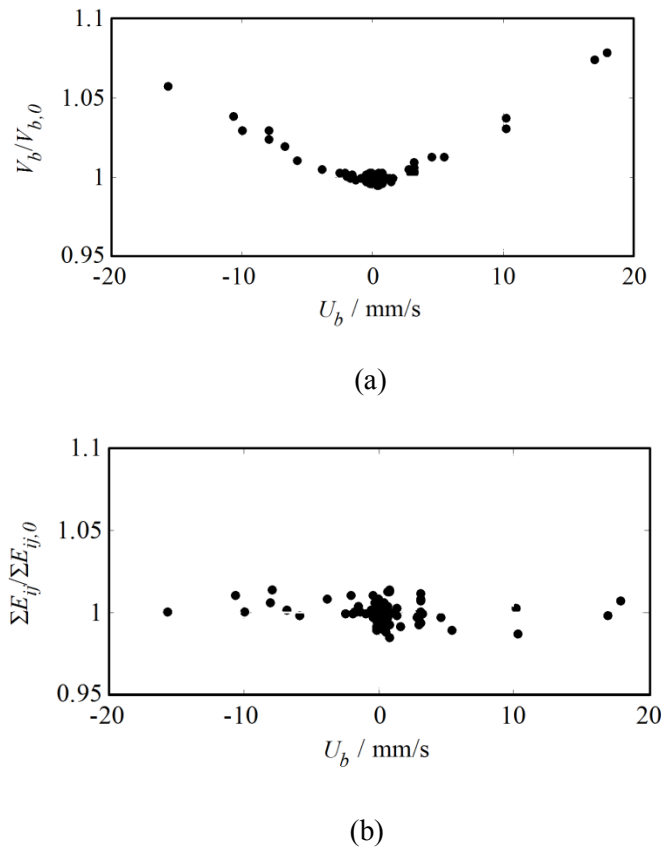
Fig. 3.6 Computed relative bubble volume and relative integral extinction of a Taylor bubble with constant volume for different velocity under forced bubble motion.

3.4.5. Calibration (circular channel)

The bubble's volume and interfacial area in each image E_b were computed utilizing calibration functions k_V and k_S (Eq. 3.3 and 3.4) which were derived from dedicated calibration experiments as

follows. Non-dissolving air bubbles of different size were injected into the liquid filled capillary and were held at a fixed position by application of a countercurrent flow. Since the bubbles were not shrinking, disturbing bubble motion was not present during the calibration measurement. An average extinction image $\overline{E}_b$ of the non-dissolving bubble was generated by integration of 256 single images (Fig. 3.7a), which increased the signal to noise ratio by a factor of 16. To extract the projected bubble interface the image $\overline{E}_b$ was scanned along lines normal to an anticipated interfacial curve. An elliptical curve was fitted to the scanned extinction signal to eventually detect the edge of the projected bubble at the interception of the ellipse with the base line (Fig. 3.7b). Construction of a solid of revolution from the extracted two-dimensional projected interfacial curve enabled precise measurement of the volume and interfacial area of the reference bubbles. The relative error in the measurement of the projected interfacial curve is estimated to be ±1 px, thus resulting in an uncertainty in the volume and interfacial area measurement of $\delta V_b / V_b = 3.8\%$ and $\delta S_b / S_b = 2.3\%$ including the uncertainty of the pixel spacing. Relating the measurements to the integral extinction $\sum_{ij} E_{ij}$ by a linear regression resulted in the factors k_V and k_S.

To achieve a suitable signal to noise ratio either a Gaussian low-pass filter on the short exposure time images or a virtual extension of the exposure time by image averaging was utilized. Therefore, instationary bubble shape fluctuations cannot be resolved by this approach, and the measurement results reflect only parameters related to an averaged bubble shape with a smooth surface. A visual observation of the bubbles inside the capillary verified that, no such small scale shape perturbations were present in the case of the capillaries used here.

<div align="center">(a)</div>
<div align="center">(b)</div>
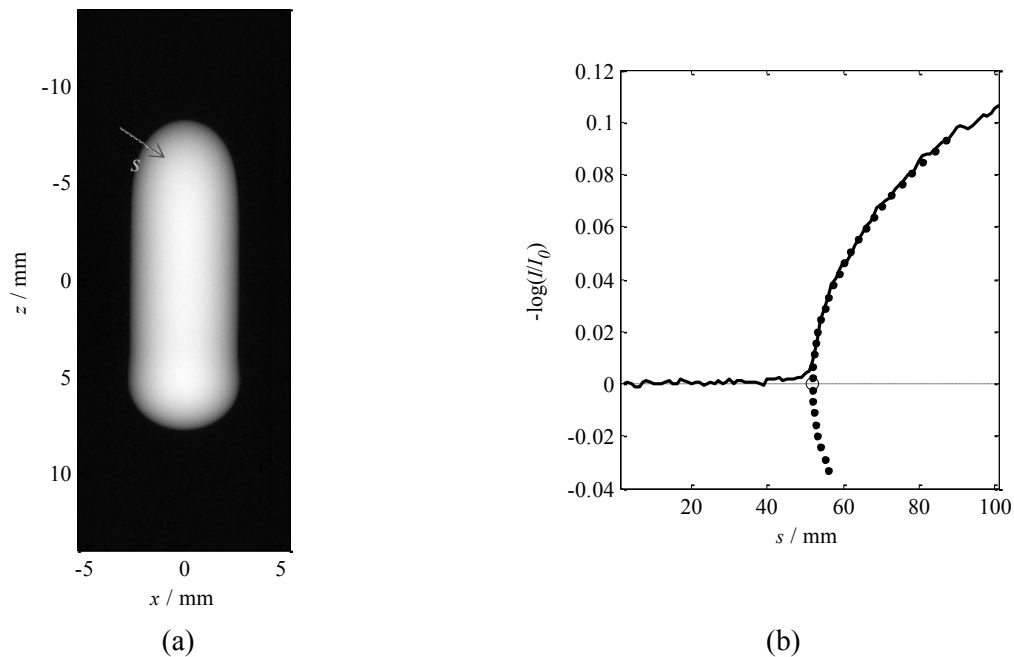
Fig. 3.7 Average extinction image of a non-dissolving Taylor bubble. The arrow indicates a scanline normal to the anticipated projected interface (a) and the fitting of the extinction profile along the scanline to an ellipse curve to extract the location of the interface (circle) (b).

3.4.6. Tomography

For the circular channel, the full three-dimensional bubble shape could be retrieved by rotational expansion of the two-dimensional interfacial curve by revolution around its axis. However, the square channel was aligned in such a way, that only the diagonal projection of the bubble's interface was obtained from the two dimensional image detectors (Fig. 3.8). The straight projection of the bubble's interface however is not accessible by this approach. A reconstruction of the three-dimensional bubble surface by revolution of the extracted plane projected diagonal bubble interface curve eventually will overestimate the bubble's volume and interfacial area, since the bubble is constricted by the planar walls of the square channel. Therefore, a tomography approach was applied to accurately measure the bubble's volume and interfacial area. Since tomographic scans are inherently slow, this technique cannot be applied for dynamic visualization of the fast dissolution process of a CO_2 Taylor bubble in water. Therefore, non-dissolving air bubbles at different sizes were injected into the square channel and their shape was compared with CO_2 bubbles with the same volumes. It was observed that the type of gas (air or CO_2) of Taylor bubbles does not have any influence on the shape bubbles. As a result,

the bubble volume and interfacial area were tomographically measured for each bubble size. The bubble's position was held stationary by application of a remotely controlled countercurrent liquid flow. The channel was rotated by 360°, and 720 projection images were captured at an exposure time of 1000 ms for each image.
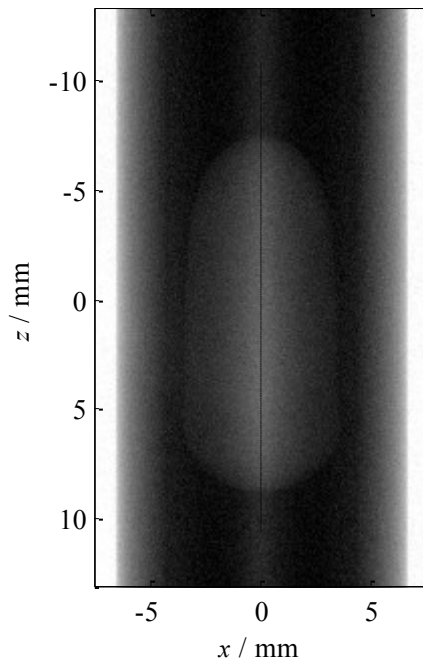
Fig. 3.8 X-ray extinction image showing the diagonal projection of a Taylor bubble in a square tube.

The acquired projection images were reconstructed by proprietary implementation of the three-dimensional filtered back-projection as described by Feldkamp et al. [115]. The reconstruction reveals the three dimensional shape of the Taylor bubble inside the liquid filled square channel. Two-dimensional bubble interfacial curves were extracted from the three-dimensional reconstructed data set at different angular positions (Fig. 3.9). By combining all extracted interfacial curves into a three-dimensional surface representation, the measurement of the bubble's volume and interfacial area was enabled. These measurements were done for several bubble sizes and a second calibration function was developed. The calibration function correlated the three-dimensional bubble volume, $V_{b,3D}$ and interfacial area, $S_{b,3D}$ with both the bubble volume, $V_{b,2D}$, and interfacial area, $S_{b,2D}$, obtained from the radioscopic two-dimensional diagonal projection images, in the form of linear fits,

$$V_{b,3D} = f(V_{b,2D}) = k_{V,3D} V_{b,2D} \qquad \text{Eq. 3.5}$$

$$S_{b,3D} = f(S_{b,2D}) = k_{b,3D} S_{b,2D}. \qquad \text{Eq. 3.6}$$

In these equations $k_{V,3D}$ and $k_{s,3D}$ are calibration constants. The quality of these correlations is limited

by the precision, at which the bubble contour can be extracted from the three-dimensional dataset, and

the uncertainty was evaluated to be lower than 3.97% for bubbles considered here.

The overall uncertainty in the measurement in $V_{b,3D}$ is governed by including the uncertainty of all

image processing steps and including an uncertainty due to the geometric calibration of the

tomographic imaging setup, and results in the maximum error in the measuring range of lower than

5.09%.

(a)

(b)

(c)
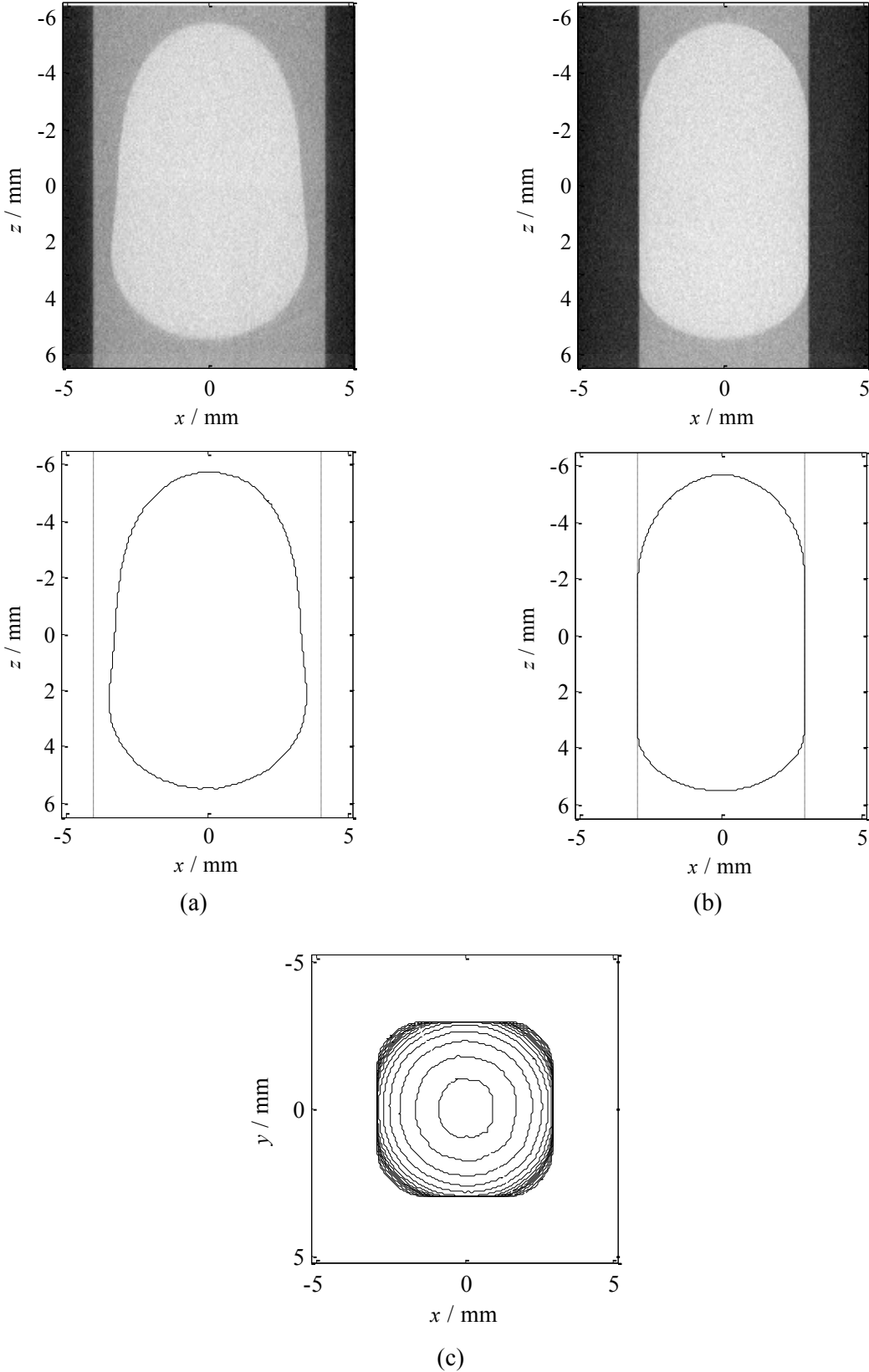
Fig. 3.9 Vertical cross sectional images and the projected gas-liquid interface (a,b) and horizontal isocontour plot (c) of the non-dissolving Taylor bubble in the square channel.

4. Shape and mass transfer of Taylor bubbles in circular and square milli-channels

4.1. Introduction

In this chapter, the shape and dissolution rate of an individual elongated Taylor bubble, whose motion is governed by the tube walls, was investigated in channels of 6 mm and 8 mm inner diameter. Both CO_2 and O_2 bubbles were investigated. The bubbles were held stationary using the technique of Schulze and Schluender [14] and the overall liquid-side mass transfer coefficient was determined from microfocus X-ray images with high accuracy. Furthermore, mass transfer measurement for stagnant Taylor bubbles in a small square channel via measurement of the dissolution rate of an individual elongated bubble of carbon dioxide into water was performed. As a measurement technique we used high resolution X-ray radiography and tomography. The changes in the size of the bubble at constant pressure obtained from the high-resolution X-ray images were used to calculate the liquid-side mass transfer coefficient. The bubbles were continuously monitored by hydrodynamic fixation of the bubble in a down flow of the liquid. The results are compared with the data for circular channels.

4.2. Bubble shape

4.2.1. Circular channel

An example of bubble images from three dimensional calculations in a 6 mm diameter channel is shown in Fig. 4.1. The nose and tail of the large Taylor bubbles are stable and no oscillations were observed. For smaller bubbles there is some small shape oscillation but for bubbles with equivalent diameter below the channel diameter, strong zig-zag movement and shape oscillations were observed.

4.2.2. Square channel

The bubble's volume and interfacial area can be measured by extraction of a single 2D contour profile and subsequent virtual rotation of this profile around the channel's axis under the assumption of rotational symmetry of the bubble in the circular channel. However, this procedure is not applicable in the case of the square channel where the bubble is not axially symmetric. Therefore, five different size, non-dissolving reference air bubbles were tomographically scanned and their volume and interfacial area was measured (Fig. 4.2). Bubble sizes were limited to equivalent bubble diameters, d_{eq}, larger than the channel diameter, $d_{eq} > D$, with d_{eq} being the diameter of an equivalent rigid sphere with the same volume

$$V_b(d_{eq}) = \frac{\pi}{6} d_{eq}^3. \qquad\qquad \text{Eq. 4.1}$$

For bubbles with $d_{eq} < D$ notable bubble shape oscillations occurred, which made tomography measurements unfeasible.

d_{eq} = 9.60 mm	d_{eq} = 8.66 mm	d_{eq} = 7.33 mm
V_b = 0.463 ml	V_b = 0.340 ml	V_b = 0.206 ml

d_{eq} = 6.31 mm	d_{eq} = 5.23 mm	d_{eq} = 4.61 mm
V_b = 0.131 ml	V_b = 0.075 ml	V_b = 0.052 ml
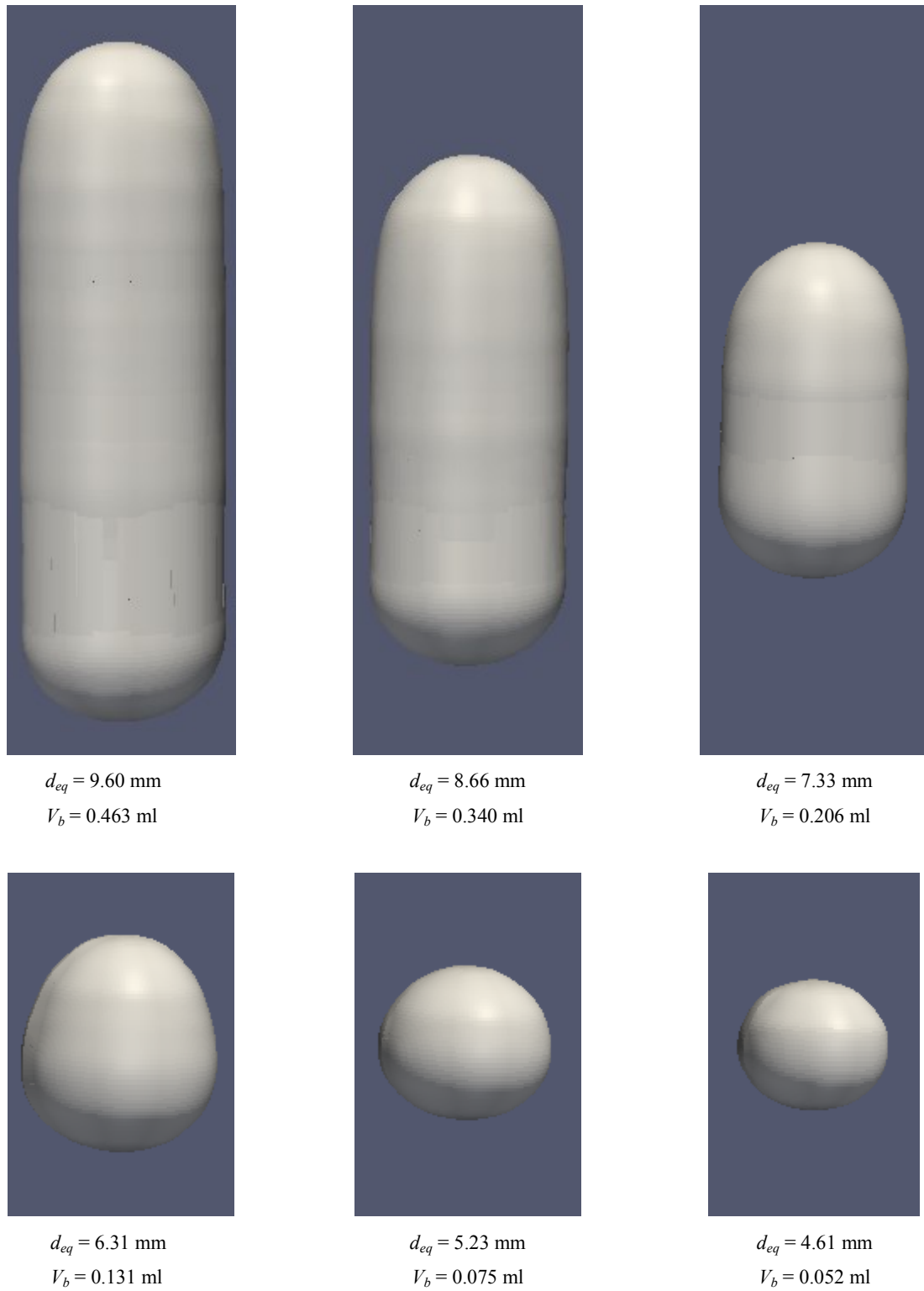
Fig. 4.1 Bubble images from three dimensional calculations in 6 mm diameter circular channel.

$V_b = 0.670$ ml $V_b = 0.477$ ml $V_b = 0.281$ ml $V_b = 0.190$ ml $V_b = 0.119$ ml
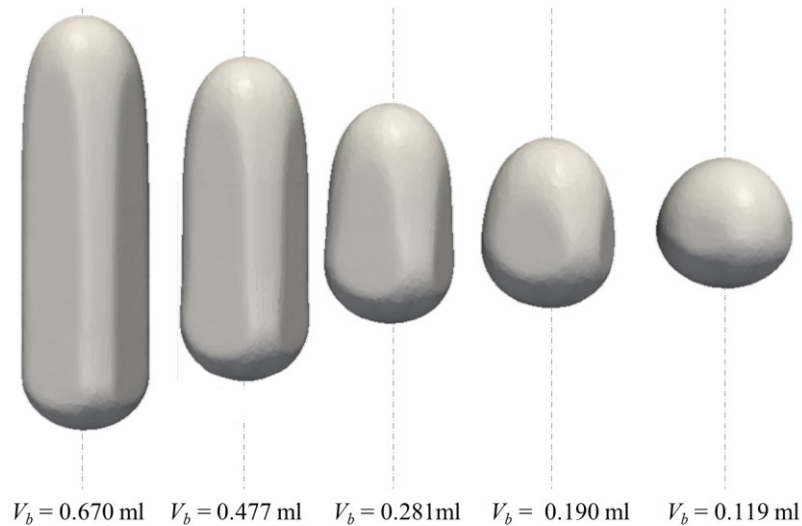
Fig. 4.2 3D shape and volume of a non-dissolving air Taylor bubble at different bubble volumes in countercurrent water flow in a square channel with hydraulic diameter $D = 6$ mm.

4.3.　Bubble free rise velocity

Fig. 4.3 shows an exemplary image from the videometric monitoring of Taylor bubble's position in the circular tube. The videometric monitoring of Taylor bubble's position enabled the measurement of the bubble free rise velocity. Here the term "free" rise velocity is used to mention that the rise velocity of bubbles is measured in absence of any co- or counter current liquid flow and bubbles rise just due to the buoyancy. The velocity of a freely rising Taylor bubble in the circular tube was measured utilizing a CCD video camera (AVT Pike F-100B) which continuously monitored the bubble's position over a height-range of 100 mm at moderately high frame rates of 231.8 frames per second and an effective pixel resolution of 104 μm.
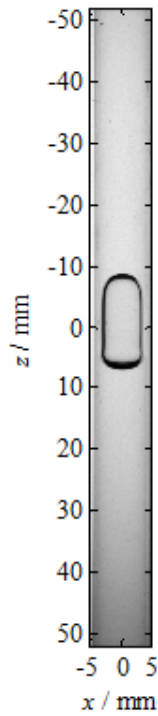
Fig. 4.3 An exemplary image from the videometric monitoring of Taylor bubble's position in the circular tube for the measurement of the bubble free rise velocity.

Fig. 4.4 shows the measured bubble rise velocity for 6 mm and 8 mm capillaries in comparison with other data available in the literature. The maximum uncertainty in measured bubble rise velocity is estimated to be 1.09%. As it can be seen, the rise velocity strongly depends on the channel diameter. When the channel diameter decreases the bubble rise velocity also decreases. This can be attributed to the interaction effect of viscous and interfacial stress on one hand and inertial and gravitational stresses on the other hand. It was shown analytically by Bretherton [102] that elongated bubbles in circular cross section channels will not raise if [1]

$$Bo = \frac{\rho g D^2}{\sigma} < 3.368, \quad\quad\quad\quad\quad\quad\quad\quad\text{Eq. 4.2}$$

where Bo is the Bond number, which is the ratio of buoyancy to surface tension forces. For our system this implies that the channel size should be larger than 5 mm to have free rising bubbles and explains the strong decrease of the rise velocity when the channel diameter approaches 5 mm. Furthermore, Fig. 4.4 shows that rise velocity depends on bubble equivalent diameter. For a fixed channel diameter

the rise velocity increases with bubble diameter but from a certain point on it does not change anymore. Hosoda et al. [28] defined this size as a criterion for definition of Taylor bubbles.
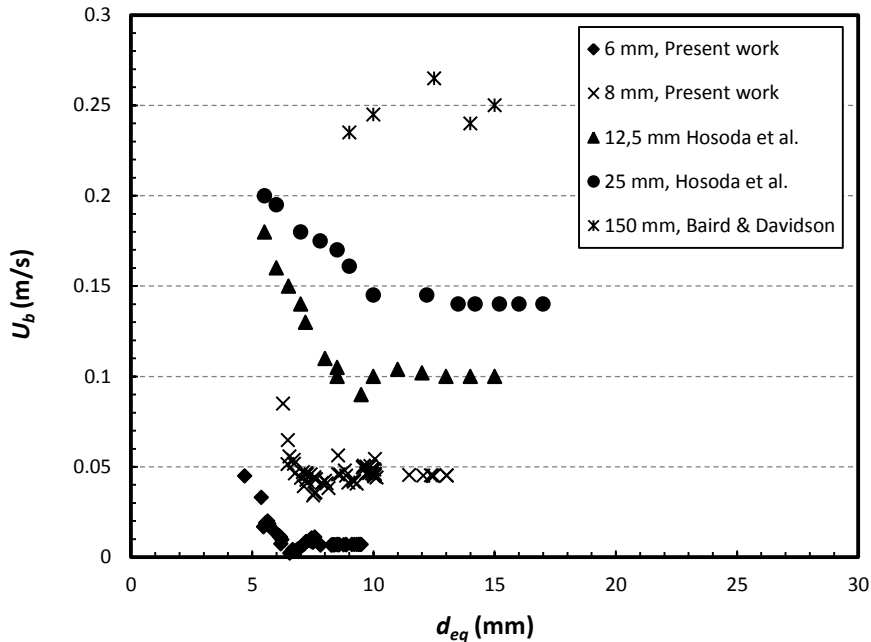
Fig. 4.4 Bubble rise velocity as a function of bubble equivalent diameter.

Fig. 4.5 shows the measured rise velocity of a freely rising Taylor bubble in circular and square channels as a function of bubble size ratio. The prediction of the correlation proposed by White and Beardmore [116] is also presented in Fig. 4.5. This correlation is valid only for cylindrical bubbles in circular pipes, therefore it is not applicable for bubble lengths smaller than the channel diameter. As it can be seen there is a good agreement between our measured data and this correlation. As it is shown, for small bubbles the rise velocity strongly depends on the bubble size and increases with decrease of bubble length (in circular channel when $d_{eq}/D < 1.1$, in square channel when $d_{eq}/D < 1.2$), while it remains constant for large bubbles (in circular channel when $d_{eq}/D > 1.2$, in square channel when $d_{eq}/D > 1.35$) and there is a transition region in between. For a better understanding about the effect of bubble size and shape on the bubble rise velocity, the corresponding bubble shapes are presented in Fig. 4.6. For a circular channel in the mass transfer measurement experiments, the bubble shows a transient behavior in this region and because the rise velocity of the bubble varies significantly, it was difficult to hold the bubble at a fixed position. However as it is shown in Fig. 4.5, this trend was

damped in square channel and despite the rise velocity was three times higher than in circular channel, the control of bubbles was considerably easier.

Fig. 4.5 Bubble rise velocity as a function of bubble size ratio.

(a)	(b)	(c)	(d)	(e)
$d_{eq}/D = 1.494$	$d_{eq}/D = 1.286$	$d_{eq}/D = 1.204$	$d_{eq}/D = 1.109$	$d_{eq}/D = 1.029$
$L/D = 2.728$	$L/D = 1.864$	$L/D = 1.634$	$L/D = 1.279$	$L/D = 1.121$

Circular channel

(f)	(g)	(h)	(i)	(j)
$d_{eq}/D = 1.680$	$d_{eq}/D = 1.512$	$d_{eq}/D = 1.352$	$d_{eq}/D = 1.206$	$d_{eq}/D = 1.153$
$L/D = 2.737$	$L/D = 2.190$	$L/D = 1.764$	$L/D = 1.344$	$L/D = 1.206$

Square channel
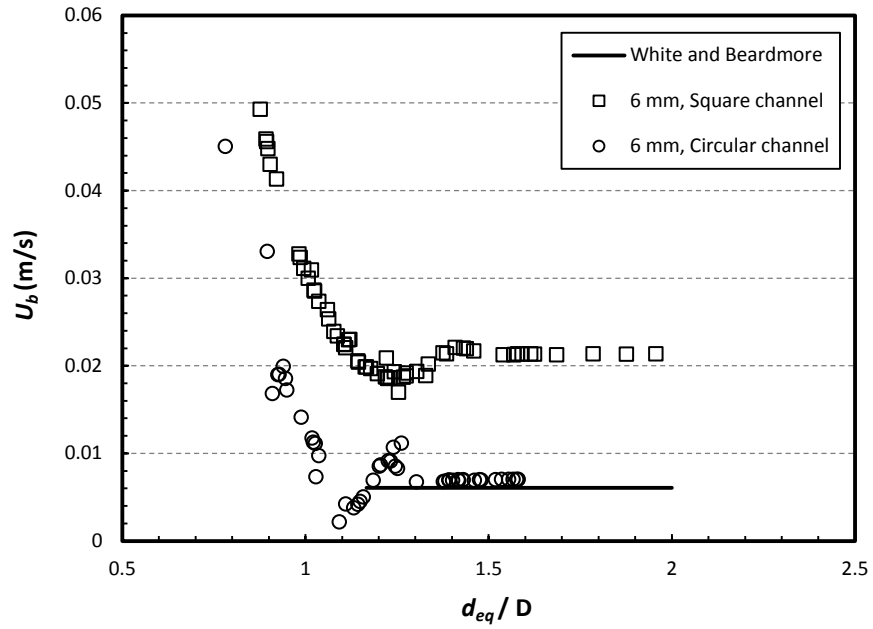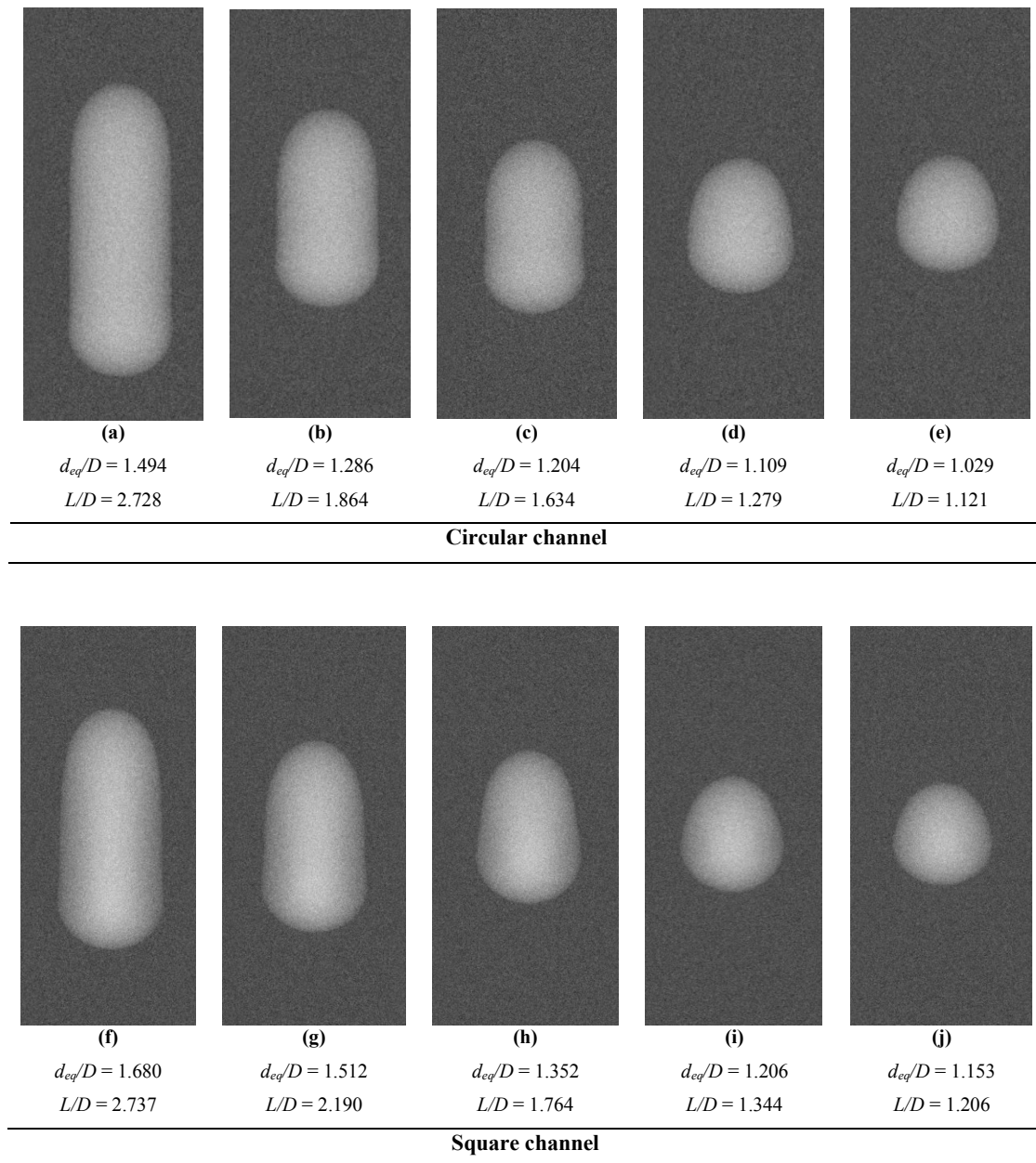
Fig. 4.6 Radioscopic images of bubbles of different size.

4.4. Gas dissolution model

For a bubble of soluble gas absorbing into a liquid, the resistance to mass transfer in the gas phase is negligible with respect to the resistance in the liquid phase under the prevailing conditions [15]. Therefore the rate of mass transfer is proportional to the difference of interface and bulk concentration of liquid phase:

$$-\frac{dn}{dt} = k_L A_{eq}(C^* - C).$$

Eq. 4.3

In this equation n is the total moles of gas phase (CO_2) inside the bubble, t the time, C^* the concentration of gas at the interface and C concentration of gas in the liquid bulk. Assuming the equilibrium at the interface by Henry's law and because $C << C^*$, we have

$$\frac{dn}{dt} = -k_L A_{eq} \frac{C_L P y}{H - P y},$$

Eq. 4.4

where H is the Henry's constant, C_L the water molar concentration, y the mole fraction of CO_2 inside the gas phase and P the pressure inside the bubble calculated by

$$P = P_{atm} + \rho_L g h + \frac{4\sigma}{d_{eq}}.$$

Eq. 4.5

Here P_{atm} is atmospheric pressure, h the distance from the liquid surface in the upper reservoir and center of the liquid, which is constant for all experiments, and σ stands for surface tension of liquid. The contribution of Laplace pressure can be neglected (lower that 0.03%) because the bubble size is relatively large. Due to atmospheric pressure of the bubble we can assume that the gas phase follows the ideal gas law, therefore we can replace dn/dt in terms of V_b (volume of bubble) as

$$\frac{dn}{dt} = \frac{P}{RT} \frac{dV_b}{dt},$$

Eq. 4.6

where R is the universal gas constant and T the gas temperature.

Hosoda et al. [28] have shown that for the first several ten seconds from the injection of the bubbles the CO_2 mole fraction inside the bubbles can be considered as unity. Therefore by assuming y as unity and by combining Eq. 4.4, 4.5 and 4.6 we have

$$k_L = -\frac{1}{A_{eq} RT} \frac{H - P}{C_L} \frac{dV_b}{dt}.$$

Eq. 4.7

The mass transfer was calculated by applying a difference scheme to determine dV_b/dt. The values of the physical properties are given in Table 4-1.

Table 4-1 The values of constant parameters

Parameter	Value (at 298 K)
Density (ρ)	998.2 (kg/m^3)
Henry constant for CO_2 (H)	189 (MPa)
Water molar concentration (C_L)	55.4 (kmol/m^3)
Molecular diffusivity for CO_2 in water (D_c)	1.6×10^{-9} (m^2/s)

4.5. Bubble dissolution

Fig. 4.7 and Fig. 4.8 quantitatively describes the long term dissolution of CO_2 bubbles with different initial volumes in circular and square channels under the same experimental conditions. The channel hydraulic diameter is 6 mm in all cases. As it can be seen, despite the different initial volumes of the bubbles, they show the same trend for the dissolution rate and after a few ten seconds the net rate of mass transfer becomes zero and the bubble size remains constant. Then, the CO_2 concentration in the gas phase is in equilibrium with the CO_2 concentration in the liquid phase. Since there is some dissolved air (mainly nitrogen and oxygen) in the liquid phase, its desorption from the water causes a conjugate flow and enrichment of these gases in the bubble [10],[28]. The final volume of bubbles is directly related to their initial volume. That is in comparison with small bubbles, large bubbles with higher initial volume have more time and larger interfacial surface area to receive dissolved air from the liquid.
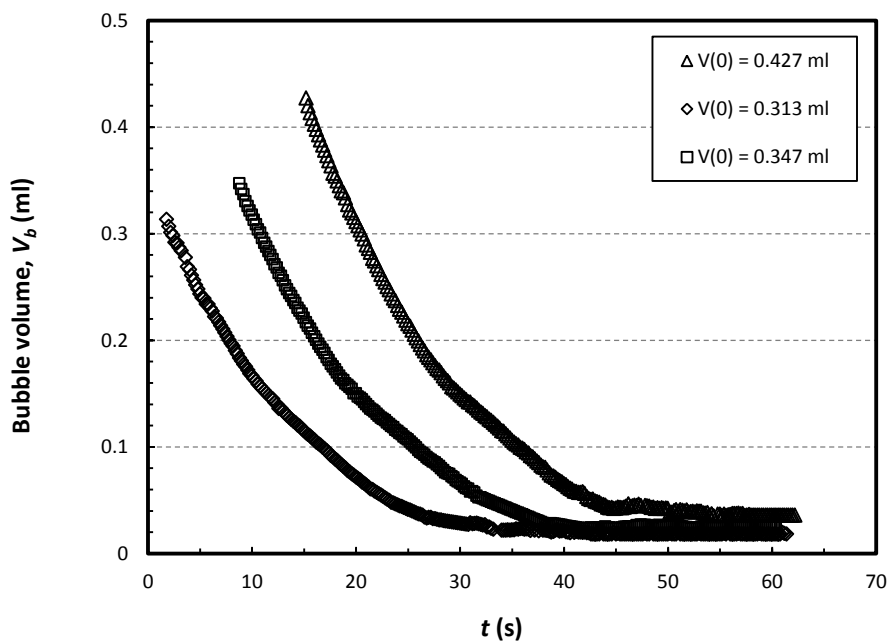
Fig. 4.7 Long term dissolution of three CO_2 bubbles with different initial volumes.
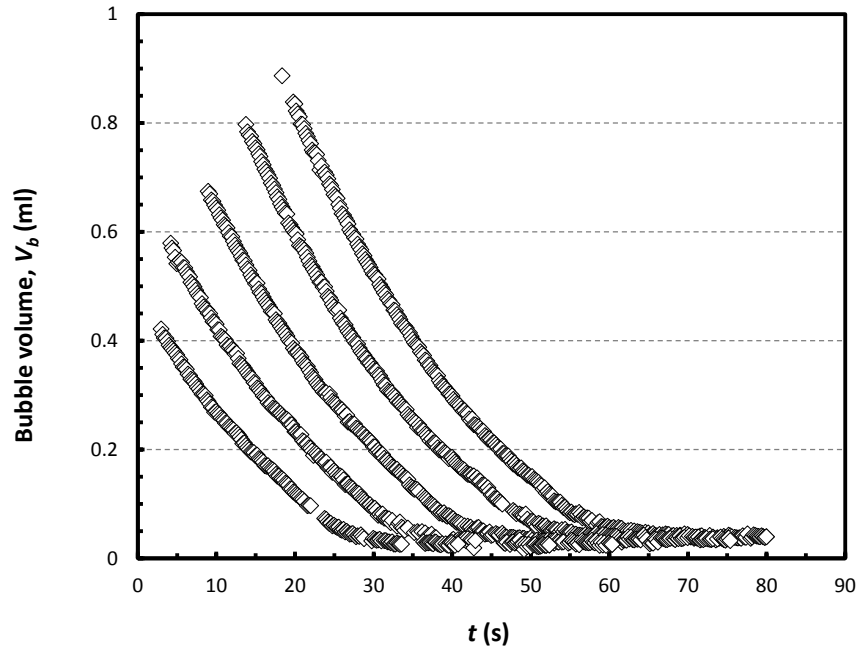
Fig. 4.8 Long term dissolution of CO_2 bubbles with different initial volumes in the square channel.

Fig. 4.9 shows the comparison between the dissolution curve of CO_2 Taylor bubbles in circular and square channels. As it can be seen the trend of the dissolution curves of square channels is more even while the dissolution curves of circular channels show some distinguishable changes in the slope.

For a better comparison, the rate of volume change of bubbles for all the experiments which shows the rate of mass transfer, are presented in Fig. 4.10 as a function of time and in Fig. 4.11 as a function of bubble size. For the bubbles with the sizes larger than the channel diameter ($d_{eq}/D > 1$), the rate of bubble dissolution is relatively linear in square channels, while it is not linear in circular channel. Furthermore, both channels show a sudden change in the dissolution behavior after a certain time (Fig. 4.10). This sudden change occurred when the bubble size ratios, d_{eq}/D, reach between $1.10 - 1.15$ for the circular channel and between $1.25 - 1.30$ for the square channel. This observation is in accordance with results of bubble rise velocity measurements where there is a transition region between a constant rise velocity and an increasing velocity. This transition behavior is attributed to the change in the hydrodynamics of the Taylor flow in small channels.
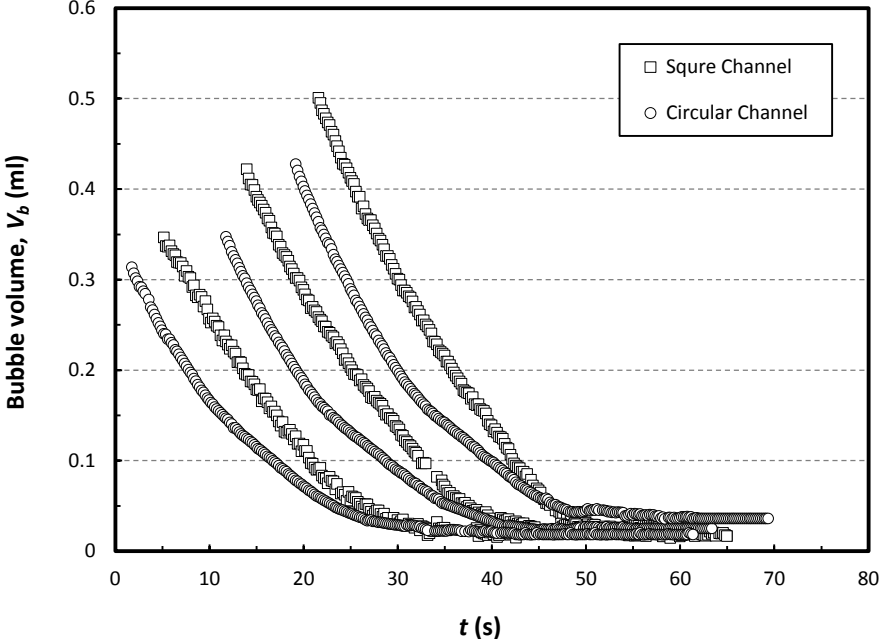
Fig. 4.9 Comparison of long term dissolution of CO_2 bubbles in circular and square channels.
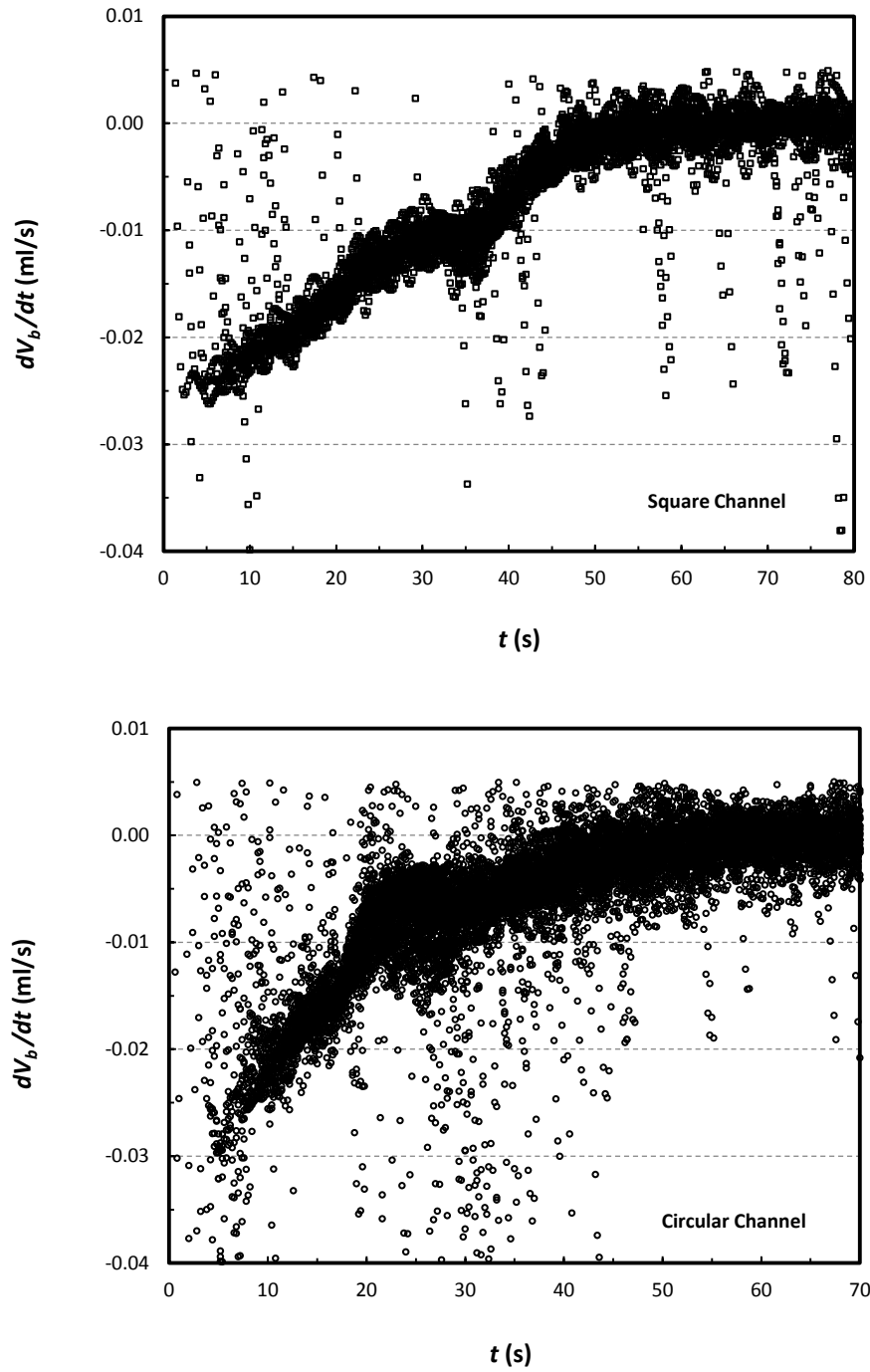
Fig. 4.10 Cumulative data for the rate of volume change of bubbles as a function of time.
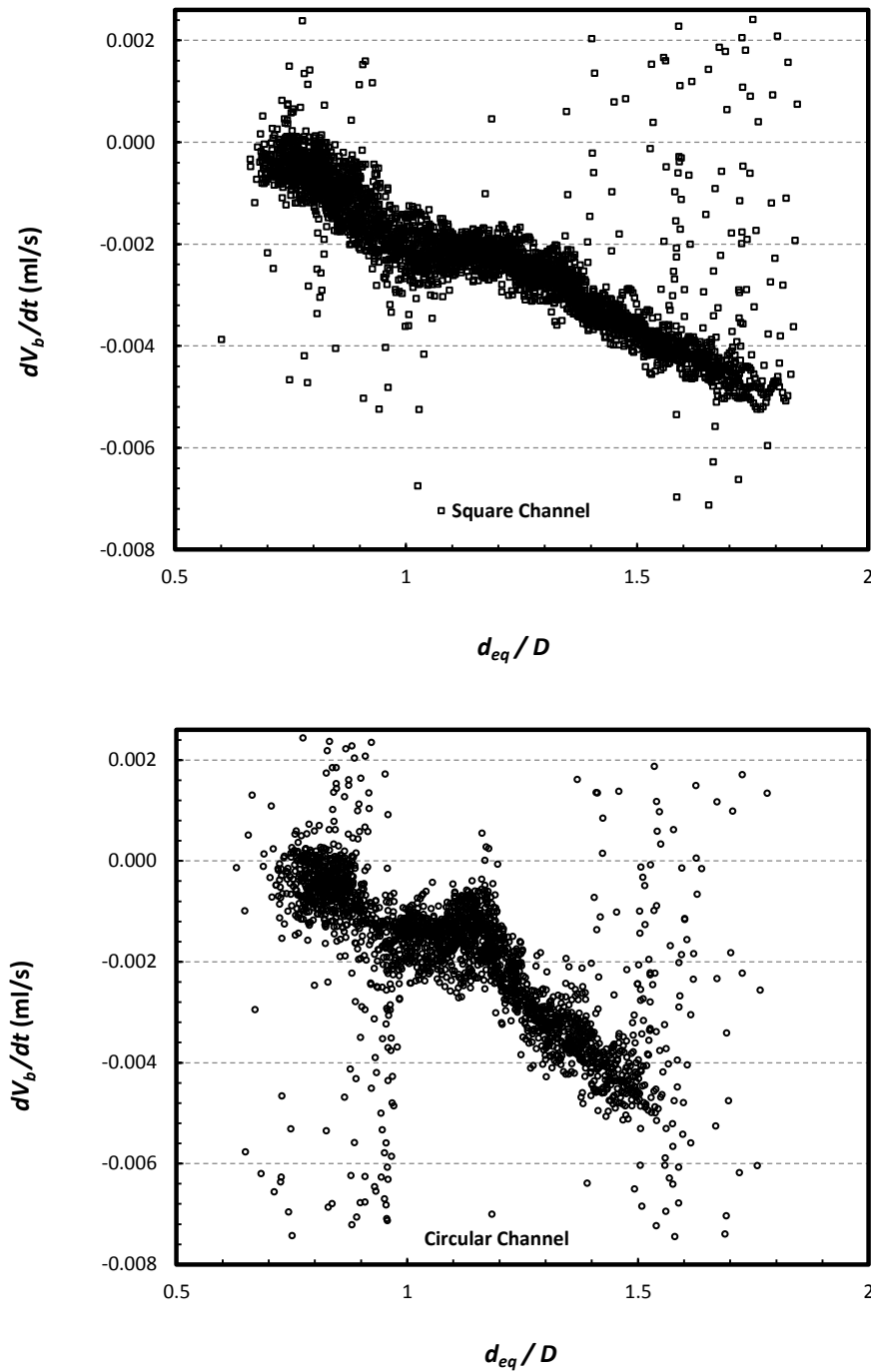
Fig. 4.11 Cumulative data for the rate of volume change of bubbles as a function of bubble size ratio.

4.6. Mass transfer coefficient

4.6.1. Circular channel

The liquid-side mass transfer coefficients k_L according to Eq. 4.7 for stagnant single bubbles in downward flowing water are compared with available data in the literature in Fig. 4.12. The continuous line shows the prediction of correlation proposed by Niranjan et al. [16] (Eq. 2.10) which

is based on the theory of Van Heuven and Beek [15]. The filled dots are experimental data extracted from Filla [10] in a 28 mm pipe. He used fine aluminum powder in the liquid phase and observed that aluminum particles accumulate at the end of bubbles and make a stagnant part at the tail of bubbles. He showed that for bubbles with $L/d_{eq} < 2$ a large portion of interface of bubbles is stagnant while this stagnant portion reduced as the bubble becomes larger.

As it can be seen our measured data, which are from a 6 mm diameter channel, show a better consistency with the experimental data of Filla [10], in comparison with the data predicted by the correlation developed by Niranjan et al. [16]. The reason may be from the fact that the correlation developed by Niranjan et al. [16] is based on the experimental data of single CO_2 bubbles dissolving not only in water but also in different aqueous solutions of glycerol. As it is known, the dissolution rate of CO_2 in water is considerably higher than its dissolution in glycerol [16].
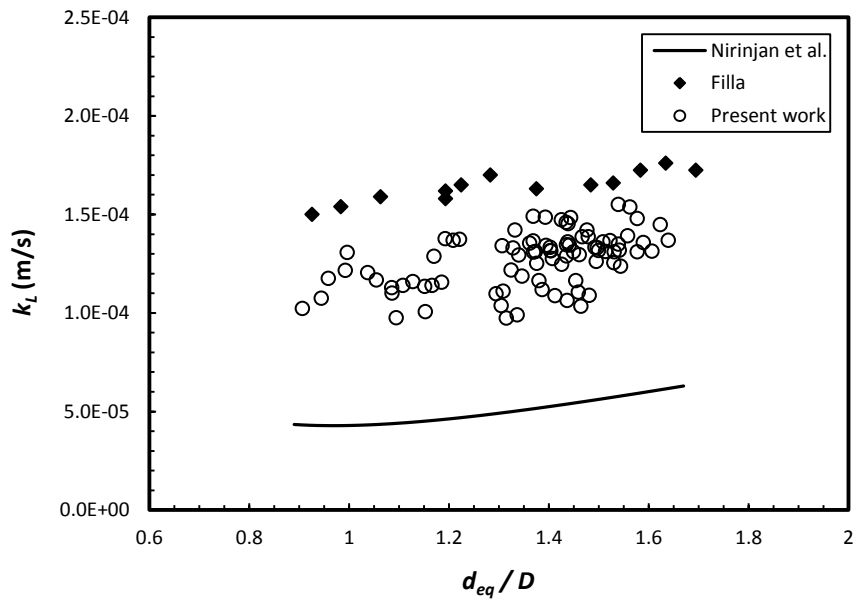
Fig. 4.12 The liquid-side mass transfer coefficients k_L for stagnant single bubbles.

4.6.2. Sherwood number

The modified Sherwood numbers versus the ratio of equivalent bubble diameter over channel diameter d_{eq}/D are shown in Fig. 4.13a,b for the 6 mm and 8 mm channel, respectively. The empirical correlations for Sh^*, Eq. 2.10 proposed by Niranjan et al. [16], Eq. 2.11, Abe et al. [24] and Eq. 2.12, Hosoda et al. [28] are also presented in the Fig. 4.13. The Sherwood number becomes greater with

increasing d_{eq}/D. All the correlations show the same trend. However, there are large errors between their predictions and experimental values for our measurement. This can be due to different channel diameters that each correlation is valid. For example Hosoda's empirical correlation, which shows smallest deviations among the presented correlations, is valid for the pipe diameters 12.5, 18 and 25 mm. As a result, the available correlations cannot be used for the present system and a new correlation should be determined.

Regarding the functional form of Sh, Niranjan et al. [16] used the form of correlation developed by Calderbank et al. [117] but using the pipe diameter D as the length scale and showed that for elongated bubbles Sh is related directly to the $Pe^{0.5}$. Hosoda et al. [28] discussed the dependency of Sh for spheroidal, wobbling and Taylor bubbles and concluded that the ratio $Sh/Pe^{0.5}$ is dependent on d_{eq}/D [28] as

$$Sh/Pe^{0.5} = f\left(\frac{dD}{A}, \frac{L_b}{D}, \frac{d_{eq}}{D}\right) = f\left(\frac{d_{eq}}{D}\right).$$ Eq. 4.8

However, to calculate the mass transfer coefficient from elongated bubbles, it is required to know the product of $k_L A$ [10]. Therefore, the data were correlated in the form of modified Sh^* as a function of $Pe^{0.5}$ and d_{eq}/D. Fig. 4.14 shows the measured data both for 6 mm and 8 mm channels. The curve that best describes the data is

$$Sh^* = \left(23.003(d_{eq}/D)^2 - 38.623(d_{eq}/D) + 23.591\right)Pe^{0.5}$$ Eq. 4.9

for $0.8 < (d_{eq}/D) < 1.6$ or $0.75 < (L/D) < 3.6$

which is valid for the mass transfer from single elongated bubbles in water for milli-channels with a diameter D, ranging from 6.0 mm to 8.0 mm.
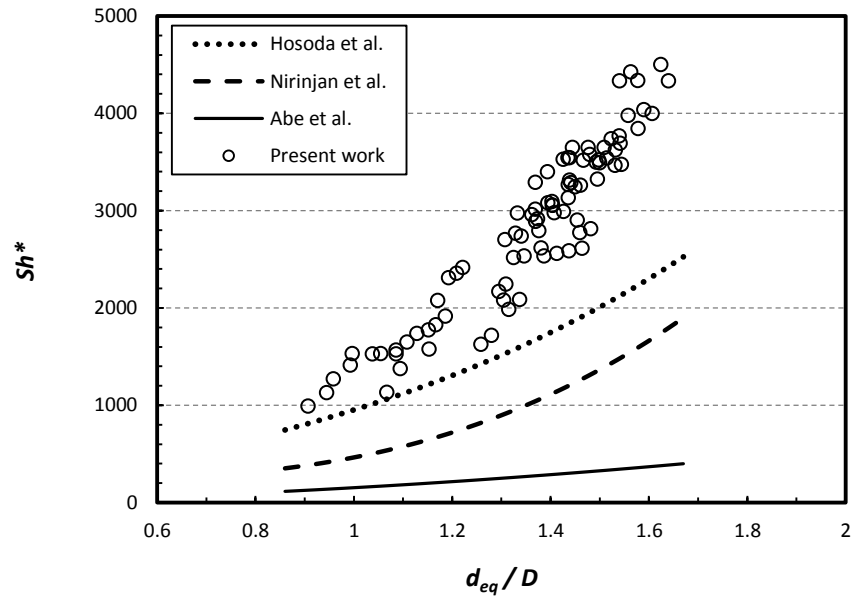
(a)
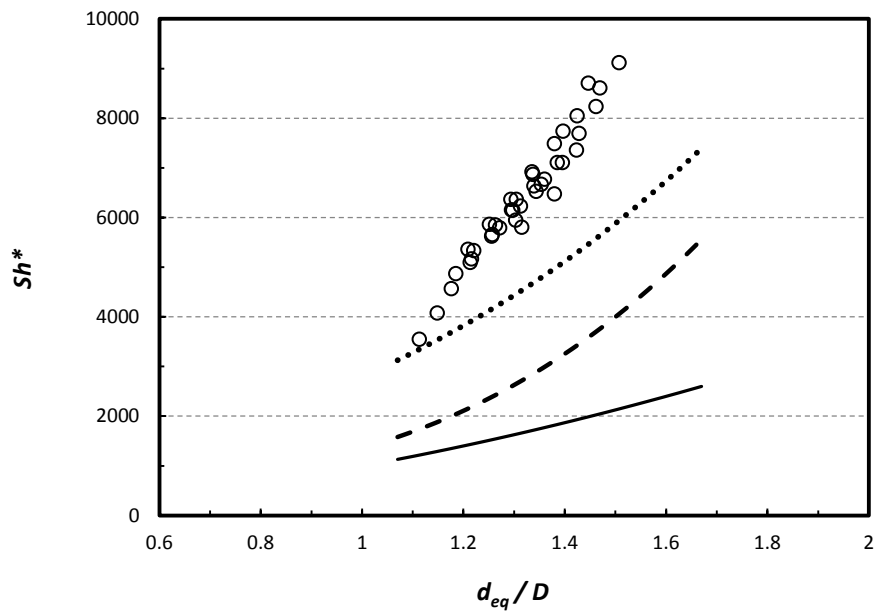
(b)

Fig. 4.13 The modified Sherwood numbers versus the bubble size ratio 6 mm channel (a) and a 8 mm channel (b).

Fig. 4.15 shows a comparison of the new correlation with our experimental data and available experimental data from the literature. The mean absolute error is 9.6% and the maximum deviation is lower than 29%. As it can be seen good agreement exists between the predicted and measured data particularly for smaller pipe sizes. However, as it was mentioned before, the proposed correlation is developed based on the experimental data for 6 mm and 8 mm channels for which Bo numbers are in the range of $4 < Bo < 9$. Therefore, for channels with Bo numbers much larger than 9 where the role of

surface tension stresses are not comparable with the inertial and gravitational forces, this correlation cannot be applied. As a result the proposed equation predicts at best for $4 < Bo < 9$ and $0.8 < d_{eq}/D < 1.6$ ($0.75 < L/D < 3.6$).
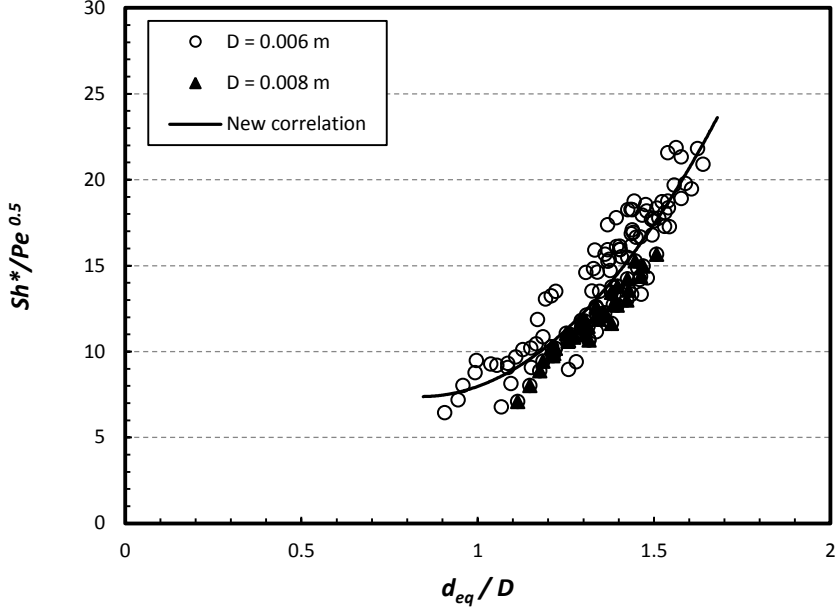
Fig. 4.14 The experimental data both for 6 mm and 8 mm channels in the form of $Sh^*/Pe^{0.5}$ as a function of the bubble size ratio.
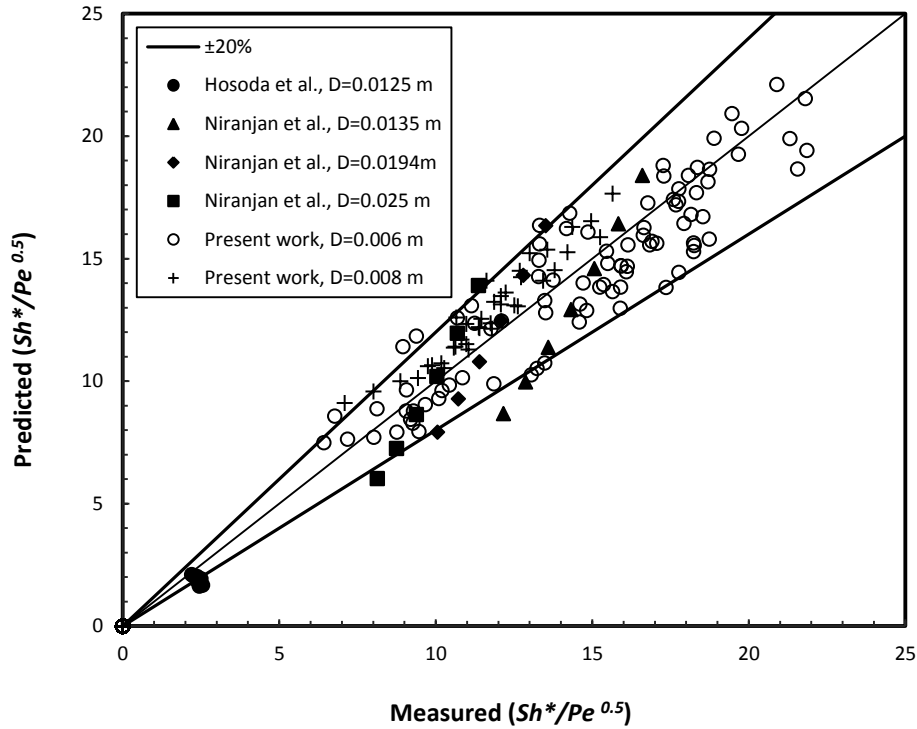
Fig. 4.15 Comparison between measured and predicted data by the new correlation Eq. 4.9.

4.6.3. Square channel

Fig. 4.16 shows the measured liquid-side mass transfer coefficient based on Eq. 4.7 for stationary Taylor bubbles. The data with the same symbol represents a single bubble over the dissolution period as a function of the instantaneous equivalent diameter and V_0 denotes the initial bubble volume. Because of the counter diffusion of dissolved air from the liquid phase into the bubbles, the CO_2 mole fraction inside the bubbles does not remain constant during the progress of the dissolution [28] and Eq. 4.7 is no longer applicable. Therefore only the data for roughly the first 10 seconds of the process are used for bubbles with different initial sizes. As it can be seen, the bubble size has a considerable influence on the measured liquid-side mass transfer coefficient of Taylor bubbles. For dissolving gas bubbles, it is known that the mass transfer coefficient depends upon the interface mobility of bubbles [118], [23] and it is proven that interface mobility relies on one hand on the bubble size and on the other hand on the presence of surface active contaminates in the liquid phase [23],[68]. As the liquid used in our experiments was deionized water, therefore the presence of surface active contaminates can be excluded. As a result, these findings which show that the liquid-side mass transfer coefficient

increases as bubble size decreases, are consistent with the fact that interface mobility of bubbles increases as the bubble size decreases [119].
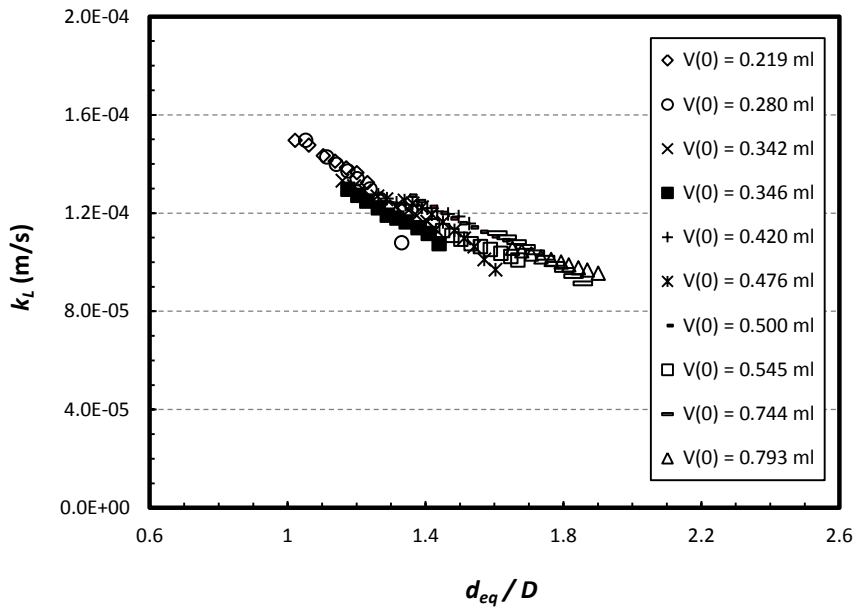
Fig. 4.16 Liquid-side mass transfer coefficients k_L for stagnant single bubbles in square channel.

Fig. 4.17 shows the prediction of classical penetration theory [120] for our data. This theory, which was firstly proposed by Higbie [119], is widely used for gas-liquid interfaces. In this theory, which assumes that when the time of exposure of a fluid to mass transfer is short, the transferring species would not penetrate very far into the liquid and as a result, the mass transfer coefficient is proportional to the inverse root of contact time of gas and liquid phase [120] according to

$$k_L = 2\sqrt{\frac{D_c}{\pi\, t_c}}\,,$$

Eq. 4.10

where t_c is contact (exposure) time between gas and liquid. In other systems such as bubble columns, this parameter is defined as the ratio of bubble diameter to the relative velocity of bubble and liquid, u_r. However, for our setup, since we have elongated Taylor bubble in our system, t_c is defined as the ratio of the bubble length to the relative velocity of bubble and liquid [121]

$$t_c = \frac{L}{u_r}\,.$$

Eq. 4.11

Bubble relative velocity, u_r is calculated by measuring the liquid flow rate, Q_L and available cross sectional area for the liquid between the bubble and the channel wall, A_L:

$$u_r = \frac{Q_L}{A_L}.$$
<div align="right">Eq. 4.12</div>

A_L was calculated by measuring the difference between the channel cross sectional area (which is constant and known) and the average cross sectional area of each bubble which was calculated from the processed X-ray images.

As it can be seen, the increase of mass transfer coefficient is in accordance with the penetration theory and good agreement exists between the experimental data and this theory.
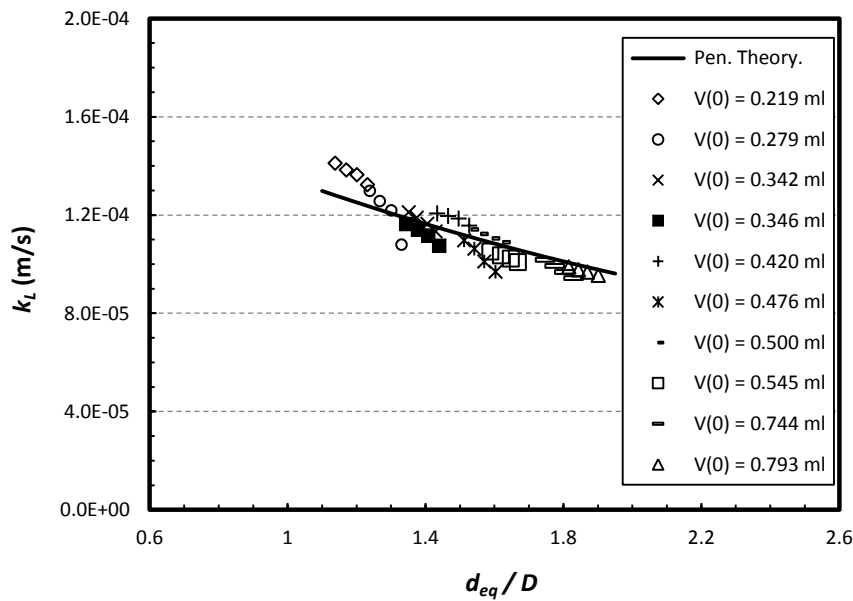
Fig. 4.17 The comparison between experimental data and penetration theory.

Fig. 4.18 shows the comparison of the liquid-side mass transfer coefficients k_L of stagnant single Taylor bubbles with different initial volumes in square and circular channels. As it is shown, the k_L values are similar for both channels. However, there are some distinguishable differences between the trend of the k_L values in the two curves. For the square channel as it was shown before, k_L increases with decrease of bubble sizes, while no obvious trend could be found for the circular channel. A reason may be that the hydrodynamics and flow pattern of liquid within these two channels are very different. In the square channels, the flow is not axisymmetric [5] and for the capillary number ranges used in our experiments ($Ca \sim 2.96 \times 10^{-4}$), Thulasidas et al. [34] showed that liquid film thickness is function of the bubble velocity and, for fluids of low viscosity, it is typically lower than 50 μm. As a result, almost all of the liquid passes through the corners and only a few percent of the liquid passes

along the walls [33]. In contrast, in circular channels, there is a symmetric liquid flow field around the bubble and the liquid film thickness is thicker than in a square channel and the liquid uniformly flows around the bubbles [1]. Nonetheless, we still consider this as an open point, which deserves future experimental consideration.

On the other hand, this result is consistent with our observation for mass transfer in square and circular channels. In Section 4.4.1 it was shown that despite the free rise velocity of bubbles in square channels is three times higher than in circular channels, the liquid-side mass transfer in both the circular and square channel has almost the same values, which means that the high liquid film thickness in the corners of square channels does not play a significant role in the mass transfer of Taylor bubbles.
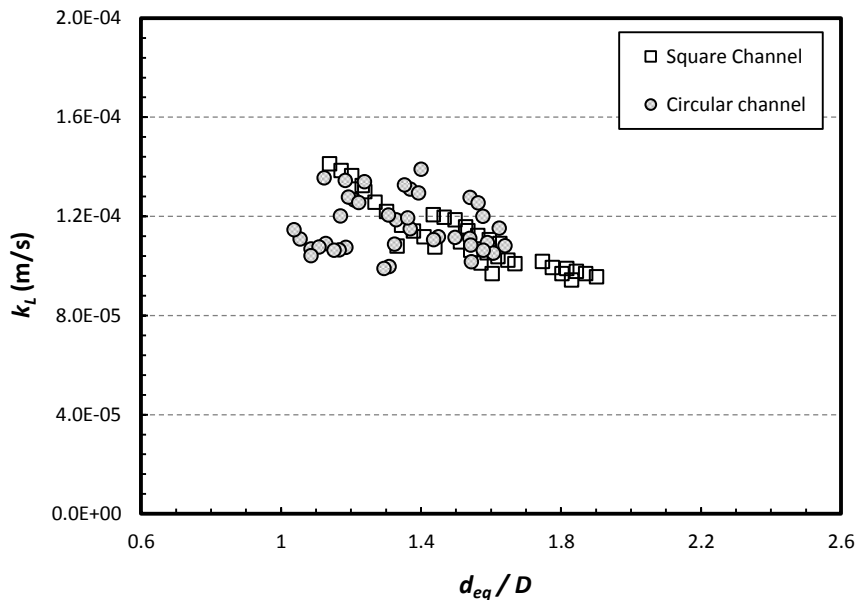
Fig. 4.18 Comparison between mass transfer coefficient k_L in circular and square channels as a function of bubble size ratio.

4.7. Oxygen transfer

For comparison and evaluation of the proposed correlation, the absorption of oxygen in deionized water was investigated. The experimental setup and conditions are the same as before. Fig. 4.19 shows the dissolution of long O_2 bubbles with different initial size. Despite of high solubility of oxygen in water, the dissolution rate of this component in water is orders of magnitude slower than for CO_2. Therefore it is necessary to consider counter diffusion of dissolved nitrogen N_2 in the water.
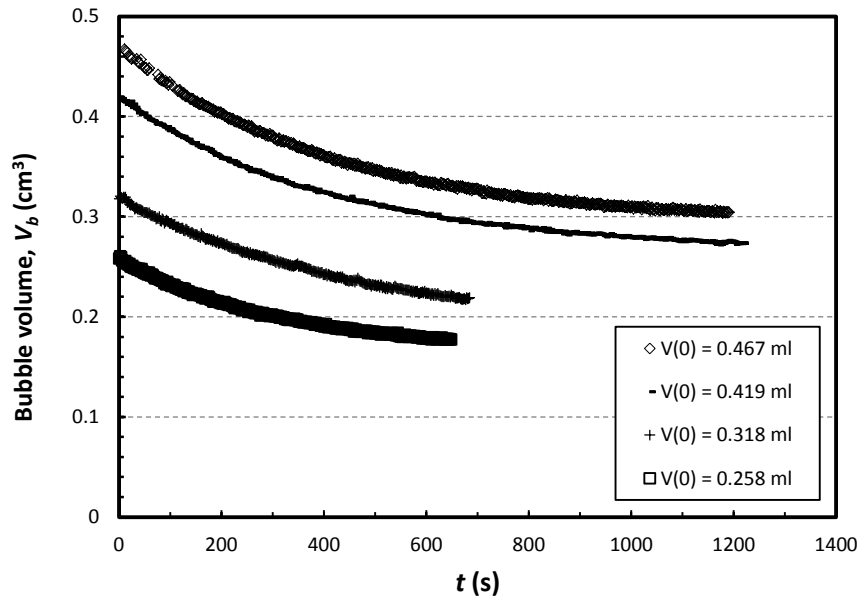
Fig. 4.19 The long term dissolution of O_2 bubbles with different initial size.

For a situation where there is some dissolved gas in the liquid that can undergo counter diffusion, a mass balance equation like Eq. 4.3 should be considered for each component [23]. For the present system, in which there is dissolved N_2 and O_2 in the liquid phase, Eq. 4.3 would be solved for each component (O_2, N_2) according to

$$-\frac{dn_i}{dt} = k_{Li}A(C_i^* - C_i),$$
Eq. 4.13

where C_i^* and C_i are the concentration of component i at the interface and in the bulk of liquid and k_{Li} is the liquid-side mass transfer coefficient calculated by Eq. 4.9. C_i is calculated by assuming equilibrium with the atmosphere and C_i^* is calculated [28] as

$$C_i^* = \frac{C_L P_i}{H_i - P_i},$$
Eq. 4.14

where P_i is partial pressure of component i in the bubble

$$P_i = \frac{P n_i}{\sum_i^2 n_i}.$$
Eq. 4.15

Finally the instantaneous equivalent diameter of bubbles may be calculated by means of ideal gas law

$$d_{eq} = \left[\frac{6RT\sum_i^2 n_i}{\pi P}\right]^{1/3}.$$
Eq. 4.16

In Fig. 4.20 the predictions of the new correlation are compared with the measured values. The predictions are in agreement with experimental data, when the counter diffusion of N_2 is considered.

From these results we can conclude that the presented correlation (Eq. 4.9) is valid not only for CO_2 dissolution but also for low soluble gases in water.
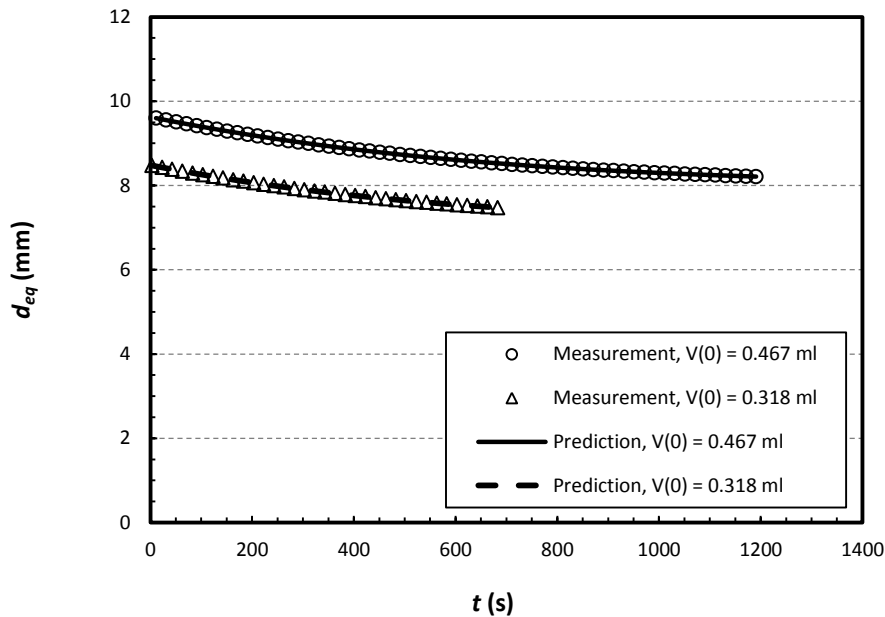
Fig. 4.20 Comparison between the predictions of the new correlation and the measured values.

4.8. Summary

The absorption rate of single Taylor bubbles of carbon dioxide in water were investigated in vertical milli-channels using high-resolution X-ray imaging. The liquid-side mass transfer coefficient was calculated by measuring the changes in the size of the bubbles at constant pressure. The experiments covered a large range of initial Taylor bubble length varying from 5 mm to 22 mm. The utilization of high-resolution microfocus X-ray visualization enabled the acquisition of a series of high-resolution radiographic images of nearly stationary Taylor bubbles. The processed images gave the volume, interfacial area and length of the bubble with high accuracy as a function of time and were used to evaluate the liquid-side mass transfer coefficient between bubble and liquid using the mass conservation equation.

In case of circular channels, the results show that Sherwood numbers have a large dependency on the bubble length and also equivalent diameter which is in accordance with previous results for larger pipe sizes. However the values of measured Sherwood numbers could not be predicted by available correlations which are valid only for larger pipes. As a result, a new mass transfer correlation in the

form of a modified Sherwood number and as a function of Peclet number as well as ratio of bubble equivalent diameter to capillary diameter (d_{eq}/D) was presented. The proposed correlation is applicable for a large range of d_{eq}/D ratio from 0.8 to 1.6 ($0.75 < L/D < 3.6$) with high accuracy.

The comparison of the results for the square and circular channels showed that despite the fact that the rise velocity of bubbles in the square channel is about three times higher than in the circular channel, the liquid-side mass transfer coefficient is about the same. Furthermore, the results show that in square channels the dissolution curves are relatively even, while the dissolution curves for circular channels exhibit some distinguishable change in the slope. In addition, it was shown that the calculated liquid-side mass transfer coefficient based on the measured data is in good agreement with the data predicted by the penetration theory.

5. Film thickness around Taylor bubbles in mini-channels

5.1. Introduction

In this chapter the experimental results of measurement of liquid film thickness around the Taylor bubbles in millimeter-size channels of circular and square cross section are reported and the results are compared with experimental and numerical data available in the literature.

5.1.1. Importance of the film thickness

In Taylor flow, an aqueous wetting layer covers elongated bubbles and prevents the direct contact of gas/vapor bubbles and channel wall. The main difference between the liquid film in Taylor flow and the one in annular flow is the wavy shape of the film in annular flow. Several investigations have proven the significant role of the liquid film in heat, mass and momentum transfer in milli- and microchannels.

In case of heat transfer application of microchannels, the liquid film thickness is an important parameter. For example the evaporation heat transfer coefficient, h_{eva}, through the film thickness is calculated as

$$h_{eva} = \frac{K}{\delta},$$
<div align="right">Eq. 5.1</div>

where K is thermal conductivity of liquid phase [122]. This equation demonstrates role of the liquid film thickness for predicting the flow boiling heat transfer coefficient in microchannels [123].

In case of mass transfer applications, for example in three phase catalytic reactions where mass transfer to the wall is of influence on the reaction rate, the liquid film thickness plays a key role for the mass transfer rate [114]. In biological applications, the liquid film separate samples from the channel and keeps the samples away from asperities within the channels and prohibits the contamination between the samples [124].

In case of Taylor bubble reactors, the creation of a liquid film around the bubbles influences the gas hold-up. As it is known, the gas hold-up is one of the main parameters in the reactor design. This parameter affects the residence time of reactant in the reactor. The liquid film inside the channel causes the reduction of channel cross section for passing of the gas phase. As a result the gas phase velocity increases in comparison with the gas superficial velocity in the reactor. Consequently, the real gas hold-up is different from initial flow rate definition in the feed flows [114].

As it was briefly mentioned, the knowledge about the liquid film thickness in milli- and microchannels is important for a quantitative investigation of tube flow heat transfer, mass transfer coefficient, reactor design and its corresponding influence on the bubble and carrier flow dynamics [35],[125].

5.2.   Studies on 2 mm channels

For 2 mm channels, to achieve a high spatial resolution, X-ray synchrotron radiography and X-ray synchrotron tomography were applied. The experiments were performed in the TOPO/TOMO beamline at the ANKA synchrotron X-ray facility of Karlsruhe Institute of Technology which allows high quality and high speed X-ray imaging. The beamline is operated in white-beam mode and is located on a bending magnet (1.5 T, bending radius 5.6 m).

The liquid comes from a reservoir and was pumped through the channel. The pump was selected in a way that produces a minimum oscillation and fluctuation on the liquid and channel. The bubbles were produced and injected with the same technique as described in section 3.2.1. The rate and intervals of bubble injection was selected small enough to reduce the impact of acceleration of liquid during the bubble injection. Therefore, a new Taylor bubble was released after the previous bubble left the

channel. Both square and circular channel cross sections were tested to investigate the liquid film thickness in lateral and diagonal direction.

The scintillation screen based X-ray image detector received a 1.78 mm by 2.31 mm portion of the capillary. The connected camera can process up to 36,000 radiographic images per second. The effective spatial resolution was 3.7 µm. The projection images in the circular channels are not dependent on the angular orientation. For these channels the bubble shape was determined from the projection images, as the bubble shape has cylinder symmetry. For square channel, however, we applied tomography [126]. By exploring the distribution of brightness over the channel axis, the front and rear positions of bubble tip were extracted. The bubble free rise velocity was measured by tracing the position of the bubble. Using this data and by super-imposing of the sequential single images, a fairly noise free image of the whole individual Taylor bubble was produced.

5.2.1. Experimental setup and procedure

The liquid was pumped through a vertically aligned test section (the capillary channel) by means of a pump which produced only little oscillation induced pressure fluctuations in the liquid. Via a T-junction at the bottom of the capillary channel gas was injected into the flowing liquid using a high-speed injection valve. Using an optical visualization approach it was proven that Taylor bubbles could be generated at sufficient reproducibility. Different Taylor bubble regimes can be realized by changing the duty cycle parameters of the gas injection valve. For $D = 2$ mm the effect of buoyancy is negligible and only surface tension and viscosity forces act on the bubbles in this capillary regime. The bubble size ratio, was chosen to be $d_{eq}/D > 1.5$ to ensure fully developed Taylor bubbles, resulting in bubble lengths roughly more than $3D$. To cover a wide range of Ca and Re numbers, experiments were done using an aqueous solution of clean water and Glycerol with a viscosity of µ = 33.5 mPas at 25°C. The liquid temperature was continuously monitored at the lower and upper end of the capillary channel and the dependency of the liquid viscosity on temperature was considered during the analysis afterwards. The bubble velocity was varied between $U_b = 20$-350 mm/s resulting in Capillary numbers $Ca = 0.01$-0.13.

5.2.2. Results

The measured data of film thickness in circular and square channel are presented in Fig. 5.1. The graphs show the liquid film thickness around the Taylor bubbles at 30 mm below the bubble tip in the form of dimensionless bubble radius, R, which defines for the diagonal direction:

$$R_{dai} = \sqrt{2} - \frac{2\delta}{D} , \qquad\qquad \text{Eq. 2.30}$$

and for the lateral direction:

$$R_{lat} = 1 - \frac{2\delta}{D} . \qquad\qquad \text{Eq. 2.31}$$

For square channels in diagonal direction, the prediction of correlations developed by Kreutzer et al. [1] and Han and Shikazono [112] are also presented in Fig. 5.1a. As it can be seen, there is a good agreement between the measured data for the 2 mm channel and the predicted values of both correlations. However, in lateral direction, the number of investigations for film thickness measurement is rare. For comparison, the experimental data of Kolb and Cerro [32] and Hazel and Heil [37] are presented. As it can be seen, the experimental data reported by Hazel and Heil shows a better consistency with our experimental data in the 2 mm square channel.

Fig. 5.1c shows the measured film thickness in the circular channel. The data are compared with the data from Irandoust and Andersson [105], Han and Shikazono [109] and Aussillous and Quéré [106]. Both the measured and predicted data show that the capillary number increases for decreasing the bubble size ratio. The increase of capillary number comes either from increase of bubble velocity or increase of liquid viscosity. The detailed physico-chemical specifications of liquid used in the experiments are given in Table 5-1 and Table 5-2.
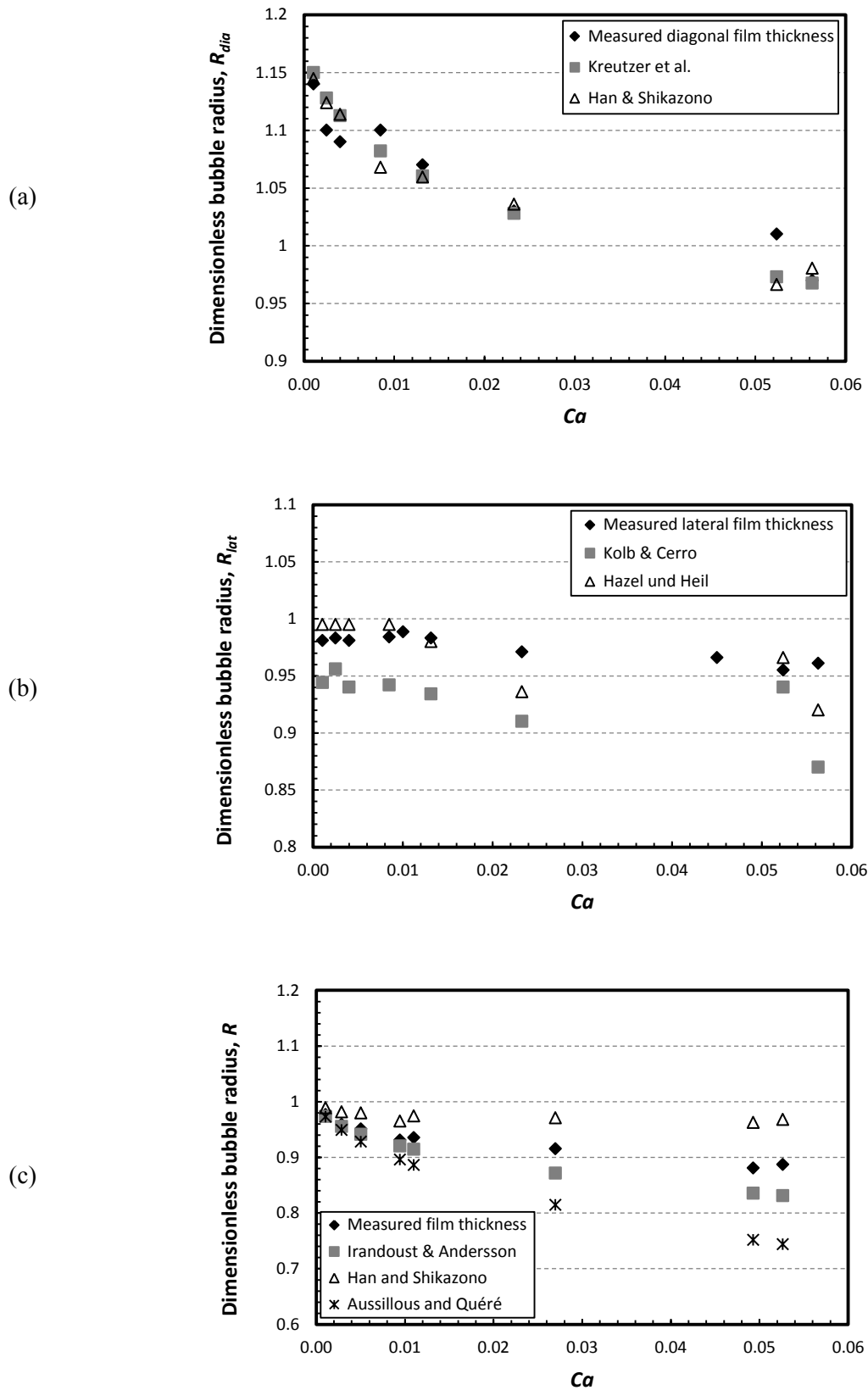
Fig. 5.1 Liquid film thickness in the 2 mm channel in the form of dimensionless bubble radius (Eq. 2.30, 2.31), a) square channel diagonal direction, b) square channel lateral direction and c) circular channel.

Table 5-1 Experimental and physical parameters of the experiments in the 2 mm square channel

Glycerol Conc.	Liq. flow rate (Q_L)	Bubble front tip vel. (U_b)	Bubble rear tip vel. (U_b)	Bubble ave. vel. (U_b)	Tempe rature (T)	Viscosity (μ)	Surface tension (σ)	Density (ρ)	Ca	Re	We
Vol. %	ml/min.	mm/s	mm/s	mm/s	°C	mPas	mN/m	kg/m³	-	-	-
0.25	8.13	36.50	36.40	36.45	21.60	2.00	70.50	1059.20	0.001	38.61	0.04
0.25	20.97	92.20	91.60	91.90	22.20	1.90	70.40	1059.00	0.002	102.44	0.25
0.25	72.17	315.00	313.00	314.00	22.40	1.90	70.40	1059.00	0.01	350.03	2.97
0.60	6.59	27.20	27.20	27.20	22.10	9.90	67.60	1152.60	0.00	6.33	0.03
0.60	20.68	90.00	89.30	89.65	21.90	9.90	67.60	1152.80	0.01	20.88	0.27
0.60	81.15	372.90	371.20	372.05	23.10	9.50	67.50	1152.10	0.05	90.24	4.73
0.80	7.07	32.70	32.30	32.50	24.10	46.70	65.30	1206.00	0.02	1.68	0.04
0.80	19.66	88.90	88.10	88.50	26.20	41.40	65.10	1204.70	0.06	5.15	0.29

Table 5-2 Experimental and physical parameters of the experiments in the 2 mm circular channel

Glycerol Conc.	Liq. flow rate (Q_L)	Bubble front tip vel. (U_b)	Bubble rear tip vel. (U_b)	Bubble ave. vel. (U_b)	Tempe rature (T)	Viscosity (μ)	Surface tension (σ)	Density (ρ)	Ca	Re	We
Vol. %	ml/min.	mm/s	mm/s	mm/s	°C	mPas	mN/m	kg/m³	-	-	-
0.25	5.78	35.50	36.40	35.95	20.40	2.10	70.60	1059.70	0.001	36.28	0.04
0.25	16.42	101.70	101.40	101.55	21.20	2.00	70.50	1059.40	0.003	107.58	0.31
0.25	53.75	334.00	330.80	332.40	21.90	2.00	70.40	1059.10	0.01	352.04	3.32
0.60	5.30	33.10	33.20	33.15	21.10	10.30	67.70	1153.20	0.01	7.42	0.04
0.60	12.19	75.30	74.90	75.10	21.90	9.90	67.60	1152.80	0.01	17.49	0.19
0.60	50.96	352.90	347.60	350.25	22.90	9.50	67.50	1152.20	0.05	84.96	4.19
0.80	5.78	36.70	36.60	36.65	23.60	48.10	65.30	1206.30	0.03	1.84	0.05
0.80	13.05	76.20	77.00	76.60	24.80	44.80	65.20	1205.60	0.05	4.12	0.22

5.3. Studies on 6 mm channels

5.3.1. Circular channel

The image acquisition procedure was the same as described in section 3.3. Fig. 5.2 a,b shows an exemplary result for the bubble shape and liquid film of stationary small and elongated Taylor bubbles in downward flow of deionized water in a 6 mm circular channel. As it can be seen, the liquid film thickness is not constant and changes along the bubble axis. However, for an elongated bubble, except for the front and rear tip of bubble, the film thickness is almost constant. Fig. 5.3 gives the thickness of liquid film at the middle of the Taylor bubbles for different bubble sizes (lengths). The film thickness increases as the bubble length decreases. This trend is consistent with the data of bubble free rise velocity. As it was shown in section 3.4, with the decrease of bubble length, the liquid film around the bubble increases and bubbles can travel more easily along the channel.

(a)

V_b = 0.3894 ml

(b)
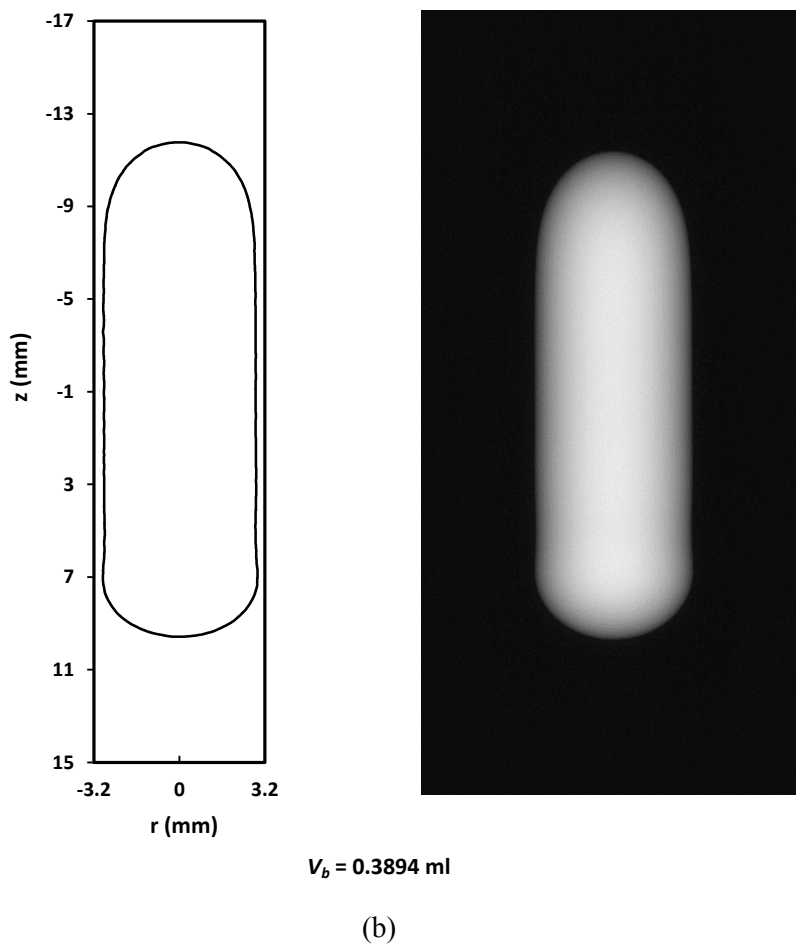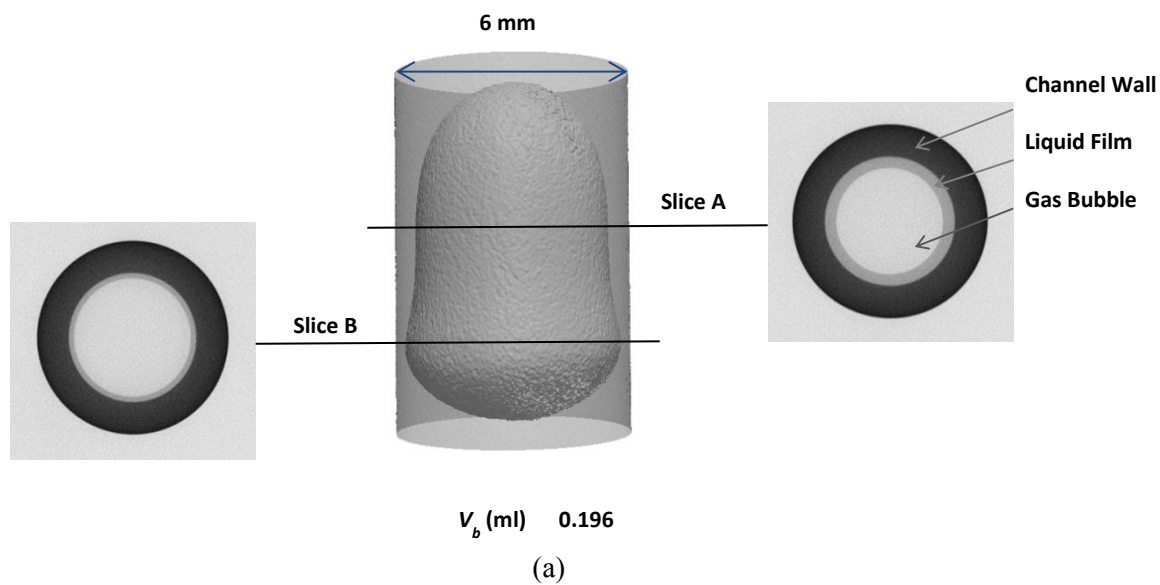
Fig. 5.2 The bubble shape and liquid film of stationary Taylor bubbles. A small (a), an elongated bubble (b)
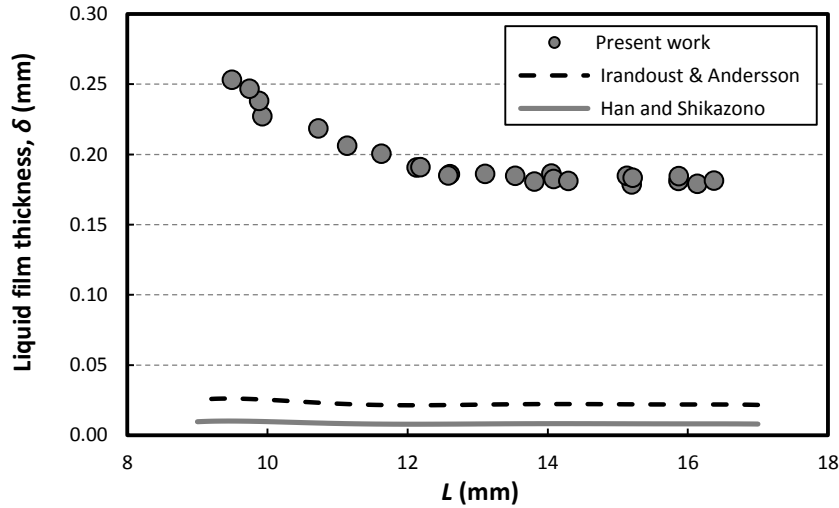
Fig. 5.3 Measured thickness of liquid film at the middle of Taylor bubbles for different bubble size.

Furthermore, the prediction of correlations from the literature is also presented. As it can be seen, the predictions are not consistent with our experimental data. The reason can be attributed to the channel size and its impact on the hydrodynamics of flow in small channels. The correlation developed by Han and Shikazono [109] are based on the data in submillimeter channels (microchannel) and the correlation of Irandust and Anderson [105] is based on the data of 1-2 mm channels, while our data presents the film thickness in 6 mm channels. This difference implies different hydrodynamics for Taylor flow. As it was discussed in section 3.4, for the air-water system the interfacial forces are dominant to the gravitational force and the bubble will not rise if the channel size is below 5 mm.

5.3.2. Square channel - diagonal direction

For 6 mm channels, the microfocus X-ray technique was used to measure the film thickness between the Taylor bubble and the solid channel wall. For the circular channel, the thickness of the liquid film is dependent only on the vertical position below the bubble front tip and is axis-symmetric. On the contrary, for the square channel, the liquid film thickness is not symmetric and two regions with various film thicknesses can be observed. One region is the corners of the channel with a thicker film with a maximal film thickness in the diagonal plane, i.e. viewpoint angle is 45° [7]. Another region is in lateral direction where the shape of the Taylor bubble is constricted by the planar channel walls (Fig. 5.4). In this region the liquid film thickness is too thin and could not be measured by the applied tomographic technique (spatial resolution 26.5 μm).

Channel Wall

Liquid Film

Gas Bubble
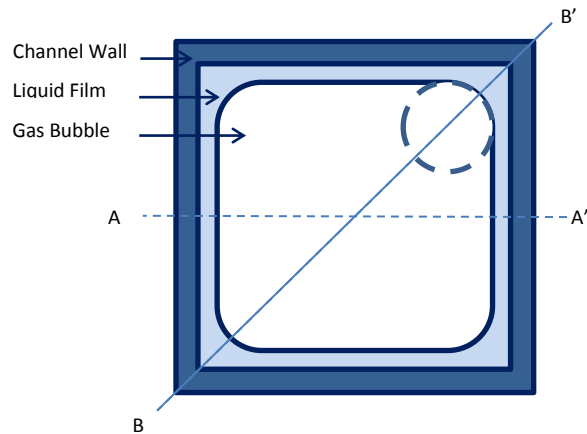
Fig. 5.4 The profile of liquid and Taylor bubble interface in square channel for low *Ca* values.

We name this region the thin film region with respect to the surface of the Taylor bubble. The thin film region was extracted from the three dimensional images by thresholding the distance between the detected Taylor bubble surface and the inner channel wall, as illustrated in Fig. 5.5.

Fig. 5.5 Location of the thin film area (dark regions) on a Taylor bubble surface in a square channel.

The liquid film thickness in the diagonal directions in the 6 mm square channel was measured at half of the bubble length. The results as a function of bubble size are presented in Fig. 5.6. As it can be seen, the liquid film in the corners of the square channel does not considerably change with the bubble size. As it was shown in section 3.4, a change of bubble size directly affects the free rise velocity of

80

bubble. These results show that the liquid film flowing in the corners of the square millimeter-size channel does not vary with change of bubble size from 8 mm to 25 mm. The prediction of correlations developed by Han and Shizakono [112] and Kreutzer et al. [1] are also presented. As it can be observed, in contrast to the circular channel, there is a good agreement between the predicted data and the experimental results. The reason can be attributed to the fact that the liquid film in the diagonal direction in the square channel is not considerably dependent on the flow regime. Experimental observation of Kolb and Cerro [32] and also analytical investigations of Ratulowski and Chang [127] revealed that for $Ca > 0.4$, the bubble diameter in both the lateral and diagonal directions is the same and axisymmetric. Kreutzer et al. [1] using the experimental data of Kolb and Cerro [32] and Hazel and Heil [37] showed that when the Ca value is lower than 0.4, the film thickness in diagonal direction of square channels is practically independent of Ca. The similar behavior of independency of diagonal film thickness on the flow conditions was found by Thulasidas et al. [33]. They observed that even in upward flow of Taylor bubbles with external pressure force, the liquid film in the corners of square channel flows downward. As a result it can be concluded that, despite the correlations developed by Han and Shizakono [112] has been developed for micro-sized channels and the governing forces are different in our millimeter-size channel, this correlation can still be applied with good accuracy to calculate the diagonal film thickness in small channels.
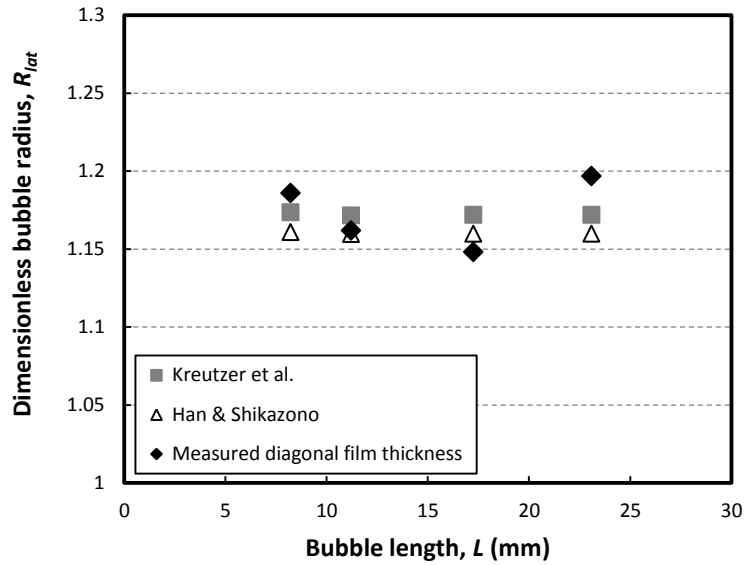
Fig. 5.6 The diagonal liquid film thickness at half of bubble length in the 6 mm square channel in the form of dimensionless bubble radius (Eq. 2.31).

5.3.3. Square channel - microfocus X-ray technique

Since the liquid film thickness in lateral direction in the square channel is too thin, the channel position was modified to reach the maximum spatial resolution (Fig. 5.7). The glass channel was placed near the X-ray tube. The clearance d_{cc} was roughly 1 mm to achieve maximum magnification. One of the four inner plane surfaces was aligned with the central ray as shown in Fig. 5.7. Alignment was achieved by subsequent rotation of the capillary (small increments), recording of X-ray images with long exposure time and evaluation of the resulting X-ray images (searching for sharpest edge visualization). The angular increment was 36000 steps per 360° which means 0.01° per step.
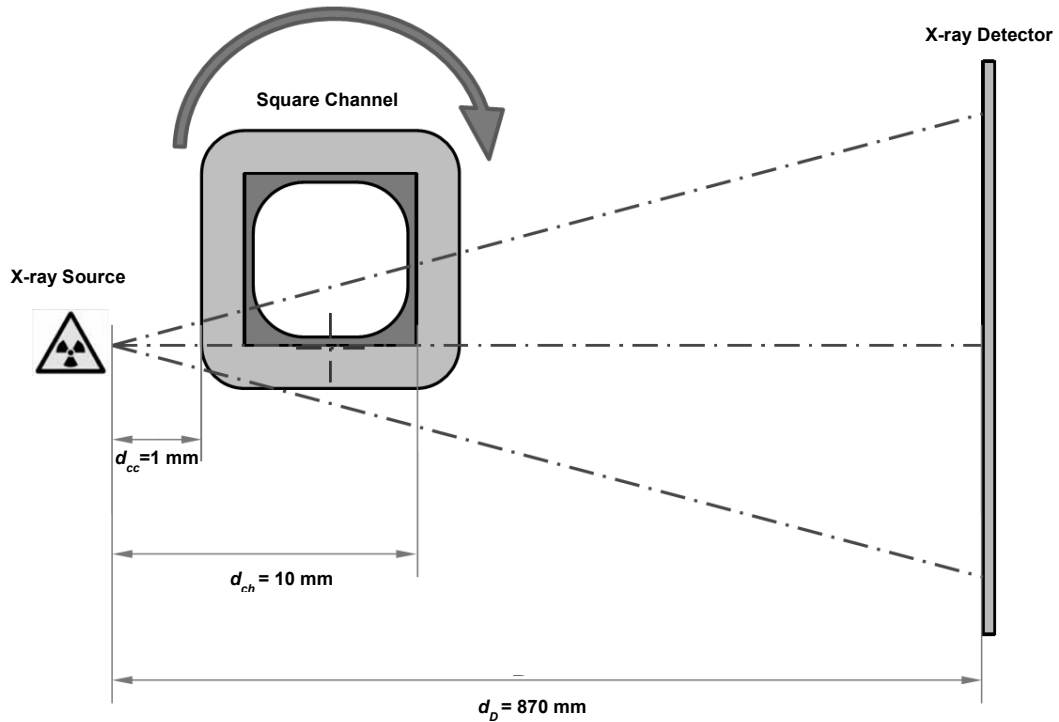
Fig. 5.7 The positioning of square channel in front of X-ray source for liquid film measurement.

For each recorded X-ray image the projected edge and its image inclination angle α was detected. The images were vertically averaged to extract the edge attenuation profile (Fig. 5.8). The sharpest edge was found for angular step #16 (Fig. 5.9).
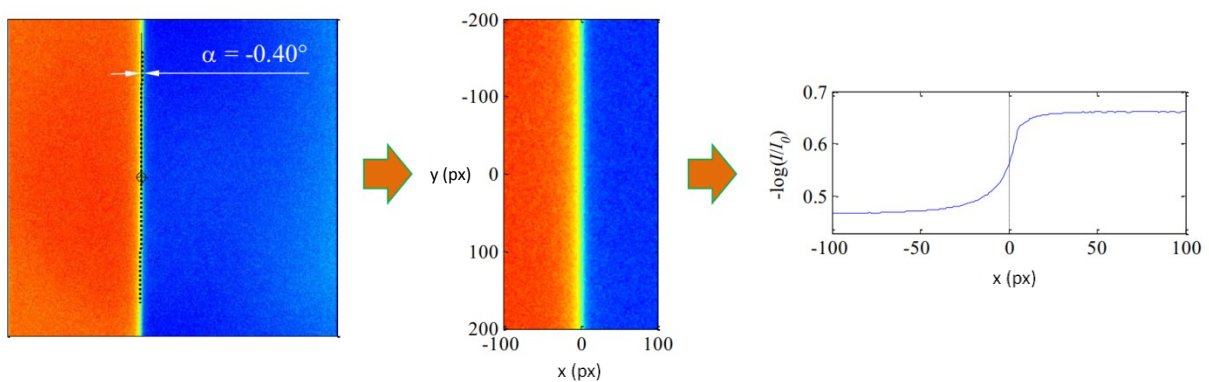
Fig. 5.8 Extraction of edge position and inclination and average edge attenuation profile.
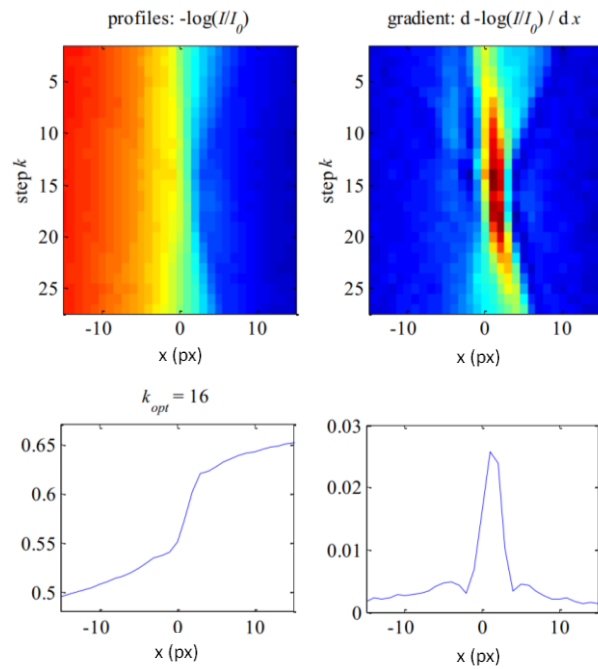
Fig. 5.9 Scanned edge attenuation profiles and profile gradients.

Liquid film thickness measurement

A Taylor bubble was fed into the channel and was guided through the X-ray imaging window at varying speeds by modification of the liquid flow rates. The channel was rotated to the angular position with the sharpest detected edge profile. A vertically averaged attenuation profile was computed for each X-ray image, the attenuation profiles subsequently were scanned to identify the frame numbers for images with presence of the Taylor bubble and of Taylor bubble free reference images (Fig. 5.10).

A reference image was computed by averaging all reference images. The image inclination of the projected edge was measured. Images were rotated accordingly in all subsequent calculations. The difference image between each short time exposure and the reference image was calculated. In case of Taylor bubble presence the projected edge of the bubble was detected (Fig. 5.11). Vertically averaged attenuation profiles were calculated for the reference image as well for the difference image. The horizontal gradient of the difference image attenuation profile (corresponding to the edge of the bubble) was compared to the horizontal gradient of the reference image attenuation profile, corresponding to the location of the plane inner surface of the channel, to measure the gap width between projected bubble edge and projected inner plane surface at pixel size precision (Fig. 5.12).
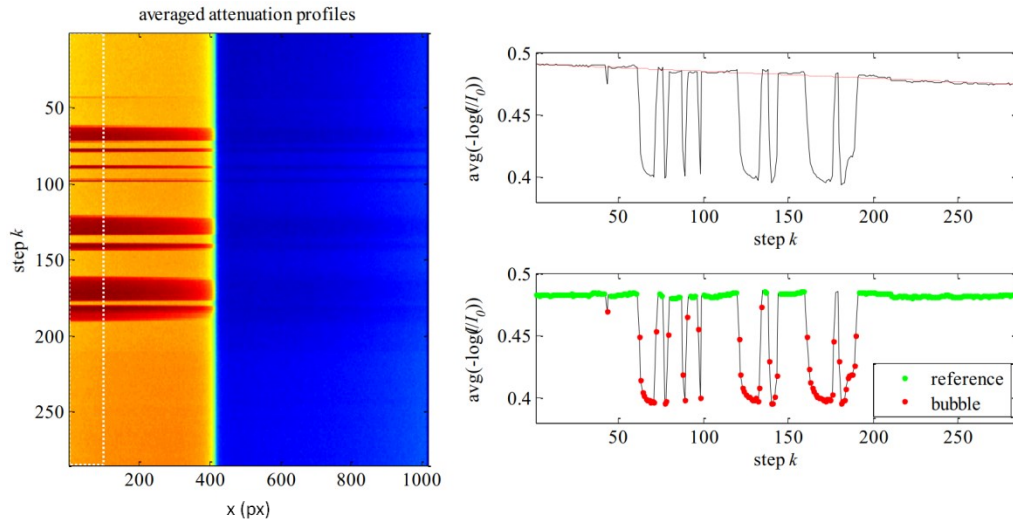
Fig. 5.10 Averaged attenuation profiles and identification of frame numbers of a detected Taylor bubble.
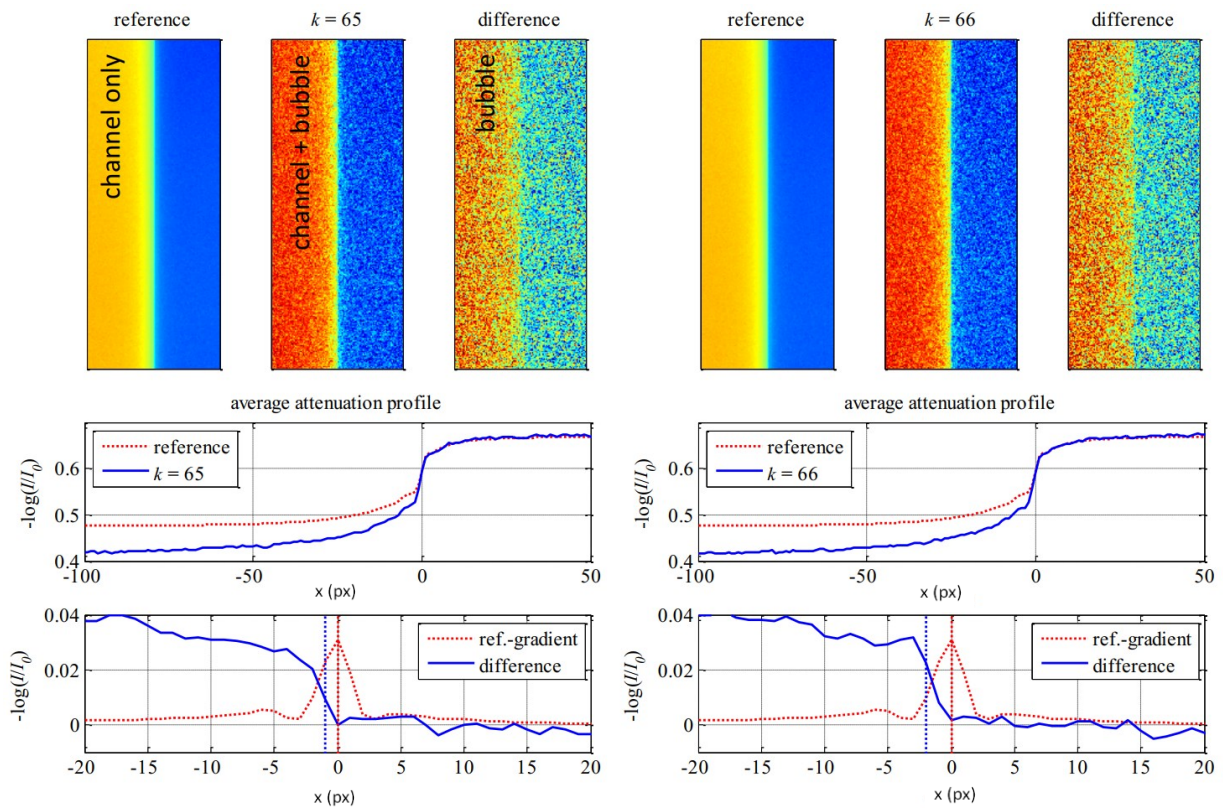
Fig. 5.11 Attenuation profile with and without bubble for two subsequent time steps.
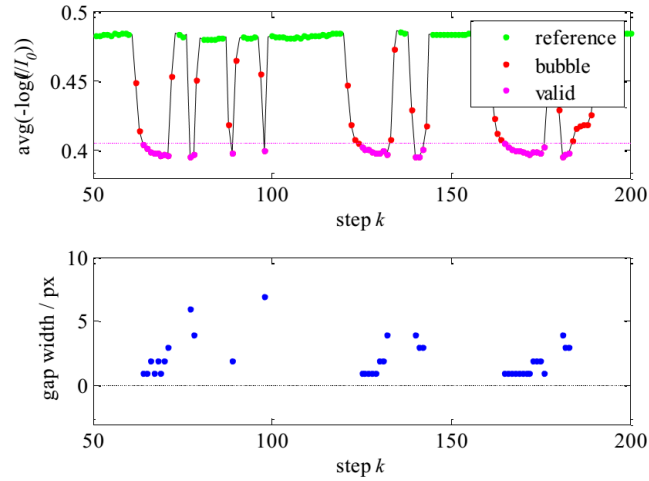
Fig. 5.12 Detected gap width between bubble edge and projected inner plane surface.

Geometric interpretation

A gap width of approximatively 1 to 2 px was measured for most of the captured frames of the moving Taylor bubble (Fig. 5.12). The measured gap width corresponds to the liquid film thickness at the position indicated by the arrows in Fig. 5.13, which is approximatively ¼D (channel hydraulic diameter) away from the center of the inner surface, thus $d' = d_{ch} - ¼D = 10$ mm – 1.5 mm = 8.5 mm. Since, the channel was misaligned by $(16 – 12) \times 0.01° = 0.04°$. According to Fig. 5.13, this results in an overestimation of liquid film thickness of approximatively $¼ D \times \tan (0.04°) = 1$ μm. The pixel size on the detector is 200 μm, thus the effective pixel size at position d' is $l_{px} \times d'/D = 2$ μm. Thus, the detected liquid film thickness is approximatively $(1$ to $2)$ px $\times 2$ μm - 1 μm = $(1$ to $3)$ μm.
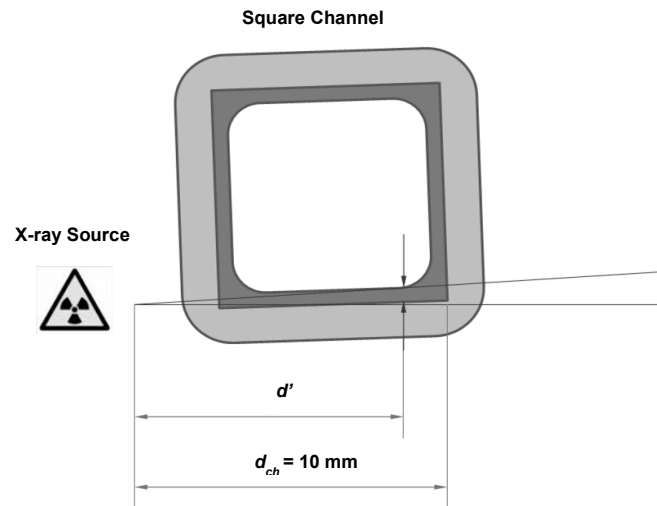
Square Channel

Fig. 5.13 Geometric interpretation of measured gap width.

5.3.4. Square channel - LCDM technique

Principles of LCDM

Since the liquid film thickness in 6 mm square channel (in lateral direction) is too thin, a laser confocal displacement meter (LCDM) with higher spatial resolution, was applied for detection and measurement of the liquid film thickness in square channels. This device which was actually designed for detection of scratches on ICs and other electronic equipment [128], was applied recently for measurement of liquid film thickness in micro-sized channels [129]. It is reported that, using this sensor, the liquid film can be measured with 1% error [123]. The principle of the LCDM is illustrated schematically in Fig. 5.14.

A laser beam is focused on the surface of the target through the objective lens. The objective lens moves up and down at high speed by means of a diapason. The reflected beam from the surface of the target enters a light detector through a pinhole. At the moment of receiving light, the sensor measures the exact position of the objective lens and finally calculates the distance to the target with high accuracy. This technique is not influenced by the material, color, or angle of the target.

The measurement range of LCDM is ±1 mm and spatial resolution is 0.1 μm. The light source is a red semiconductor laser with a wavelength of 655 nm. The laser spot diameter on the target is 7 μm and the distance of the target can be up to 30 mm. The sampling cycle is 640 μs to 187 ms depending on the frequency of the diapason. The main specifications of the LCDM are given in Table 5-3. The

measured values of film thickness were converted to DC voltage in the range ±10 V and the signals were acquired by a computer and saved with Labview software.
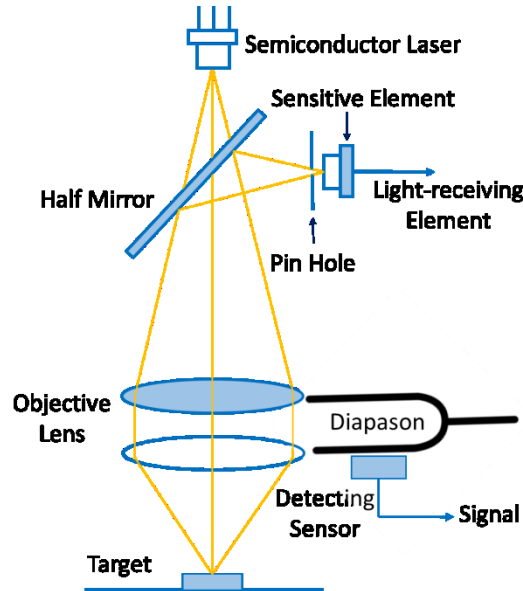
Fig. 5.14 Functional principle of the laser confocal displacement meter (LCDM).

Table 5-3 Laser confocal displacement meter specifications (Keyence Co.)

LCDM Model		**LT - 9030M**
Measurement range		± 1.0 mm
Reference distance		30 mm
Light source	Wave length	655
	Output	170 µW
	Class	Class I
	Spot diameter	7 µm
Scan with / interval		0 to 560 µm / 1 to 8 µm
Resolution		0.1 µm
Sampling cycle		640 µs to 187 ms
Temperature characteristic (20-30 ºC)		± 0.25 % F.S.

Calibration for refractive index difference

The channel surface is not round. As a result, there was no laser beam scattering since the curvature of channel in different direction is the same. However, because the refractive indices of glass wall and the liquid film are different, the focus is scattered. Therefore, this effect should be considered. Fig. 5.15 shows the pathway of the laser light and its reflection through air, channel wall and liquid

film. In this figure, x_1 is the thickness of channel wall and is measured separately by the LCDM when the channel is dry. x_2 is summation of the channel wall thickness and liquid film measured by the LCDM. Therefore, based on the system geometry, we have [112]

$$\frac{x_1}{x_2} = \frac{y_1}{y_2} \qquad\qquad \text{Eq. 5.2}$$

$$tan\alpha_{air} = \frac{y_1}{x_1} \qquad\qquad \text{Eq. 5.3}$$

$$tan\alpha_L = \frac{y_2 - y_1}{\delta} \qquad\qquad \text{Eq. 5.4}$$

$$\delta = \frac{y_2 - y_1}{tan\alpha_L} = \frac{(x_2/x_1 - 1)y_1}{tan\alpha_L} = \frac{(x_2 - x_1)tan\alpha_{air}}{tan\alpha_L} \qquad\qquad \text{Eq. 5.5}$$

where δ is the liquid film thickness, δ_w the channel wall thickness, α_{air} the angle of incidence at the surface for air and α_L the angle of incidence at the surface for liquid film. Using Snell's law, we have

$$n_L sin\,\alpha_L = n_w sin\,\alpha_w, \qquad\qquad \text{Eq. 5.6}$$

$$n_w sin\,\alpha_w = n_{air} sin\,\alpha_{air}, \qquad\qquad \text{Eq. 5.7}$$

where n_L, n_w and n_{air} are liquid, channel wall and air refractive indices. α_{air} is the angle of incidence of the laser beam, which is 23°.
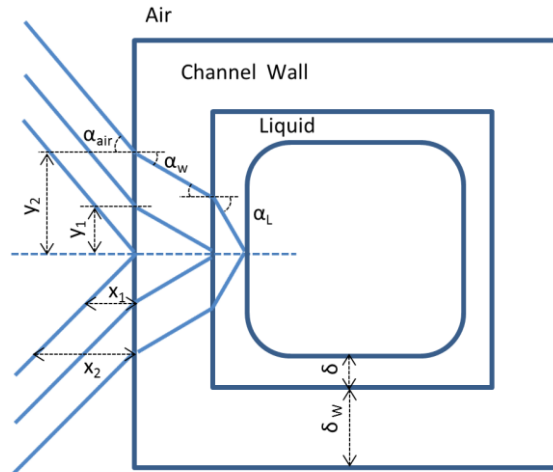
Fig. 5.15 Pathway of laser source and its reflection at air, channel wall and liquid film.

Results

The liquid film thickness was measured at different positions along the bubble length. The bubble size was selected between 25 mm < L < 50 mm to become sure that the Taylor bubbles are well developed. To increase the measurement accuracy of the LCDM system, the output data from the LCDM was averaged for every two measurements. As a result the time resolution is 0.7 kHz.

The measured film thickness data are given in Fig. 5.16. The data are an average of at least five measurements. The error bars indicate the standard error about the mean points. As it can be seen, both film thickness values for 32 mm and 41 mm bubble lengths are in the range of 1-5 μm, which is consistent with the results of measurements using the microfocus X-ray technique.

As it was mentioned before, to the best knowledge of the author, there is no experimental and numerical data for liquid film thickness in lateral direction for Ca values below 0.01 except the correlation developed by Han and Shizakono [112] (Eq. 2.29). However, in contrast their observation that "δ_{lat} still has a finite value", this correlation predicts the film thickness to be zero at low Ca values.

To summarize, the measured liquid film thickness for low Ca values in millimeter-size channels can provide a fairly good estimate of liquid film particularly in lateral direction for numerical simulation of heat, mass and momentum transport studies.
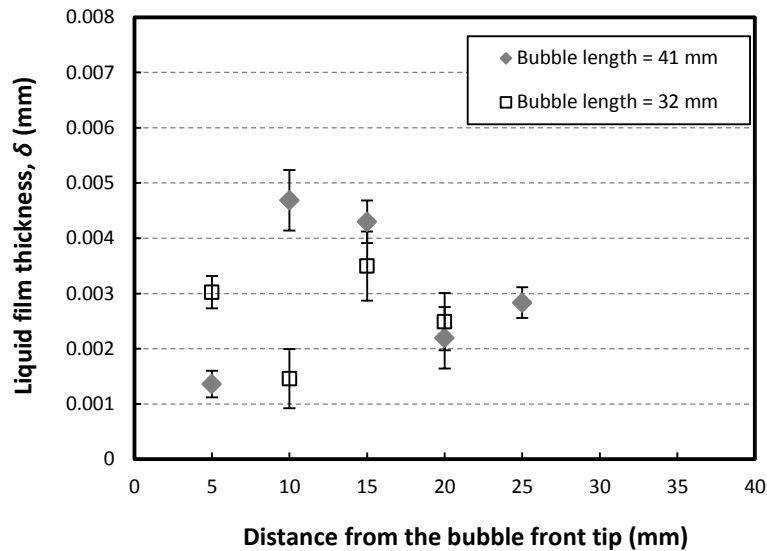
Fig. 5.16 liquid film thickness in lateral direction of elongated Taylor bubbles measured with LCDM.

5.4. Summary

In this chapter the liquid film thickness as a governing parameter in mass and heat transport in small channels was measured experimentally. The liquid film was obtained by two different techniques for circular and square channels with different hydraulic diameter. The results were compared with experimental and numerical data available in the literature. In case of channels with 2 mm hydraulic diameter, the available experimental and theoretical correlations mainly developed by Han and Shikazono [112] and Hazel and Heil [37] show an acceptable accuracy in the prediction of liquid film thickness.

Regarding the 6 mm channels with circular cross section it was demonstrated that the prediction of available correlations in the literature are not consistent with our experimental data and the reason was attributed to the channel size and its impact on the hydrodynamics of flow in small channels. For channels with square cross section, the experimental data could be fairly well predicted by available correlations. However, in the lateral direction, there is no experimental or theoretical data in the literature and the presented data can be considered as one of the first measured data for film thickness in lateral direction in square cross sectional milli-channels.

6. Effect of the presence of surfactants

6.1.   Introduction

It is known, that surface active agents (surfactant) influence both the hydrodynamics and the mass transfer rate in gas-liquid systems. They are adsorbed at gas–liquid interfaces and decrease the surface tension. Fig. 6.1 shows the presence of surfactant around the bubble in Taylor flow. In this chapter, the effect of surfactant on the shape, dissolution rate and liquid film thickness of an individual elongated Taylor bubble of CO_2 in water was investigated in channels of 6 mm inner diameter using the microfocus X-ray radiography technique.

6.2.   Experimental

The apparatus, procedure and calibration are the same as described in section 3.2. The water used for preparation of aqueous solutions comes from an ion exchanger and was purified via a millipore water purification system with output water having TOC (total organic carbon) 4 ppb and pH 7.0. The nonionic compound Triton X-100 ($C_8H_{17}C_6H_4(OCH_2CH_2)_{10}OH$) was used as surface active agent to contaminate the millipore water. It is a commonly used detergent in laboratories and cleaning agents. Surfactant concentrations C_s were set to 0.4, 2.0 and 20.0 mmol/m^3 (0.26, 1.30 and 13.0 ppm, respectively), which is much lower than the critical micelle concentration (240 mmol/m^3) [49].
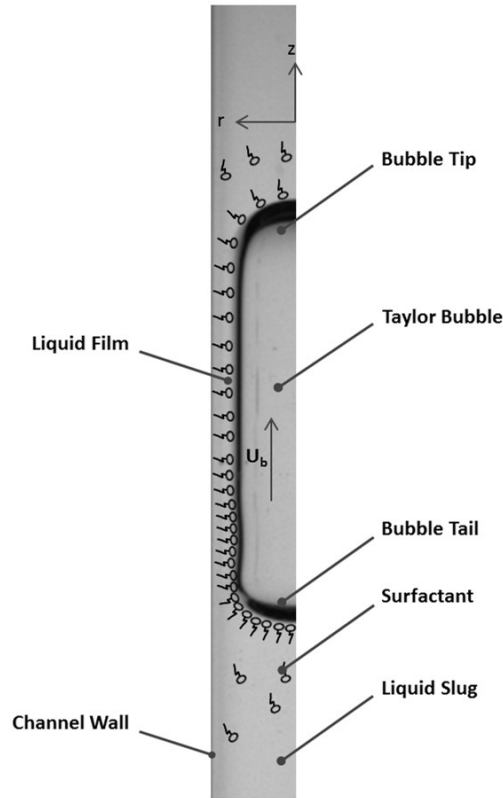
Fig. 6.1 Presence of surfactant around the bubble in Taylor flow.

The change of the viscosity is negligible. The concentration of surfactant was selected based on the most common ranges used by other investigators in the literature [79], [29], [76], [73], [49]. To compare the effect of concentration, lower and higher concentrations were applied. In our experimental setup, the maximum surfactant concentration which could be applied was about 13.0 ppm (20 mmol/m^3). Due to type of gas injection system, applying higher concentration of Triton X-100 caused foaming which considerably reduced the accuracy of measurements. The physicochemical properties of the surfactant [49] in the form of Langmuir number, La and surface coverage ratio, Se are as follows:

$$La = \frac{C_s \beta}{\alpha} \qquad \text{Eq. 6.1}$$

$$S_e = \frac{La}{La+1}. \qquad \text{Eq. 6.2}$$

The surface coverage ratio is defined as the ratio of interfacial surfactant concentration at equilibrium to the saturated interfacial surfactant concentration. These parameters are calculated based on the Langmuir isotherm [29]. α and β are desorption and adsorption rate constants and their values are 0.033 s^{-1} and 50 m^{3}mol^{-1}s^{-1}, respectively [49]. Se, La, and surface tension, σ, are given in Table 6-1.

Table 6-1 Physicochemical properties of liquid phase

Triton X-100	0.26 ppm	1.3 ppm	13.0 ppm
Surface tension (σ) [N/m]	0.0677	0.0620	0.0510
Langmuir number (La) [-]	0.61	3.03	30.30
Surface coverage ratio (Se) [-]	0.38	0.75	0.97

6.3. Bubble shape and rise velocity

The free rise velocity of bubbles in the channel was measured utilizing X-ray radiographic images. The position of bubbles in a height range of 30 mm was traced and the rise velocity was calculated. The measured data both for clean and contaminated bubbles are shown in Fig. 6.2. For comparison and evaluation, a CCD video camera (AVT Pike F-100B) was used for clean bubbles to measure the rise velocity. The bubble's position over a height range of 100 mm at moderately high frame rates of 231.8 frames per second and at effective pixel resolution of 104 μm was continuously monitored. The difference between the measured bubble velocities for the two methods is less than 2%.
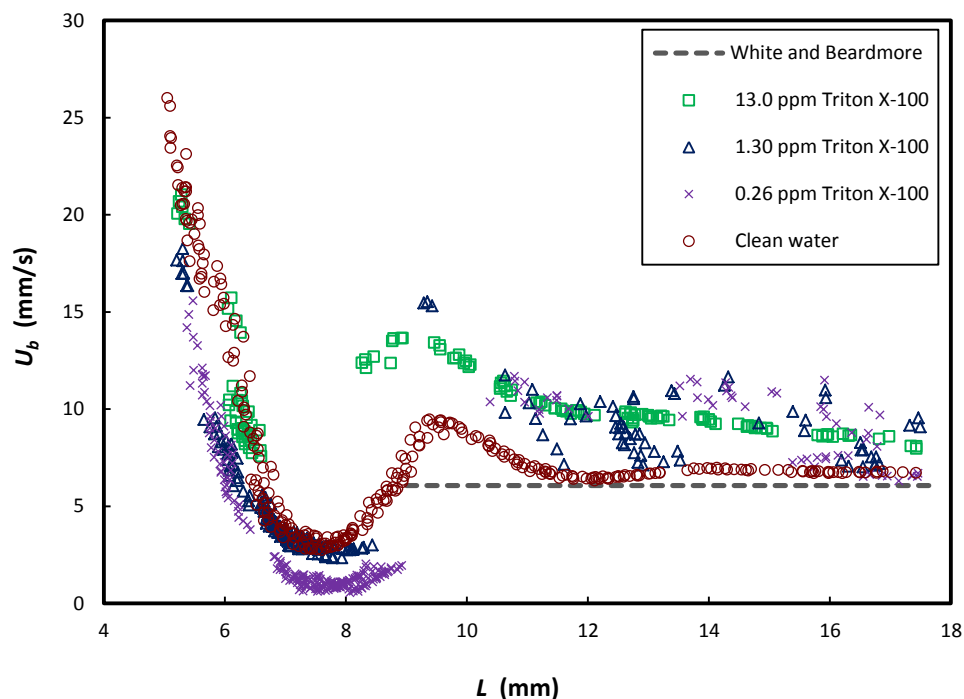
Fig. 6.2 Bubble rise velocity as a function of bubble length in clean and contaminated water.

The prediction of the correlation proposed by White and Beardmore [116] is also presented. The figure shows that the rise velocity of small bubbles strongly depends on the bubble size and increases with decrease of bubble length (for clean bubbles when $L < 7.4$ mm), while it remains constant for large bubbles (for clean bubbles when $L > 12$ mm). There is a transition region in between. In this region, despite the shape of bubbles is still bullet shape and the bubble are elongated, there is a special bubble size ($L = 9.8$ mm) at which, bubble velocity reaches maximum value. This can be attributed to the interaction effect of viscous and interfacial stress on one hand and inertial and gravitational stresses on the other hand.

Furthermore, as it is shown, contamination affects the rise velocity of bubbles. For small bubbles, presence of surfactant decreases the rise velocity of bubbles while for elongated bubbles, contamination causes an increase of bubble velocity. These findings are in accordance with other theoretical and experimental findings [47], [49], [130]. Almatroushi and Borhan [67] reported the same findings for bubbles contaminated by sodium dodecyl sulfate (SDS) in a circular pipe of 7.9 mm hydraulic diameter and showed that the surfactant decreases the motion of small bubbles because of development of adverse Marangoni stresses, while it enhances the mobility of large bubbles by increasing their deformability away from the tube wall.

Besides, as it can be seen, for clean and highly contaminated solution (13.0 ppm Triron X-100), the rise velocity both for small and elongated bubbles shows a stable trend, while for low and intermediate concentration of surfactant (0.26 and 1.30 ppm), the data points for elongated bubbles are somehow scattered and for small bubbles no scattering is observed. The reason can be attributed to the influence of the surfactant concentration on the shape of long bubbles. Hayashi and Tomiyama [49] have shown that the rise velocity of elongated Taylor bubbles is related to the nose curvature of the bubbles which is mainly governed by interfacial tension. Fig. 6.3a shows the extracted interface of a single Taylor bubble in clean water and solution of Triton X-100. As it can be seen, the bubble nose has a maximum curvature for higher concentration of surfactant in comparison with bubbles in clean and lower contaminated systems (Fig. 6.3b). The bubble nose curvature in low contaminated systems is almost the same as for clean bubble. However, as it can be seen in Fig. 6.3c, the bubble shape and curvature in lower contaminated systems start to deviate from the clean bubble shape and approaches to the

highly contaminated system in the middle of the bubble length. This change and transition in the shape of the bubble from clean to highly contaminated could be a possible reason that the rise velocity in low contaminated systems scatters between the rise velocity in clean and high contaminated systems.
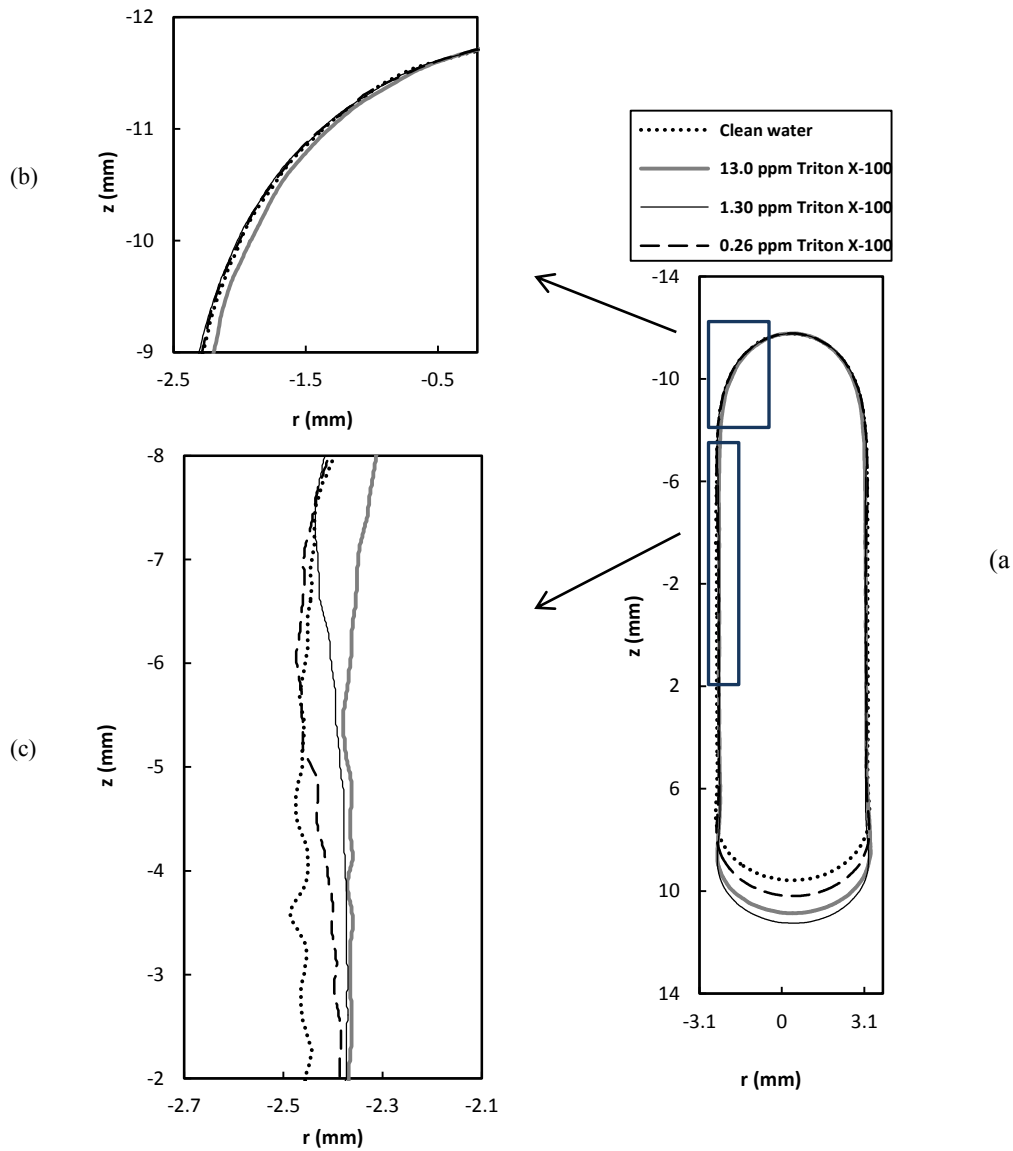
Fig. 6.3 Extracted bubble interfaces. Comparison between bubble curvature in clean and contaminated water.

An example of an instantaneous X-ray radiographic bubble image in a 6 mm diameter channel in clean and contaminated water is shown in Fig. 6.4. The nose and tail of the large Taylor bubbles both for clean and contaminated system are stable and no oscillations were observed. For smaller bubbles there exist some small shape oscillations. However, for bubbles in clean water with equivalent diameter

96

below the channel diameter, strong zig-zag movement and shape oscillations were observed (Fig. 6.4a,b) while no bubble movement and shape oscillation were detected for contaminated bubbles (Fig. 6.4g,h).

Furthermore, the impact of bubble shape and size on the rise velocity of bubbles can be seen in Fig. 6.4. In this figure V_b is the bubble volume, L the bubble length and d_{max} the bubble diameter at its maximum cross section in the channel. d_{max}, which indirectly shows the minimum available gap between the bubble and the channel wall for liquid flow, remains almost constant for large elongated bubble (for example Fig. 6.4e and f), correspondingly, it was shown in Fig. 6.2 that bubble rise velocity does not change for large bubbles.

On the other hand, at bubble length about 10 mm, d_{max} reaches the minimum value among the elongated bubbles, while the bubble rise velocity is maximum around this bubble size as is shown in Fig. 6.2 and corresponds to the maximum bubble rise velocity in transition region. As a result, it can be concluded that the changes in the rise velocity of bubbles are in accordance with size and also the shape of the bubbles in small channels.

6.4.   Bubble shape and liquid film thickness

Fig. 6.5 shows few examples of extracted bubble interface profiles with various sizes in clean and contaminated water. As it can be seen, the presence of surfactant causes a slight increase of the liquid film thickness around the bubble and as a result the elongation of the contaminated bubble. In our case where the concentration of surfactant in the liquid bulk is low (far away from CMC), the surfactants are absorbed onto the bubble interface and convected towards the stagnation point at the end of the bubble where they are accumulated. This interfacial shear generated by the flowing liquid around the bubble causes the development of a surface traction in the direction of the film (Marangoni stresses) which leads to push more fluid into the thin liquid film region and consequently causes an increase in liquid film thickness and elongation of the bubble [52],[57].

(a)	*(b)*	*(c)*	*(d)*	*(e)*	*(f)*
$V_b = 70.0$ mm^3	$V_b = 112.3$ mm^3	$V_b = 145.5$ mm^3	$V_b = 207.2$ mm^3	$V_b = 357.3$ mm^3	$V_b = 523.5$ mm^3
$L = 4.3$ mm	$L = 6.4$ mm	$L = 7.8$ mm	$L = 10.5$ mm	$L = 16.2$ mm	$L = 23.4$ mm
$d_{max} = $ -	$d_{max} = $ -	$d_{max} = 5.84$ mm	$d_{max} = 5.73$ mm	$d_{max} = 5.81$ mm	$d_{max} = 5.81$ mm

Clean water

(g)	*(h)*	*(i)*	*(j)*	*(k)*	*(l)*
$V_b = 66.1$ mm^3	$V_b = 106.8$ mm^3	$V_b = 117.3$ mm^3	$V_b = 202.2$ mm^3	$V_b = 422.9$ mm^3	$V_b = 476.8$ mm^3
$L = 4.6$ mm	$L = 6.2$ mm	$L = 6.7$ mm	$L = 10.2$ mm	$L = 18.8$ mm	$L = 21.9$ mm
$d_{max} = 5.28$ mm	$d_{max} = 5.71$ mm	$d_{max} = 5.75$ mm	$d_{max} = 5.64$ mm	$d_{max} = 5.69$ mm	$d_{max} = 5.69$ mm

Contaminated water (Triton X-100 1.3 ppm)

Fig. 6.4 Bubble radioscopic images for different bubble sizes.

This problem was firstly raised by Bretherton [102]. He theoretically analyzed displacement of long bubbles in a capillary and showed that the wetting film thickness left behind the bubbles is proportional to $Ca^{2/3}$. In the range of $Ca < 10^{-4}$, however, his model under-predicts the liquid film thickness. Bretherton [102] proposed that adsorbed impurities on the surface of bubbles may cause the discrepancy between the theory and experiment. Several investigations confirm the thickening effect both analytically [52],[53],[54],[131] and numerically [49],[57],[132] and proved that the observed discrepancy of the liquid film thickness at low Ca is due to the dominant role of Marangoni effects in

that limit. However, almost all of experimental studies that have been done so far on this subject, focused mainly on fiber coating, known as Landau-Levich problem [57]. The present work might be one of the first experimental evidence of film thickening of finite-size bubbles in small channels.

The measured liquid film thickness around the bubble at the center of mass of the bubbles for a large range of bubble lengths is shown in Fig. 6.6. The film thickness values listed in this figure are averages of at least five measurements. The error bars indicating one standard deviation about the mean are in (or smaller than) the size of the data points.

In Fig. 6.6 the effect of surfactant concentration on the film thickness of elongated bubbles, are examined by applying three different concentration of Triton X-100. As it is shown, increase of contamination causes a slight increase in liquid film thickness and its trend is consistent with the results of previous experimental and analytical investigations [57],[133]. For example, Olgac and Muradoglu [57] showed that the thickening effect of surfactants grows up as the surfactant concentration increases.

However, the film thickening effect with increase of contamination is not high. The reason may be that the range of change of surfactant concentration in our study does not have a significant effect on the interfacial surface tension. In our case, increase of surfactant concentration from 0.26 ppm to 1.30 ppm causes a reduction of only 8% in surface tension and rise of Triton X-100 concentration from 1.30 ppm to 13.0 ppm leads to a decrease of 17% in the interfacial tension.

The measured interface of clean and contaminated bubbles are presented in the form of polynomials and summarized in Appendix A.

	(a)		(b)		(c)		(d)
Clean bubble	**Contaminated**	**Clean bubble**	**Contaminated**	**Clean bubble**	**Contaminated**	**Clean bubble**	**Contaminated**
$V_b = 358.2$ mm^3	$V_b = 364.6$ mm^3	$V_b = 282.8$ mm^3	$V_b = 272.0$ mm^3	$V_b = 222.0$ mm^3	$V_b = 222.7$ mm^3	$V_b = 179.8$ mm^3	$V_b = 171.7$ mm^3
$L = 16.26$ mm	$L = 17.44$ mm	$L = 13.23$ mm	$L = 13.63$ mm	$L = 10.86$ mm	$L = 11.59$ mm	$L = 9.33$ mm	$L = 9.55$ mm
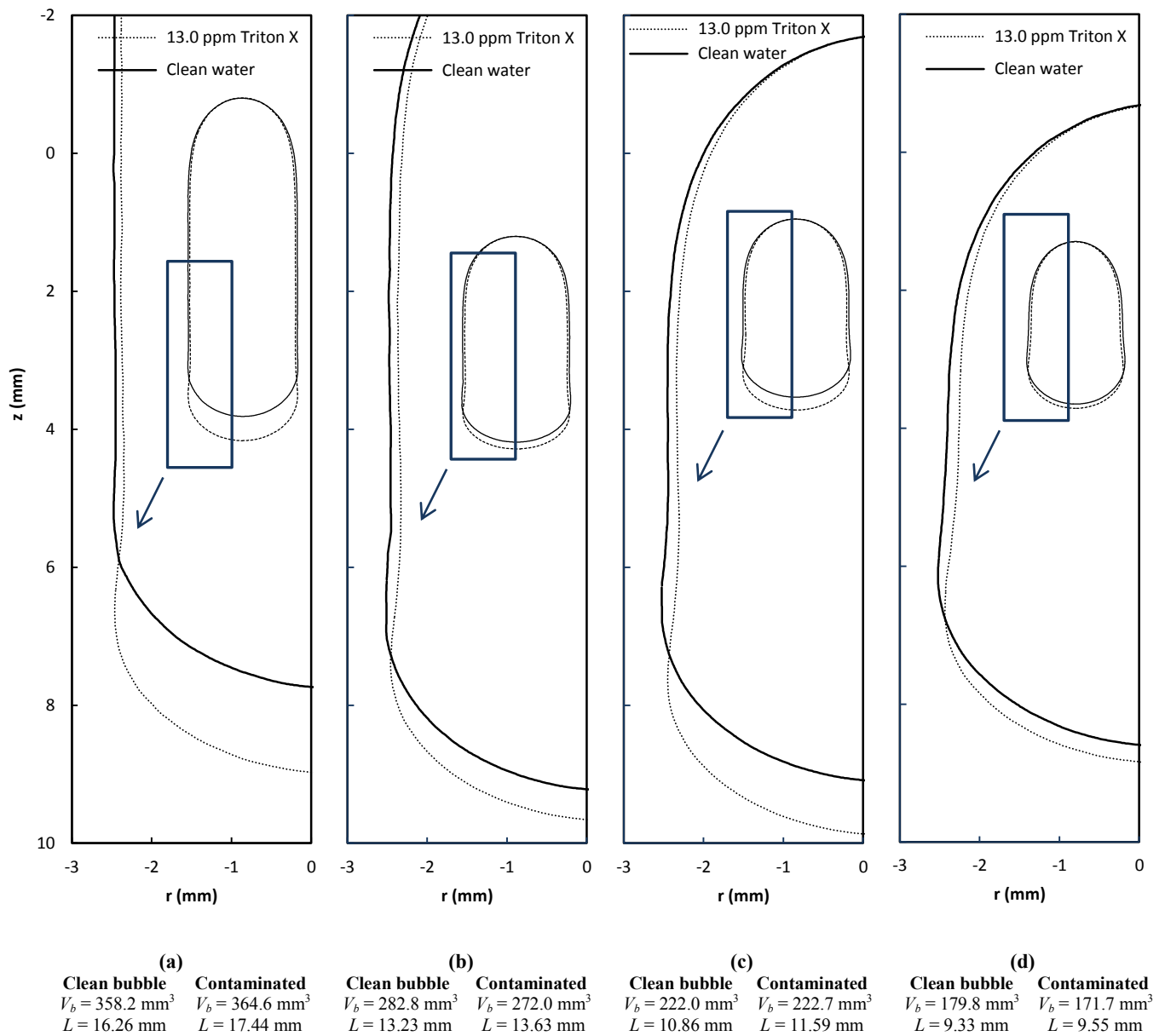
Fig. 6.5 Extracted bubble interfaces. Comparison between clean and contaminated water.
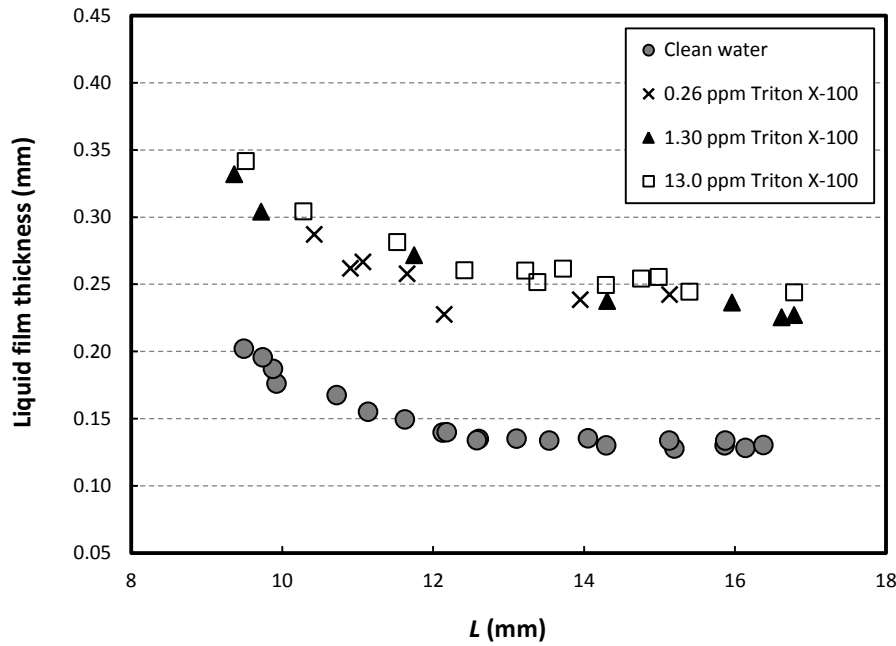
Fig. 6.6 The measured liquid film thickness around the bubble at the center of mass of the bubbles.

6.5. Mass transfer

The liquid-side mass transfer coefficient, k_L, (Eq. 4.7) for single bubbles in pure and contaminated water is shown in Fig. 6.7. The values of mass transfer coefficients plotted in this figure are averages of at least five measurements. The error bars indicate one standard deviation about the mean points. As it can be seen, contamination causes a reduction of the mass transfer coefficient for both small and elongated bubbles. The retardation of the mass transfer coefficient in the presence of surfactants can be attributed to either the hydrodynamic influence or to the formation of an interfacial barrier layer [134]. The influence of surfactant on the hydrodynamics of a moving bubble may cause modifications in the internal circulation velocities, reducing interfacial waves, and the hindrance of interfacial movement via the gradient of interfacial tension along the bubble surface (Marangoni effect) [135]. On the other hand, in the barrier layer model, which is also known as the physicochemical effect, the molecules of surfactant adsorb on the bubble interface and form a condensed monolayer. As a result, the interfacial free area for the mass transfer is reduced. When the transferring species transfer through the adsorbed layer on the interface, the interaction between the molecules of solute and surfactant

becomes an additional resistance and the rate of mass transfer is decreased. Based on this model, the mass transfer resistance will grow up with the rise in surface concentration of surfactant [134].

Furthermore, as it can be seen in Fig. 6.7, for the surfactant free system the mass transfer coefficient decreases as the equivalent bubble size ratio increases, while in contaminated water k_L does not show any considerable dependency on the bubble size ratio. In other words, the comparison between clean and contaminated bubbles indicates that presence of surfactant has a more significant impact on the dissolution rate of small bubbles. The same trend was reported for ellipsoidal and Taylor bubbles in 12.5, 18.2 and 25.0 mm pipes in presence of Triton X-100 and 1-octanol solutions by Aoki et al. [29],[79]. They showed that the interface immobilization caused by the Marangoni effects is the reason for the decrease of k_L in small bubbles. For Taylor bubbles they found that mass transfer coefficients of contaminated bubbles are also smaller than those of clean bubbles, whereas they grow with bubble size and approach those of clean bubbles. The reason could be attributed to the interface mobility of bubbles while the mass transfer coefficient of dissolving bubbles is proven to depend upon interface mobility [118]. For clean water, the high mass transfer rate is related to the internal circulation in the bubble, and the interfacial turbulence occurring with the mass transfer across an interface. For the contaminated system, the interfacial mobility will be inhibited by the Marangoni stress. Furthermore, it has been shown that contamination influences more considerably smaller bubbles [46], while concentration and surface tension gradients are more noticeable for ''small'' than for ''large'' bubbles, since their surface is less influenced by impurities and moves more freely [23]. This result is consistent with the findings concerning the rise velocity of small and elongated bubbles, while the rise velocity, shape oscillation and capillary waves of contaminated small bubbles are lower than for clean bubbles.

Furthermore, in Fig. 6.7 the influence of surfactant concentration on the mass transfer coefficient of single bubbles is evaluated. As it can be seen, for elongated bubbles, increase of surfactant concentration causes a decrease of mass transfer coefficient. For low concentration of surfactant (0.26 ppm), contamination causes a reduction of k_L by 29%. However, for higher Triton X-100 concentration (1.30 ppm and 13.0 ppm), the mass transfer coefficient reduces to 55%. This is attributed on one hand to the physicochemical nature of the used surfactant. The adsorption behavior

of Triton X-100 was shown to follow the diffusion-controlled mechanism both at the air-water and the oil-water interfaces [136],[135]. As a result the rate of surfactant transfer can be increased steadily by increasing the bulk concentration, which intensifies the hydrodynamic influence of surfactant and causes further reduction in internal circulation velocities, interfacial mobilization and increase of Marangoni stresses along the bubble surface. On the other hand, the influence of surfactant concentration on k_L can be related to the surface coverage ratio of surfactant (Se). Surface coverage ratio is directly affected by the concentration of surfactant or degree of contamination of the bubbles. In our case, for low surfactant concentration (0.26 ppm), Se is about 38% while this parameter is about 75% for 1.30 ppm solution and as it was mentioned before, the rise of the surface coverage ratio strengthens the barrier layer effect of surfactants. As a result, an increase of surfactant concentration, which corresponds to a rise of the barrier resistance of surfactants, may be another reason for decrease of mass transfer coefficient of elongated bubbles.
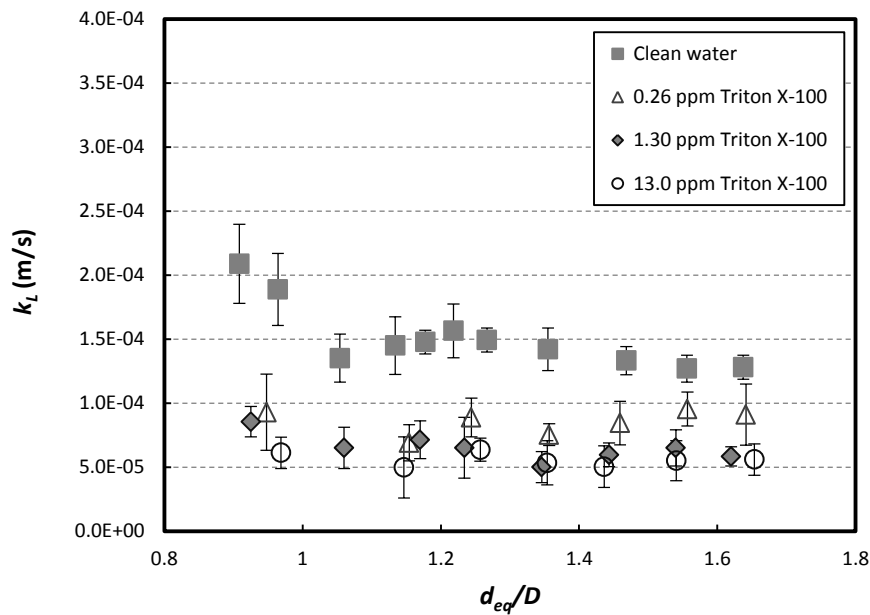
Fig. 6.7 Liquid-side mass transfer coefficients for stagnant single bubbles in clean and contaminated water.

Furthermore, Fig. 6.7 shows that for higher surfactant concentrations (1.30 ppm), addition of surfactant does not have any considerable influence on k_L. In this case, increase of surfactant concentration from 1.30 ppm to 13.0 ppm, which corresponds to a change of Se from 75% to 97%,

indicates that at high surfactant concentration, which corresponds to high coverage ratio, increase of contamination does not have a significant impact on the mass transfer coefficient of bubbles.

As it was mentioned, increase of surfactant concentrations to the CMC concentration was not possible due to the experimental limitations. However, for liquid droplets in aqueous phase, it was shown [134], [137], [138] that increase of surfactant concentration close to CMC can form a micelle zone at the trailing end of a bubble due to elevated surfactant concentration in the adjacent sublayer which causes partially remobilization of interface and consequently an increase of the mass transfer coefficient. Investigation of these phenomena for a gas bubble may be the subject of future studies.

6.6. Summary

The shape and absorption rate of an individual elongated Taylor bubble of CO_2 in contaminated water was measured in a millimeter-size channel to investigate the effect of surfactant. The bubbles were held stationary in the down-flowing liquid and the liquid-side mass transfer coefficient was determined from microfocus X-ray images. The acquired X-ray images of the bubbles were analyzed with respect to volume, surface area and length of the bubble and were utilized to obtain the liquid-side mass transfer coefficient and shape of the bubble. The comparison of the results for the clean and contaminated water showed that

- a small amount of surfactant reduces the mass transfer of Taylor bubbles;

- presence of surfactant has a more significant impact on the mass transfer rate of small bubbles;

- at high surfactant concentration which corresponds to high coverage ratio, increase of contamination does not have a noticeable influence on the mass transfer coefficient of bubbles;

- the presence of surfactants causes the change of the bubble shape and leads to a slight increase of the liquid film thickness around the bubble and as a result the elongation of contaminated bubble;

- the present work is an experimental evidence of film thickening effect of surfactants on the finite-size bubbles in small channels.

7. Mass transfer enhancement by channel vibration

7.1.   Introduction

Multiphase chemical reactors with micro- and millimetre-size channel structures are considered as a promising alternative to conventional multiphase reactors. However, due to the small diameter of crossing flow, in most cases the governing flow regime in such reactors is laminar and therefore the liquid-side mass transfer coefficient between the Taylor bubbles and liquid slugs is lower than for turbulent flow [81]. Recently, applying structural vibration or sound fields to agitate the fluidic phases is proposed to enhance the individual mass transfer coefficient [82].

In this chapter, the hydrodynamics and mass transfer behavior of a single Taylor bubble in quiescent water, whose motion is governed by the channel walls, was investigated inside of a laterally vibrated vertical channel of 6 mm inner diameter using the combination of microfocus X-ray radiography technique and optical videometry. The amplitude, A, and frequency, f, of vibration are in the range of 0 to 0.7 mm and 0 to 44 Hz, respectively. The liquid-side mass transfer coefficient was determined from microfocus X-ray images.

7.2.   Experimental

The modified experimental setup is schematically shown in Fig. 7.1a while the imaging instrumentation is presented in more detail in Fig. 7.1b. The glass tube is placed between the X-ray source and a two-dimensional flat panel X-ray image detector. It is fixed between two horizontal arms

which are connected to the vibrator. The arms transform the horizontal sinusoidal motion of the vibrator to the capillary. In this study the liquid is quiescent and the single Taylor bubbles are freely rising and there is no downward liquid flow to fix the bubble in front of the X-ray source. The passing of single bubbles takes about 2 seconds depending on the size of the bubbles. A Taylor bubble is generated by the injection of some finite amount of gas into the liquid through an axially aligned metallic needle inside the tube upstream the observation section [139]. The amount of gas injected into the liquid is controlled by a remotely operated fast acting solenoid valve.

(a) (b)
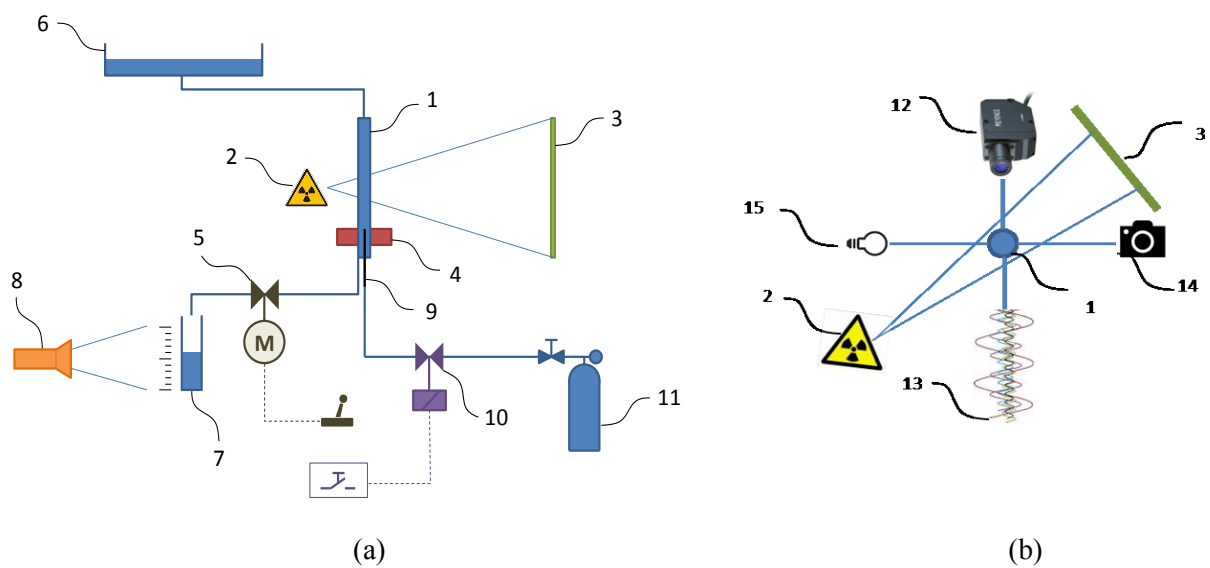
Fig. 7.1 Schematic drawing of the experimental setup: a) Hydraulic circuit with observation section (1), microfocus X-ray source (2), flat panel X-ray image detector (3), vibrator (4), remotely controlled motorized needle valve (5), upper reservoir (6), lower reservoir (7), video camera (8), gas injection line (9), fast solenoid valve (10), gas cylinder (11), b) Top view of special instrumentation and actuators: LCDM (12), Mechanical vibrator (13), CCD camera (14), LED light source (15).

Fig. 7.1b shows the top view of the actuator and the imaging instrument. It comprises of an X-ray source, a flat panel X-ray detector, a high-resolution camera, a LED light source, the mechanical vibrator, and a laser confocal displacement meter (LCDM). The Taylor bubble was radioscopically monitored at an exposure time of 100 ms and a frame rate of 10 Hz. The mechanical vibrator (Otto Schön, 11075) is connected to the amplifier which is able to vibrate the vertical channel in the horizontal (lateral) direction in a frequency range between 3 Hz and 80 kHz and an amplitude up to 7.00 mm. However, in this study the imposed amplitude and frequency of vibration were in the range

of $0 - 0.7$ mm and $0 - 44$ Hz, respectively. Due to the mechanical limitations of the experimental setup, it was not possible to impose broader amplitudes and higher frequencies. The amplifier is controlled by a wave form generator (Agilent 33250A). The signal of the generator is transferred to the amplifier and then to the vibrator. The strength of the signal is adjusted by both the amplifier and generator.

The camera is a CCD video camera (AVT Pike, F-100B) which continuously monitored the bubble's position in an axial range of 30 mm. The camera is connected to the PC via a digital interface and is controlled using AVT smart view software. The camera is fixed on an adaptable support which enables positioning of the camera to adjust the field of view. The recorded images of the bubble oscillation were processed using MATLAB. The laser confocal displacement meter (Keyence, LT9030M) was used to adjust and measure of the amplitude of channel vibration.

The protocol of each set of experiments is as follows. Before starting each experiment, a high countercurrent flow rate was adjusted and a large number of bubbles were injected into the liquid to flush the injection needle and pipes and to ensure that they were filled with the injection gas only. At the beginning of the experiments a number of reference X-ray images were acquired showing the liquid filled tube only. The desired value of frequency for channel vibration was set for the vibrator. The value of the amplitude of oscillation was measured by the LCDM and controlled by changing the output power of the wave form generator. Then, a bubble was injected into the liquid. As soon as the ascending bubble reached the field of view, the CCD camera recording was started. Synchronously, we scanned the bubble by X-ray imaging during the dissolution process of the bubble.

7.3. X-ray image acquisition

7.3.1. Bubble size measurement

The X-ray image processing and calibration used in these experiments are mostly the same as section 3.4. However, as it was mentioned before the bubbles do rise in these experiments. Image averaging is not possible during studies of mass transfer, since the bubble shape is continuously changing. Fig. 7.2 shows X-ray radiographs of dissolving (CO_2) bubbles in the oscillating channel. As it can be seen,

bubble rise and oscillation of the channel cause undesired motion blur. The size of each X-ray radiographs was 15 mm x 30 mm. This size comes from a compromise to have the maximum field of view to trace the bubble on one hand and to have the maximum spatial resolution and minimum signal to nose ratio on the other hand. During the mass transfer study the change in the volume of bubble was different and depending upon the amplitude and frequency of vibration. It varied between 4% and 14% of initial volume of bubble. As a result, only the integral extinction $\sum_{ij} E_b$ of non-averaged X-ray images (Fig. 7.3a) was measured as a function of time and correlations equivalent to Eq. 3.3 was used to infer instantaneous bubble volume and their dynamics. Thereby we utilized the beforehand measured calibration constants [140].

Due to the finite exposure time, the channel oscillation causes periodically changing blur of the X-ray projections, which in turn causes periodical variations in calculated integral attenuation $\sum_{ij} \boldsymbol{E}_b$ when using a static reference, $\boldsymbol{E}_{ref}$. Amplitude and phase of that periodically changing offset were estimated using fast Fourier transformation (FFT) analysis and the fluctuating integral attenuation was corrected accordingly.

The uncertainty in measured $\sum_{ij} \boldsymbol{E}_b$ was less than 2%. The uncertainty in measurement of V_b is the same due to Eq. 3.3 which is included in the uncertainty calculation of the mass transfer coefficient.
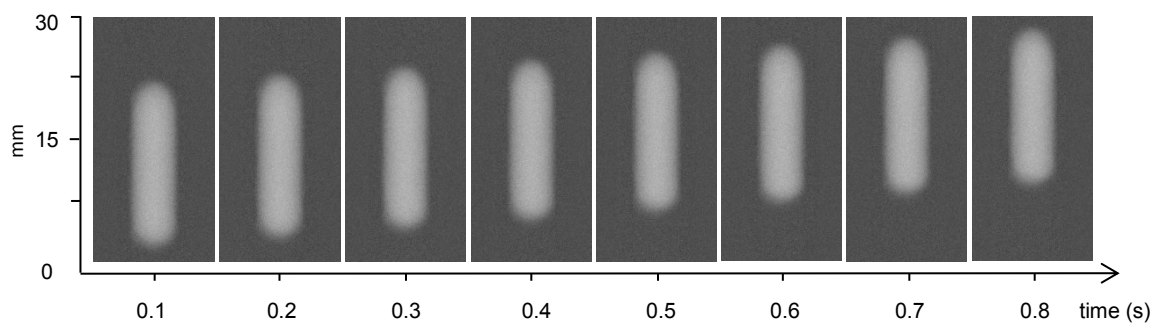
Fig. 7.2 X-ray radiographs of dissolving (CO_2) bubbles in an oscillating channel ($f = 40$ Hz).
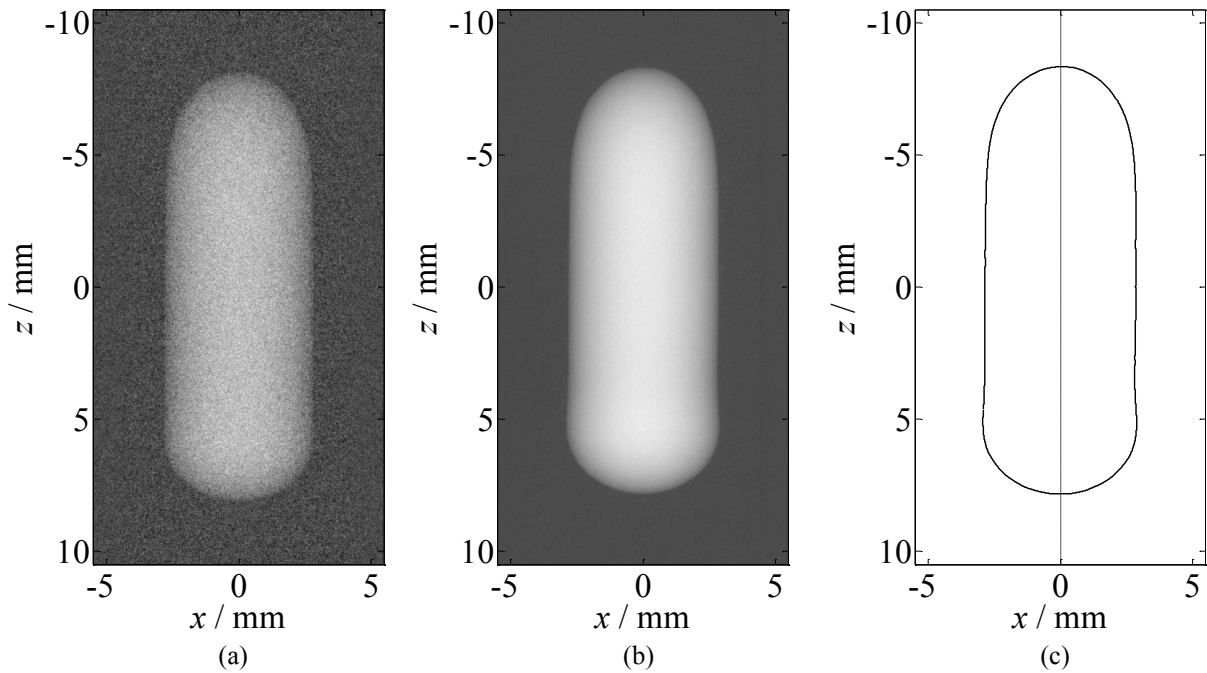
Fig. 7.3 (a) Extinction image of a dissolving Taylor bubble as it passes the X-ray detector (raw data). (b) Averaged image of the 'calibration bubble', whose position was held fixed in front of the X-ray detector by countercurrent liquid flow. (c) Extracted bubble interface projection (solid line).

7.4. Measurement and adjustment of the vibration amplitude

The oscillation induces a horizontal motion of the vertical channel axis and as it was mentioned, the frequency and amplitude of oscillation were controlled by wave form generator. But, the resulting amplitude of the motion cannot be deduced from the wave form generator signals and therefore we measured and set its value using the LCDM at the beginning of each experiment. However, due to injection and movement of bubble, in some cases, the oscillation amplitude of channel was slightly affected. Therefore, the videoscopic observation data from CCD camera with effective pixel resolution of 108 µm was used to double check the data. Fig. 7.4 shows the measured channel vibration amplitudes from the videography data.
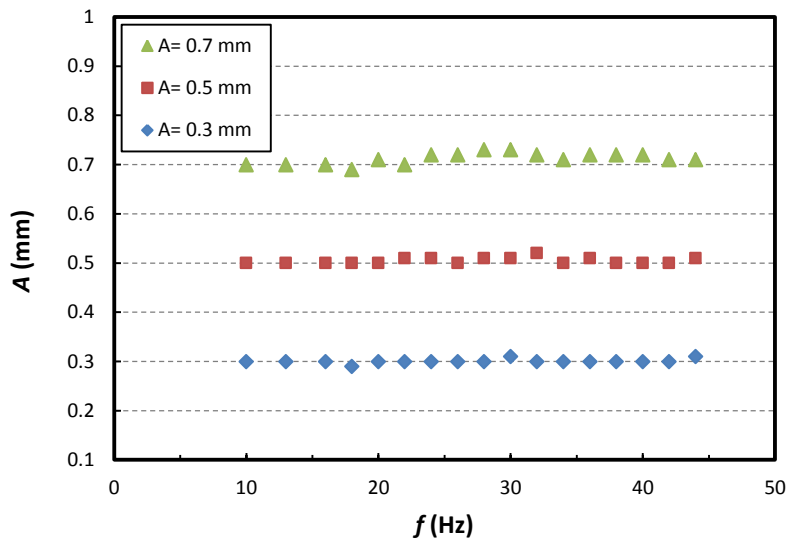
Fig. 7.4 Measured channel vibration amplitude using the videoscopic data from the CCD camera.

7.5.   Bubble shape and rise velocity

Fig. 7.5 exemplarily shows a non-dissolving Taylor bubble as it rises in the oscillating channel within one full period of oscillation. As Hashmi et al. [95] discussed, the bubble interface may be considered as a soft membrane which is able to oscillate under the action of excitation. Depending upon the frequency and amplitude of the external vibration, the response of the bubble can be linear or non-linear. As it can be seen, the horizontal channel motion forces the liquid via its momentum to the backside of the channel (with respect to motion direction) and thus pushes the bubble tip in the direction of motion. As a result, the liquid film thickness increases at the backside of the tube which leads to downward movement of additional amount of liquid along the Taylor bubble side.

Furthermore, the channel oscillation causes waves on the surface of bubble which travel along the bubble axis. As it can be seen in Fig. 7.5, on one hand, the surface wave axial velocity is mainly related to liquid velocity in the film. On the other hand, the waves on the surface of the bubble are not symmetric. This behavior was also reported by Kubie [87] in laterally oscillating vertical pipes and also by Madani et al. [86] for axial vibration of vertical tubes. For the later case Madani et al. [86] conjectured that the non-axisymmetric surface wave motion leads to a higher downward liquid flow rate and also an increase of bubble rise velocity.

110
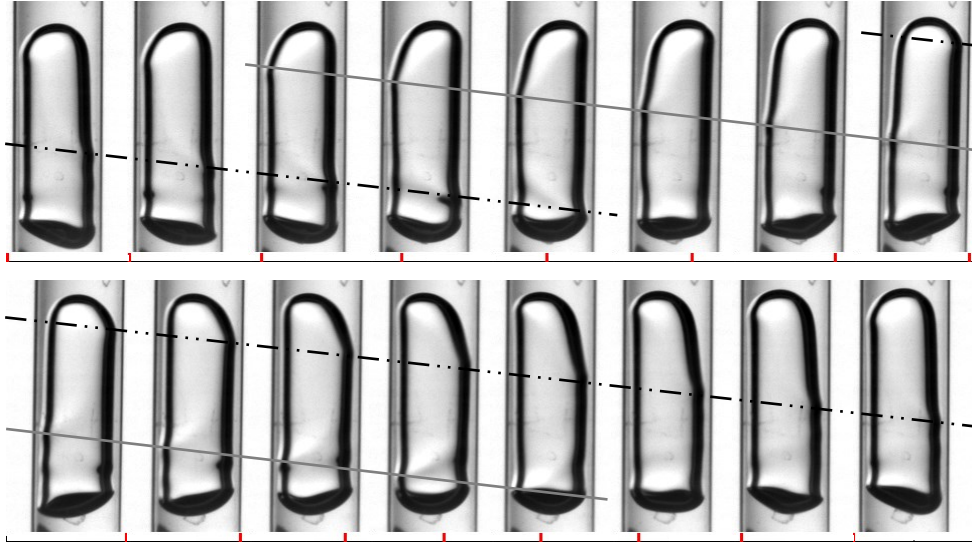
Fig. 7.5 An air Taylor bubble (not dissolving in the liquid) as it rises in the oscillating channel within one full period of oscillation (f = 12 Hz). The vertical position of the surface wave crest on the Taylor bubble's left and right hand side is indicated by the dashed and continuous line. The relative horizontal position of the tube is indicated by the marker at the bottom of each image.

The free rise velocity of bubbles (U_b) in the stagnant liquid in the channel was measured utilizing the CCD video camera which monitored the front tip of the bubbles. The position of the bubble's front tip was tracked over an axial range of 30 mm at a frame rate of 188.2 frames per second and an effective pixel resolution of 108 μm. Depending on the rise velocity of the bubbles, 180 to 950 images were analyzed and tracked to measure the rise velocity. This way the instantaneous bubble front tip free rise velocity was obtained. These data was cross-compared to the ones obtained from the X-ray radiographic images and it was found that the difference between the measured values by two methods is about 2%.

Fig. 7.6 shows the measured rise velocity of a freely rising non-dissolving (air) Taylor bubble in the circular channel as a function of channel oscillation frequency. We studied bubbles between L = 20 mm and 22 mm and d_{eq}/D of 1.5 to 1.6. The maximum uncertainty in measured bubble rise velocity is estimated to be 3%. As it can be seen, for non-oscillating channel the Taylor bubbles rises at 6.9 mm/s. An increasing amplitude and frequency of the horizontal channel motion leads to increase of the bubble rise velocity. Moreover, the amplitude of vibration has a considerable influence on the rise velocity of the bubbles. For example, at 26 Hz a change of amplitude from 0.3 mm to 0.7 mm causes an increase of bubble velocity from 10.11 mm/s to 28.95 mm/s.

Furthermore, as it can be seen, the data show some intensifying effect at certain frequencies. At these frequencies the bubble vibration and bubble rise velocity reach their maximum value. This behavior is consistent with the observation of the Ellenberger et al. [9] for gas holdup of bubble columns. They showed that vertical vibration of bubble columns shows some enhancing effect at specific frequencies where the gas holdup is maximum. In our system, our observations revealed that this intensifying effect is more pronounced at higher amplitude and is dependent upon the parameters of the mechanical system.
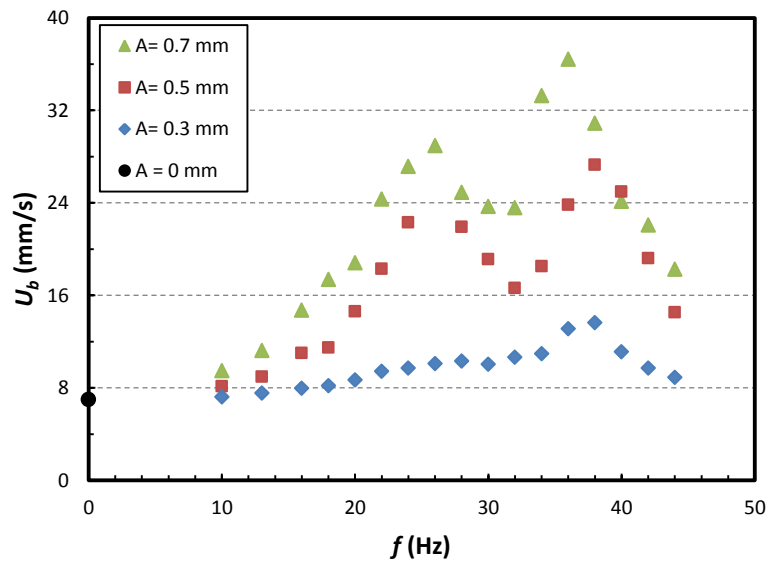
Fig. 7.6 Measured rise velocity of a freely rising non-dissolving Taylor bubble in a circular channel as a function of channel oscillation frequency and amplitude.

7.6.   Interfacial waves

The horizontal channel oscillation induces surface waves on the left and right-hand side of the Taylor bubble (left and right with respect to the observers point of view), which travel downward on the bubble interface. The travel velocity is assumed to be constant, which seems to be true at least for the center part of the Taylor bubble away from the front and rear bubble cap. Fig. 7.7 presents the surface wave travel velocity. The values of the surface wave travel velocity plotted in this figure are averages of at least three measurements. The error bars indicate one standard deviation about the mean points. The surface wave travel velocity shows a similar behavior as the bubble rise velocity. It increases with increasing amplitude and frequency of channel motion. In detail, the maximum and minimum of both

112

the bubble velocity and bubble surface wave velocity are the same. This means that the increase and decrease of bubble rise velocity are corresponding with the variation of bubble surface wave velocity. Moreover, it should be noted that for large amplitude oscillations of the channel, at the frequencies where the rise velocity is maximum, a slight vertical oscillation of channels was observed which can affect the motion of oscillating bubbles. Furthermore, videometric observation reveals that with increasing of oscillation amplitude, the bubble surface oscillation increases progressively. The bubble surface oscillation starts from volume pulsation to the small surface waves and then to chaotic surface distortion. This behavior is in accordance with the observation reported by Dong et al. [81] in horizontal microchannels.
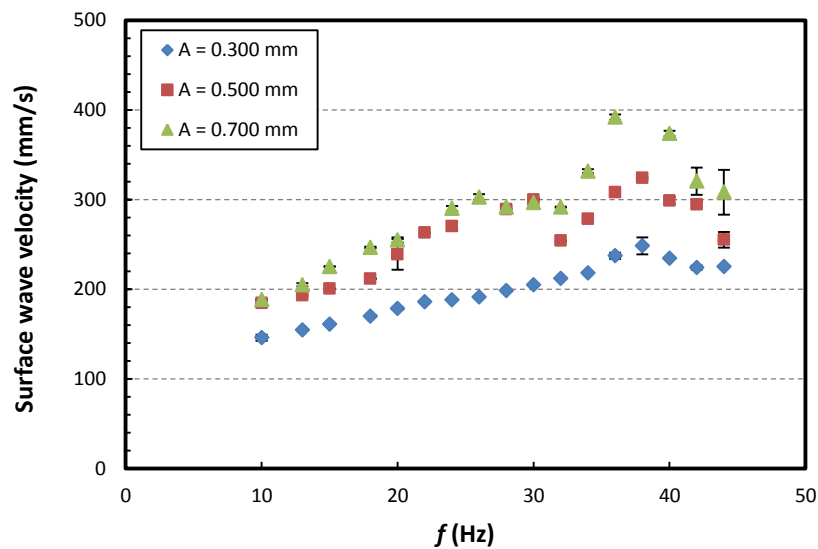
Fig. 7.7 Surface wave travel velocity of rising bubbles.

The videoscopic data of non-dissolving bubbles (Fig. 7.5) show periodic occurrence of bubble surface waves. The surface wave occurrence frequency was measured and is shown in Fig. 7.8. As it can be seen, the surface waves occur at exactly the same frequency as the horizontal channel oscillation (one new wave per horizontal motion period) and are independent of the oscillation amplitude. This behavior is in contrast with the observation of Dong et al. [81] in microchannels which indicated that the bubble surface waves oscillate periodically at half the driving frequency, which is a key feature of a Faraday wave.
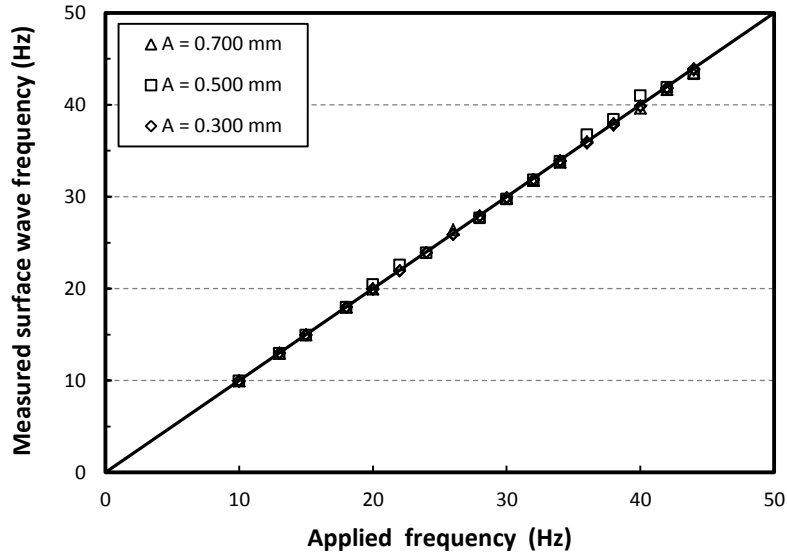
Fig. 7.8 Surface wave occurrence frequency of rising bubbles.

7.7.   Mass transfer coefficient

We carried out the experiments to measure the influence of vibration frequency and amplitude on the mass transfer rate. The liquid-side mass transfer coefficients, k_L, according to Eq. 4.7 for individual rising dissolving Taylor bubbles in stagnant liquid are shown in Fig. 7.9. It should be noted that the variation of bubble pressure due to the rising of the bubble (Δh = 30 mm) is less than 0.4%. Therefore, P can be assumed constant during the experiments. For dissolving bubble experiments (CO_2 bubbles) the injected (initial) bubble size was set to L = 19 mm to 22 mm and d_{eq}/D = 1.5 to 1.6. The values of the mass transfer coefficient plotted in this figure are averages of at least three measurements. The error bars indicate one standard deviation about the mean points.

As it can be seen, oscillation causes an increase of the mass transfer coefficient in comparison with the non-oscillation case (single point at f = 0 Hz). At constant vibration amplitude, an increase of frequency causes also an increase of mass transfer coefficient. The rise of k_L is not even and has some fluctuations. For vibration with an amplitude of 0.7 mm, at frequencies larger than 30 Hz due to very large shape oscillations of bubbles and high bubble rise velocity, the number of data to calculate the mass transfer coefficient was not enough. Therefore, k_L could not be measured and reported. However, the trend shows a clear rising behavior of k_L. Furthermore, increase of oscillation amplitude leads to an

114

increase of the mass transfer rate, which is more pronounced for higher amplitudes. For example for a vibration amplitude of 0.3 mm, the liquid-side mass transfer coefficient increases at maximum by 79.9%, while the increase is 186.1% for a vibration amplitude of 0.5 mm.
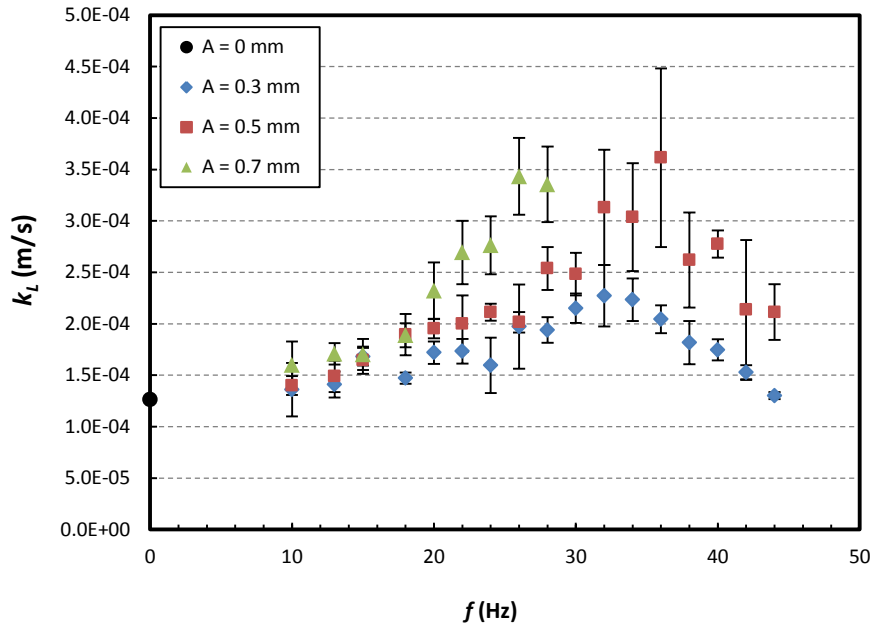
Fig. 7.9 Measured mass transfer coefficient for oscillating bubbles with initial size $1.5 < d_{eq}/D < 1.6$.

For a better understanding of the behavior of dissolving bubbles the free rise velocity of CO_2 bubbles was measured and is given in Fig. 7.10. The measurement conditions and procedure were the same as air bubbles. The maximum uncertainty in measured bubble rise velocity is estimated to be 3%. As it can be seen, an increase of vibration frequency and amplitude causes faster motion of rising bubbles, which is in accordance with the non-dissolving bubbles (Fig. 7.6). However, there are some differences in the trend of rise velocity between CO_2 and air bubbles. The local maximum points are more pronounced for non-dissolving bubbles compared to the CO_2 bubbles. The reason could be attributed to the multipart behavior of dissolving bubbles. On one hand, CO_2 bubbles are dissolving and their front tip is shrinking which means their front tip is descending and at the same time whole bubble is rising. On the other hand, because of dissolution of bubble, the bubble volume is decreasing which also affects hydrodynamics of the bubble and consequently the free rise velocity of bubbles which causes some differences in trend of dissolving and non-dissolving bubble rise velocity.

Moreover, comparison of Fig. 7.9 and Fig. 7.10 shows that there is a fairly good consistency between the values of mass transfer coefficient and bubble rise velocities. For example in the range of our experiment for a vibration amplitude of 0.3 mm, the maximum bubble rise velocity occurs at frequencies 32 Hz to 34 Hz and k_L also has a maximum at this frequency. On the other hand, as it was shown in Fig. 7.6 and Fig. 7.7, for any vibration amplitude considered in this study, the trend and the peak values of bubble rise velocities are corresponding to the trend and peak values of bubble surface waves, which means that the rise velocity and surface wave velocity are directly related to each other. Therefore, in case of CO_2 bubbles where there is a fairly good agreement between the values of mass transfer coefficient and bubble rise velocities, it can be concluded that the increase and decrease of mass transfer coefficient of rising bubbles as a function of vibration amplitude and frequency is a function of bubble surface wave velocity.
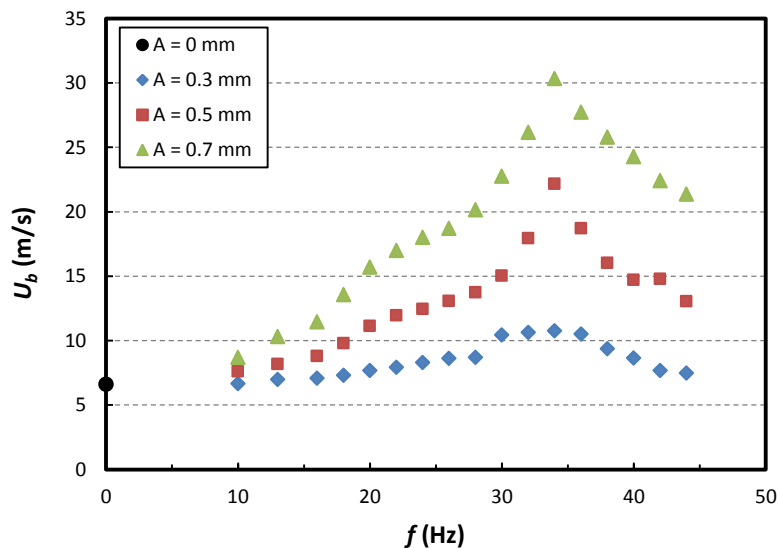
Fig. 7.10 Free rise velocity of dissolving bubbles.

Furthermore, as it can be seen in Fig. 7.5, the bubble surface wave oscillation directly influences the hydrodynamics of the liquid film and therewith the gas–liquid interface in the falling liquid film region around the bubble and causes an increase of mixing in this region. As it is known, the flow regime in this region is laminar and mass transfer is performed due to diffusion mechanism between the layers. Therefore, vibration of the channel causes the reduction of the liquid-side mass transfer

resistance between the streamlines and consequently leads to the enlargement of mass transfer rate. On the other hand, bubble surface waves generated by channel oscillation cause the increase of interfacial area between the bubbles and liquid phase which is another mechanism for enhancement of mass transfer.

For overall comparison of dissolution rate of bubbles in oscillating and non-oscillating channels, the mass transfer rate of oscillating bubbles were calculated in the form of dimensionless Sherwood number and Peclet number. We reported the data in the form of modified Sherwood number,

$$Sh^* = \frac{k_L A_{eq}}{D_c D} .$$ Eq. 2.7

The Sherwood number data are shown in Fig. 7.11. The prediction of the correlation developed by Haghnegahdar et al. [141] (Eq. 4.9) is also presented. This correlation is developed for the mass transfer of elongated bubbles in water in non-oscillating millimeter-size channels with a hydraulic diameter ranging from 6.0 mm to 8.0 mm.
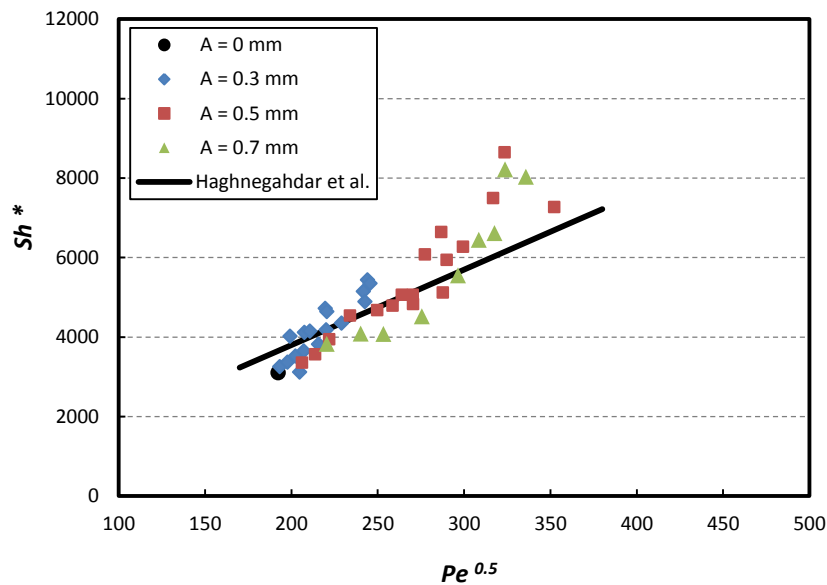
Fig. 7.11 The experimental data for oscillating channels in the form of modified Sherwood number accompanying with predicted data by the correlation proposed by Haghnegahdar et al. [141].

As it can be seen in Fig. 7.11, for low amplitude vibration (A = 0.3 mm) and also for channel oscillations with high amplitude but low frequencies, the experimental data fits to our previously derived correlation for non-oscillating bubbles. It should be noted, however, that the non-oscillating

bubbles were held stationary in a downward flow of liquid while the agitated bubbles propel themselves through stagnant liquid. At about $Pe^{0.5} = 280$ higher amplitude and frequencies of the oscillation do not only increase the bubble velocity (Peclet number) but also the mass transfer beyond the prediction of the correlation for non-oscillating bubbles. This increase in mass transfer is gained from the deformation turbulence induced by the shaking.

To sum up, the intensification of mass transfer with increase of amplitude/frequency of vibration is primarily attributed to the increase of the bubble surface wave oscillation that causes an enlargement of contact area between the phases and a reduction of mass transfer resistance in the liquid-side boundary layer [94]. Nonetheless, understanding the exact mechanism of mass transfer enhancement and obtaining a fundamental model require a more detailed analysis in the future.

7.8. Summary

The motion, shape and dissolution rate of individual elongated Taylor bubbles of air and CO_2 in water was studied in a millimeter-size channel to investigate the effect of low-frequency horizontal vibration of the channel. The bubbles were freely rising in stationary liquid and the liquid-side mass transfer coefficient was determined from microfocus X-ray images. The acquired X-ray images of the bubbles were analyzed with respect to volume, surface area and length of the bubble and were utilized to obtain the mass transfer coefficient. The rise velocity and surface wave motion of bubbles were analyzed via videometric observation with a CCD camera. The comparison of the results for the stationary and oscillating channel showed that

- mechanical vibration of the channel is able to enhance the liquid-side mass transfer coefficient between the gas and liquid phases in millimeter-size channels from 80% to 186%;

- the mass transfer rate positively correlates with frequency and amplitude of oscillation, which is more pronounced for higher amplitude;

- channel oscillation causes an enlargement of free rise velocity of bubbles, which is mainly attributed to development of bubble surface waves;

- the intensification of mass transfer with increase of amplitude/frequency of vibration is mainly attributed to the increase of the bubble surface wave oscillation that causes an enlargement of contact area between the phases and also a reduction of mass transfer resistance in the liquid-side boundary layer.

8. Conclusions and outlook

8.1. Overall conclusion

Gas-liquid two-phase reactors with micro- and millimeter-size channel structures are being increasingly used in different applications such as gas absorption, catalytic hydrogenation, biochemical conversions, direct fluorination and others. The main advantage of small channel multiphase reactors is creation of a large volumetric interfacial area. In comparison with common column contactors like trickle bed reactors, they also provide lower pressure drop for a given specific contact area. The dominant flow pattern in such channels is segmented slug flow or bubble-train flow of elongated bubbles and slugs which is an ideal flow regime to improve transport phenomena performance. However, a complete understanding of various parameters and different variables are still missing. In this work the goal was to investigate the fundamentals of Taylor bubble behavior in millimeter-size channels and to examine the influence of different parameters on the performance of the two-phase gas-liquid milli-channels. The obtained results gave a precious and deeper knowledge of small channel contactors. The findings and conclusions from the different parts of presented work are summarized as follows.

8.2. Influence of shape and cross sectional shape of channel

The absorption rate of single Taylor bubbles of carbon dioxide in water were investigated in vertical milli-channels using high-resolution X-ray imaging. The liquid-side mass transfer coefficient was

calculated by measuring the changes in the size of the bubbles at constant pressure. The experiments covered a large range of initial Taylor bubble lengths varying from 5 mm to 22 mm. The utilization of high-resolution microfocus X-ray visualization enabled the acquisition of a series of high-resolution radiographic images of nearly stationary Taylor bubbles. The processed images gave the volume, interfacial area and length of the bubble with high accuracy as a function of time and were used to evaluate the liquid-side mass transfer coefficient between bubble and liquid using the mass conservation equation.

In case of circular channels, the results show that Sherwood numbers have a large dependency on the bubble length and also equivalent diameter which is in accordance with previous results for larger pipe sizes. However, the values of measured Sherwood numbers could not be predicted by available correlations which are valid only for larger pipes. As a result, a new mass transfer correlation in the form of modified Sherwood number and as a function of Peclet number as well as ratio of bubble equivalent diameter to capillary diameter (d_{eq}/D) was presented. The proposed correlation is applicable for a large range of d_{eq}/D ratio from 0.8 to 1.6 (or $0.75 < L/D < 3.6$) with high accuracy.

The comparison of the results for the square and circular channels showed that despite the fact that the rise velocity of bubbles in the square channel is about three times higher than in the circular channel, the liquid-side mass transfer coefficient is relatively the same. Furthermore, the results show that in square channel the dissolution curves of square channels are relatively even, while the dissolution curves of circular channels exhibit some distinguishable change in the slope. In addition, it is shown that the calculated liquid-side mass transfer coefficient based on the measured data show good agreement with the data predicted by the penetration theory.

8.3.   Effect of presence of surfactant

The shape and absorption rate of an individual elongated Taylor bubble of CO_2 through contaminated water was measured in a millimeter-size channel to investigate the effect of surfactant. The bubbles were held stationary in the down-flowing liquid and the liquid-side mass transfer coefficient was determined from microfocus X-ray images. The comparison of the results for the clean and contaminated water showed that

- a small amount of surfactant reduces the mass transfer of Taylor bubbles;

- presence of surfactant has a more significant impact on the mass transfer rate of small bubbles;

- at high surfactant concentration which corresponds to high coverage ratio, increase of contamination does not have a noticeable influence on the mass transfer coefficient of bubbles;

- the presence of surfactants causes the change of the bubble shape and leads to a slight increase of the liquid film thickness around the bubble and as a result the elongation of contaminated bubble;

- the present work is an experimental evidence of film thickening effect of surfactants on the finite-size bubbles in small channels.

8.4. Influence of channel oscillation

The motion, shape and dissolution rate of individual elongated Taylor bubbles of air and CO_2 in water was studied in a millimeter-size channel to investigate the effect of low-frequency horizontal vibration of the channel. The bubbles were freely rising in stationary liquid and the liquid-side mass transfer coefficient was determined from microfocus X-ray images. The rise velocity and surface wave motion of bubbles were analyzed via videometric observation with a CCD camera. The comparison of the results for the stationary and oscillating channel showed that:

- mechanical vibration of the channel is able to enhance the liquid-side mass transfer coefficient between the gas and liquid phases in millimeter-size channels from 80% to 186%;

- the mass transfer rate positively correlates with frequency and amplitude of oscillation, which is more pronounced for higher amplitude;

- channel oscillation causes an enlargement of free rise velocity of bubbles, which is mainly attributed to development of bubble surface waves;

- the intensification of mass transfer with increase of amplitude/frequency of vibration is mainly attributed to the increase of the bubble surface wave oscillation that causes an enlargement of contact area between the phases and also a reduction of mass transfer resistance in the liquid-side boundary layer.

8.5. Outlook

In this study the influence of some of the main parameters of Taylor flow on the mass transfer and motion of Taylor bubbles in micro- and milli-channels have been investigated experimentally. The obtained results provided a better understanding regarding the performance of small channel contactors. However, there exist some unknown aspects which need to be explored. In following the suggestions for further work and some of the research challenges as the outcome of presented study are mentioned.

The dissolution rate of Taylor bubbles in circular and square milli-channels were investigated and the influence of bubble shape, bubble size, channel size and channel cross sectional shape was studied. However, there are still some open questions regarding the effect and role of the flow field in liquid and gas phases. The velocity distribution inside the liquid film and also velocity field in the gas bubbles and their influence on the dissolution rate of bubbles are import issues which needs to be explored experimentally specially in milli-channels.

Regarding the surfactants, it was shown that the presence of surfactant has a noticeable impact on the shape and mass transfer of bubbles. However, further investigations are required to detect the effect of contamination on the gas bubble and liquid slug flow fields and the mechanism of their influence on the mobility and dissolution rate of Taylor bubbles.

The vibration of the milli-channel as an intensifying technique for enhancement of the gas-liquid mass transfer was investigated in this work. It was found that the mass transfer rate depends upon the frequency and amplitude of oscillation and this effect is more noticeable for higher amplitudes. Experiments for even higher amplitudes and frequencies may be the subject of future investigations.

Since one of the main applications of Taylor flow is in monolithic reactors, and because the internal surface of monoliths are usually coated. The investigation of the effect of internal roughness of

channel can be of great benefit. To study the influence and the role of roughness of the channel on the liquid film thickness, liquid film velocity field, the bubble rise velocity and also on the mass transfer coefficient of bubbles is an important subject for future development of milli-channels for industrial applications. In this regard, application of X-ray imaging technique can be the first step.

Appendix A

Interface data of clean and contaminated bubbles

The interface data of clean and contaminated bubbles shown in Fig. 6.5 are fitted in the form of polynomials and presented in Table A.1. In this table, r_b is bubble radius, z is axial distance from the head of the bubble, a_0 to a_{20} are polynomial coefficients and dev_{max} is the maximum deviation in absolute distance between the interface sampling points extracted from the x-ray images and their nearest points on the fitted polynomial curve.

Table. A.1 Interface data of clean and contaminated bubbles shown in Fig. 6.5

$r_b(mm) = a_{20}z^{20} + a_{19}z^{19} + a_{18}z^{18} + a_{17}z^{17} + a_{16}z^{16} + a_{15}z^{15} + a_{14}z^{14} + a_{13}z^{13} + a_{12}z^{12} + a_{11}z^{11}$ $+ a_{10}z^{10} + a_9z^9 + a_8z^8 + a_7z^7 + a_6z^6 + a_5z^5 + a_4z^4 + a_3z^3 + a_2z^2 + a_1z + a_0$				
Fig. 6.5	**a**		**b**	
Coefficients	clean	contaminated	clean	contaminated
a_{20}	-4.80294695935788E-15	-9.40421305721929E-16	-1.24211940306675E-14	-2.24049589508817E-14
a_{19}	7.79266701796566E-13	1.62440851637228E-13	2.36763272004498E-12	2.97693316128133E-12
a_{18}	-5.85750889133396E-11	-1.29930403099477E-11	-2.09173218752898E-10	-1.83041778891067E-10
a_{17}	2.70696987426965E-09	6.38633660881426E-10	1.13559401945631E-08	6.91210108611807E-09
a_{16}	-8.60726676073100E-08	-2.15860698170760E-08	-4.23443634996111E-07	-1.79421624357313E-07
a_{15}	1.99672241348144E-06	5.32014185913731E-07	1.14827197738592E-05	3.39554188811152E-06
a_{14}	-3.49671870813340E-05	-9.89258532039311E-06	-2.33996134704937E-04	-4.84964500451427E-05
a_{13}	4.71858227548241E-04	1.41658384951966E-04	3.65782932967479E-03	5.33923875125635E-04
a_{12}	-4.96490014850410E-03	-1.58072907656754E-03	-4.46159894598517E-02	-4.58990766259511E-03
a_{11}	4.09608635990690E-02	1.38220240165315E-02	4.35893173834714E-01	3.10299787267823E-02
a_{10}	-2.65085817034957E-01	-9.47553302295150E-02	-3.61601578812868E+00	-1.65442577025842E-01
a_9	1.34015337060141E+00	5.07212650697691E-01	2.83584401456879E+01	6.95224638185723E-01
a_8	-5.24610954865750E+00	-2.10176365496657E+00	-2.29949402031930E+02	-2.29393978205187E+00
a_7	1.56799510670546E+01	6.65060977606740E+00	1.84181273483385E+03	5.90167309055049E+00
a_6	-3.50645927689308E+01	-1.57588630366621E+01	-1.28544848134067E+04	-1.17086625574475E+01
a_5	5.70318262445195E+01	2.72187299544167E+01	7.12125711598618E+04	1.76155822073721E+01
a_4	-6.48907410098701E+01	-3.30491167052668E+01	-2.96796397060977E+05	-1.96096765470814E+01
a_3	4.90311187858117E+01	2.69490135500644E+01	8.90809205667305E+05	1.56667315641923E+01
a_2	-2.32888796937463E+01	-1.42413754887764E+01	-1.81382736757085E+06	-8.94579854442243E+00
a_1	7.50645624360757E+00	5.57583257139493E+00	2.24195271112227E+06	4.39804082518896E+00
a_0	5.17008262248863E-02	2.95257563410426E-01	-1.26991681840798E+06	-3.86012635387946E-01
dev_{max} (mm)	23.564E-03	26.289E-03	30.831E-03	6.276E-03
Range (mm)	0 < z < 16.26	0 < z < 17.44	0 < z < 13.23	0 < z < 13.63

Table. A.1 Interface data of clean and contaminated bubbles shown in Fig. 6.5 - continued

$r_b(mm) = a_{20}z^{20} + a_{19}z^{19} + a_{18}z^{18} + a_{17}z^{17} + a_{16}z^{16} + a_{15}z^{15} + a_{14}z^{14} + a_{13}z^{13} + a_{12}z^{12} + a_{11}z^{11} + a_{10}z^{10} + a_9z^9 + a_8z^8 + a_7z^7 + a_6z^6 + a_5z^5 + a_4z^4 + a_3z^3 + a_2z^2 + a_1z + a_0$				
Fig. 6.5	**c**		**d**	
Coefficients	clean	contaminated	clean	contaminated
a_{20}	-9.28490938485168E-12	-1.01434328117774E-13	-1.96162564918123E-10	-7.23032707255770E-11
a_{19}	1.00692242595437E-09	1.24620892054285E-11	1.82684052225316E-08	6.86686903388259E-09
a_{18}	-5.06033666141633E-08	-6.76563459146997E-10	-7.88300582193555E-07	-3.02216313119092E-07
a_{17}	1.56394818289759E-06	2.07302351349529E-08	2.09162559550479E-05	8.18008849976712E-06
a_{16}	-3.32652617137538E-05	-3.61043613000415E-07	-3.81892777550636E-04	-1.52398024842053E-04
a_{15}	5.16347455517094E-04	2.09749846591526E-06	5.08765168945583E-03	2.07243070546108E-03
a_{14}	-6.05192200977038E-03	6.56245746026938E-05	-5.11707564690741E-02	-2.12876251631979E-02
a_{13}	5.46715009566159E-02	-2.21106341793525E-03	3.96604594913592E-01	1.68615130059554E-01
a_{12}	-3.85201204590206E-01	3.71138639933171E-02	-2.39687763388989E+00	-1.04232301917009E+00
a_{11}	2.12859710186701E+00	-4.23694974201007E-01	1.13572362526264E+01	5.05769951254364E+00
a_{10}	-9.22992028905145E+00	3.54870279481066E+00	-4.22092606750818E+01	-1.92788203159149E+01
a_9	3.12774973888715E+01	-2.23483617660009E+01	1.22521420077338E+02	5.75131801475940E+01
a_8	-8.21160662086720E+01	1.05946798054380E+02	-2.75312334622842E+02	-1.33189307460022E+02
a_7	1.64743190156590E+02	-3.70932254599017E+02	4.72236070737528E+02	2.36356660630884E+02
a_6	-2.47590830307266E+02	9.09877723052316E+02	-6.05993490012971E+02	-3.15545428113227E+02
a_5	2.71128456666118E+02	-1.33755962168544E+03	5.65802220024633E+02	3.09101449998095E+02
a_4	-2.08268420690747E+02	2.95062925783911E+02	-3.70140056760340E+02	-2.14998106797008E+02
a_3	1.06720705365266E+02	3.40608174007099E+03	1.61525294681252E+02	1.01960700300075E+02
a_2	-3.47140544416797E+01	-7.63980230100507E+03	-4.48383093533255E+01	-3.19005160104310E+01
a_1	8.07304594773088E+00	7.53855559015673E+03	8.93996280674196E+00	7.53987096238963E+00
a_0	1.29681757737575E-02	-3.01984486243346E+03	1.79899165500136E-01	6.59533685673801E-02
dev_{max} **(mm)**	8.990E-03	10.942E-03	9.516E-03	13.929E-03
Range (mm)	0 < z < 10.86	0 < z < 11.59	0 < z < 9.33	0 < z < 10.55

List of figures

List of tables

References

[1]   M. T. Kreutzer, F. Kapteijn, J. A. Moulijn, and J. J. Heiszwolf, "Multiphase monolith reactors: chemical reaction engineering of segmented flow in microchannels," *Chem. Eng. Sci.*, vol. 60, pp. 5895–5916, 2005.

[2]   S. Boden, T. Dos Santos Rolo, T. Baumbach, and U. Hampel, "Synchrotron radiation microtomography of Taylor bubbles in capillary two-phase flow," *Exp. Fluids*, vol. 55, 2014.

[3]   C. Yao, Z. Dong, Y. Zhao, and G. Chen, "Gas-liquid flow and mass transfer in a microchannel under elevated pressures," *Chem. Eng. Sci.*, vol. 123, pp. 137–145, 2015.

[4]   V. Hessel, P. Angeli, A. Gavriilidis, and H. Löwe, "Gas and liquid and gas and liquid and solid microstructured reactors: contacting principles and applications," *Ind. Eng. Chem. Res.*, vol. 44, pp. 9750–9769, 2005.

[5]   S. Nogueira, M. L. Riethmuller, J. B. L. M. Campos, and A. M. F. R. Pinto, "Flow patterns in the wake of a Taylor bubble rising through vertical columns of stagnant and flowing Newtonian liquids: An experimental study," *Chem. Eng. Sci.*, vol. 61, pp. 7199–7212, 2006.

[6]   J. C. Elliott and S. D. Dover, "X-ray microtomography," *J. Microsc.*, vol. 126, pp. 211–213, 1982.

[7]   S. Boden, M. Haghnegahdar, and U. Hampel, "Measurement of Taylor bubble shape in square channel by microfocus X-ray computed tomography for investigation of mass transfer," *Flow Meas. Instrum.*, vol. 53, pp. 49–55, 2017.

[8]   S. N. Kazi, *An Overview of Heat Transfer Phenomena*. Open access: InTech, 2012.

[9]   W. E. Adeney and A. R. C. Becker, "The determination of the rate of solution of atmospheric nitrogen and oxygen by water. Part I," *Phil. Mag.*, vol. 38, p. 317, 1919.

[10]   M. Filla, "Gas absorption from a slug held stationary in downflowing liquid," *Chem. Eng. J.*, vol. 22, pp. 213–220, 1981.

[11]   J. F. Davidson and F. A. Kirk, "Holding a bubble fixed by downward flow," *Chem. Eng. Sci.*, vol. 24, pp. 1529–1530, 1969.

References

[12] M. H. I. Baird and J. F. Davidson, "Gas absorption by large rising bubbles," *Chem. Eng. Sci.*, vol. 17, pp. 87–93, 1962.

[13] K. Koide, Y. Orito, and Y. Hara, "Mass transfer from single bubbles in Newtonian liquids," *Chem. Eng. Sci.*, vol. 29, pp. 417–425, 1974.

[14] P. H. Calderbank, D. S. L. Johnson, and J. Loudon, "Mechanics and mass transfer of single bubbles in free rise through some Newtonian and non-Newtonian liquids," *Chem. Eng. Sci.*, vol. 25, pp. 235–256, 1970.

[15] J. W. van Heuven and W. J. Beek, "Gas absorption in narrow gas lifts," *Chem. Eng. Sci.*, vol. 18, pp. 377–389, 1963.

[16] K. Niranjan, M. A. Hashim, A. B. Pandit, and J. F. Davidson, "Liquid-phase controlled mass transfer from a gas slug," *Chem. Eng. Sci.* , vol. 43, pp. 1247–1252, 1988.

[17] J. A. Redfield and G. Houghton, "Mass transfer and drag coefficients for single bubbles at reynolds numbers of 0.02-5000," *Chem. Eng. Sci.*, vol. 20, pp. 131–139, 1965.

[18] G. Schulze and E. U. Schlünder, "Physical absorption of single gas bubbles in degassed and preloaded water," *Chem. Eng. Process.*, vol. 19, pp. 27–37, 1985.

[19] K. Tsuchiya, H. Mikasa, and T. Saito, "Absorption dynamics of CO2 bubbles in a pressurized liquid flowing downward and its simulation in seawater," *Chem. Eng. Sci.* , vol. 52, pp. 4119–4126, 1997.

[20] F. Takemura and A. Yabe, "Rising speed and dissolution rate of a carbon dioxide bubble in slightly contaminated water," *J. Fluid Mech.*, vol. 378, pp. 319–334, 1999.

[21] K. Tsuchiya, M. Koshihata, T. Tomida, and T. Saito, "Effect of satellite bubbles on dynamics of gas absorption from a CO2 bubble into a downward-flowing liquid," *Korean J. Chem. Eng.*, vol. 16, pp. 635–639, 1999.

[22] F. Takemura and Y. Matsumoto, "Dissolution rate of spherical carbon dioxide bubbles in strong alkaline solutions," *Chem. Eng. Sci.*, vol. 55, pp. 3907–3917, 2000.

[23] J. M. T. Vasconcelos, S. P. Orvalho, and S. S. Alves, "Gas–liquid mass transfer to single bubbles: Effect of surface contamination," *AIChE J.*, vol. 48, pp. 1145–1154, 2002.

[24] S. Abe, H. Okawa, S. Hosokawa, and A. Tomiyama, "Dissolution of a carbon dioxide bubble

132

in a vertical pipe," *J. Fluid Sci. Technol.*, vol. 3, pp. 667–677, 2008.

[25]   A. A. Donaldson, A. Macchi, and D. M. Kirpalani, "Predicting inter-phase mass transfer for idealized Taylor flow: A comparison of numerical frameworks," *Chem. Eng. Sci.*, vol. 66, pp. 3339–3349, 2011.

[26]   A. Kundu, J. K. Basu, and G. Das, "A novel gas liquid contactor for chemisorption of CO2," *Sep. Purif. Technol.* , vol. 94, pp. 115–123, 2012.

[27]   M. Jimenez, N. Dietrich, and G. Hébrard, "Mass transfer in the wake of non-spherical air bubbles quantified by quenching of fluorescence," *Chem. Eng. Sci.*, vol. 100, pp. 160–171, 2013.

[28]   S. Hosoda, S. Abe, S. Hosokawa, and A. Tomiyama, "Mass transfer from a bubble in a vertical pipe," *Int. J. Heat Mass Transf.*, vol. 69, pp. 215–222, 2014.

[29]   J. Aoki, K. Hayashi, and A. Tomiyama, "Mass transfer from single carbon dioxide bubbles in contaminated water in a vertical pipe," *Int. J. Heat Mass Transf.*, vol. 83, pp. 652–658, 2015.

[30]   C. O. Vandu, H. Liu, and R. Krishna, "Mass transfer from Taylor bubbles rising in single capillaries," *Chem. Eng. Sci.* , vol. 60, pp. 6430–6437, 2005.

[31]   T. Taha and Z. F. Cui, "CFD modelling of slug flow inside square capillaries," *Chem. Eng. Sci.*, vol. 61, pp. 665–675, 2006.

[32]   W. B. Kolb and R. L. Cerro, "Coating the inside of a capillary of square cross section ," *Chem. Eng. Sci.* , vol. 46, pp. 2181–2195, 1991.

[33]   T. C. Thulasidas, M. A. Abraham, and R. L. Cerro, "Bubble-train flow in capillaries of circular and square cross section," *Chem. Eng. Sci.*, vol. 50, pp. 183–199, 1995.

[34]   T. C. Thulasidas, M. A. Abraham, and R. L. Cerro, "Flow patterns in liquid slugs during bubble-train flow inside capillaries," *Chem. Eng. Sci.*, vol. 52, pp. 2947–2962, 1997.

[35]   D. M. Fries, F. Trachsel, and P. R. von Rohr, "Segmented gas–liquid flow characterization in rectangular microchannels," *Int. J. Multiph. Flow*, vol. 34, pp. 1108–1118, 2008.

[36]   A. Kuzmin, M. Januszewski, D. Eskin, F. Mostowfi, and J. J. Derksen, "Three-dimensional binary-liquid lattice Boltzmann simulation of microchannels with rectangular cross sections," *Chem. Eng. J.*, vol. 178, pp. 306–316, 2011.

[37] A. L. Hazel and M. Heil, "The steady propagation of a semi-infinite bubble into a tube of elliptical or rectangular cross-section," *J. Fluid Mech.*, vol. 470, pp. 91–114, 2002.

[38] J. M. van Baten and R. Krishna, "CFD simulations of mass transfer from Taylor bubbles rising in circular capillaries," *Chem. Eng. Sci.* , vol. 59, pp. 2535–2545, 2004.

[39] N. Dietrich, K. Loubière, M. Jimenez, G. Hébrard, and C. Gourdon, "A new direct technique for visualizing and measuring gas–liquid mass transfer around bubbles moving in a straight millimetric square channel," *Chem. Eng. Sci.*, vol. 100, pp. 172–182, 2013.

[40] J. Yue, L. Luo, Y. Gonthier, G. Chen, and Q. Yuan, "An experimental study of air water Taylor flow and mass transfer inside square microchannels," *Chem. Eng. Sci.* , vol. 64, pp. 3697–3708, 2009.

[41] D. Bothe and J. Prüss, "Stability of equilibria for two-phase flows with soluble surfactant," *Q. J. Mech. Appl. Math.*, vol. 63, pp. 177–199, 2010.

[42] M. E. Weber, "The effect of surface active agents on mass transfer from spherical cap bubbles," *Chem. Eng. Sci.*, vol. 30, pp. 1507–1510, 1975.

[43] S. Sadhal and R. Johnson, "Stokes flow past bubbles and drops partially coated with thin films. Part 1. Stagnant cap of surfactant film- exact solution," *J. Fluid Mech.*, vol. 126, pp. 237–250, 1983.

[44] A. Dani, "Direct numerical simulation of mass transfer from spherical bubbles : the effect of interface contamination at low Reynolds numbers," *Int. J. Chem. React. Eng.*, vol. 4, pp. 1–21, 2006.

[45] M. Muradoglu and G. Tryggvason, "A front-tracking method for computation of interfacial flows with soluble surfactants," *J. Comput. Phys.*, vol. 227, pp. 2238–2262, 2008.

[46] R. Clift, J. Grace, and M. Weber, *Bubbles, drops, and particles*. New York: Academic Press, 1978.

[47] S. Tasoglu, U. Demirci, and M. Muradoglu, "The effect of soluble surfactant on the transient motion of a buoyancy-driven bubble," *Phys. Fluids*, vol. 20, pp. 17–20, 2008.

[48] B. Cuenot, J. Magnaudet, and B. Spennato, "The effects of slightly soluble surfactants on the flow around a spherical bubble," *J. Fluid Mech.*, vol. 339, pp. 25–53, 1997.

[49]   K. Hayashi and A. Tomiyama, "Effects of surfactant on terminal velocity of a Taylor bubble in a vertical pipe," *Int. J. Multiph. Flow*, vol. 39, pp. 78–87, 2012.

[50]   S. N. Ghadiali and D. P. Gaver, "The influence of non-equilibrium surfactant dynamics on the flow of a semi-infinite bubble in a rigid cylindrical capillary tube," *J. Fluid Mech.*, vol. 478, pp. 165–196, 2003.

[51]   G. M. Ginley and C. J. Radke, "Influence of soluble surfactants on the flow of long bubbles through a cylindrical capillary," *ACS Symp. Ser. 396*, pp. 480–501, 1989.

[52]   J. Ratulowski and H.-C. Chang, "Marangoni effects of trace impurities on the motion of long gas bubbles in capillaries," *J. Fluid Mech.*, vol. 210, pp. 303–328, 1990.

[53]   K. J. Stebe and D. Barthès-Biesel, "Marangoni effects of adsorption-desorption controlled surfactants on the leading end of an infinitely long bubble in a capillary," *J. Fluid Mech.*, vol. 286, pp. 25–48, 1995.

[54]   C.-W. Park, "Influence of soluble surfactants on the motion of a finite bubble in a capillary tube," *Phys. Fluids A Fluid Dyn.*, vol. 4, pp. 2335–2347, 1992.

[55]   P. Daripa and G. Pasa, "The effect of surfactant on long bubbles rising in vertical capillary tubes," *J. Stat. Mech. Theory Exp.*, vol. 2011, p. L02003, 2011.

[56]   P. Daripa and G. Pasa, "The effect of surfactant on the motion of long bubbles in horizontal capillary tubes," *J. Stat. Mech. Theory Exp.*, vol. 2010, p. L02002, 2010.

[57]   U. Olgac and M. Muradoglu, "Effects of surfactant on liquid film thickness in the Bretherton problem," *Int. J. Multiph. Flow*, vol. 48, pp. 58–70, 2013.

[58]   K. H. Mancy and D. A. Okun, "Effects of surface active agents on bubble aeration," *Water Pollut. Control Fed.*, vol. 32, pp. 351–364, 1960.

[59]   R. M. Griffith, "The effect of surfactants on the terminal velocity of drops and bubbles," *Chem. Eng. Sci.*, vol. 17, pp. 1057–1070, 1962.

[60]   D. R. Raymond and S. A. Zieminski, "Mass transfer and drag coefficients of bubbles rising in dilute aqueous solutions," *AIChE J.*, vol. 17, pp. 57–65, 1971.

[61]   G. Vázquez, M. a. Cancela, R. Varela, E. Alvarez, and J. M. Navaza, "Influence of surfactants on absorption of CO_2 in a stirred tank with and without bubbling," *Chem. Eng. J.*, vol. 67, pp.

References

131–137, 1997.

[62] G. Vázquez, M. Cancela, C. Riverol, E. Alvarez, and J. Navaza, "Application of the Danckwerts method in a bubble column," *Chem. Eng. J.*, vol. 78, pp. 13–19, 2000.

[63] J. M. T. Vasconcelos, J. M. L. Rodrigues, S. C. P. Orvalho, S. S. Alves, R. L. Mendes, and A. Reis, "Effect of contaminants on mass transfer coefficients in bubble column and airlift contactors," *Chem. Eng. Sci.*, vol. 58, pp. 1431–1440, 2003.

[64] K. Loubière and G. Hébrard, "Influence of liquid surface tension (surfactants) on bubble formation at rigid and flexible orifices," *Chem. Eng. Process. Process Intensif.*, vol. 43, pp. 1361–1369, 2004.

[65] S. S. Alves, S. P. Orvalho, and J. M. T. Vasconcelos, "Effect of bubble contamination on rise velocity and mass transfer," *Chem. Eng. Sci.*, vol. 60, pp. 1–9, 2005.

[66] S. S. Alves, C. I. Maia, and J. M. T. Vasconcelos, "Gas-liquid mass transfer coefficient in stirred tanks interpreted through bubble contamination kinetics," *Chem. Eng. Process. Process Intensif.*, vol. 43, pp. 823–830, 2004.

[67] E. Almatroushi and A. Borhan, "Surfactant effect on the buoyancy-driven motion of bubbles and drops in a tube," *Ann. N. Y. Acad. Sci.*, vol. 1027, pp. 330–341, 2004.

[68] P. Painmanakul, K. Loubière, G. Hébrard, M. Mietton-Peuchot, and M. Roustan, "Effect of surfactants on liquid-side mass transfer coefficients," *Chem. Eng. Sci.*, vol. 60, pp. 6480–6491, 2005.

[69] R. Sardeing, P. Painmanakul, and G. Hébrard, "Effect of surfactants on liquid-side mass transfer coefficients in gas–liquid systems: A first step to modeling," *Chem. Eng. Sci.*, vol. 61, pp. 6249–6260, 2006.

[70] D. Rosso, D. L. Huo, and M. K. Stenstrom, "Effects of interfacial surfactant contamination on bubble gas transfer," *Chem. Eng. Sci.*, vol. 61, pp. 5500–5514, 2006.

[71] N. J. English and S. G. Kandlikar, "An experimental investigation into the effect of surfactants on air-water two-phase flow in minichannels," *Heat Transf. Eng.*, vol. 27, pp. 99–109, 2006.

[72] N. J. English and S. G. Kandlikar, "An experimental investigation into the effect of surfactants on air-water two-phase flow in minichannels," in *Third International Conference on*

136

Microchannels and Minichannels, 2005, pp. 1–10.

[73] S. Takagi, T. Ogasawara, M. Fukuta, and Y. Matsumoto, "Surfactant effect on the bubble motions and bubbly flow structures in a vertical channel," *Fluid Dyn. Res.*, vol. 41, p. 65003, 2009.

[74] G. Hebrard, J. Zeng, and K. Loubiere, "Effect of surfactants on liquid side mass transfer coefficients: A new insight," *Chem. Eng. J.*, vol. 148, pp. 132–138, 2009.

[75] M. Jamnongwong, K. Loubiere, N. Dietrich, and G. Hébrard, "Experimental study of oxygen diffusion coefficients in clean water containing salt, glucose or surfactant: Consequences on the liquid-side mass transfer coefficients," *Chem. Eng. J.*, vol. 165, pp. 758–768, 2010.

[76] S. Takagi and Y. Matsumoto, "Surfactant effects on bubble motion and bubbly flows," *Annu. Rev. Fluid Mech.*, vol. 43, pp. 615–636, 2011.

[77] D. D. McClure, A. C. Lee, J. M. Kavanagh, D. F. Fletcher, and G. W. Barton, "Impact of surfactant addition on oxygen mass transfer in a bubble column," *Chem. Eng. Technol.*, vol. 38, pp. 44–52, 2015.

[78] J. Huang and T. Saito, "Influence of bubble-surface contamination on instantaneous mass transfer," *Chem. Eng. Technol.*, vol. 38, pp. 1947–1954, 2015.

[79] J. Aoki, K. Hayashi, S. Hosokawa, and A. Tomiyama, "Effects of surfactants on mass transfer from single carbon dioxide bubbles in vertical pipes," *Chem. Eng. Technol.*, vol. 38, pp. 1955–1964, 2015.

[80] R. Krechetnikov and G. M. Homsy, "Experimental study of substrate roughness and surfactant effects on the Landau-Levich law," *Phys. Fluids*, vol. 17, p. 102108, 2005.

[81] Z. Dong, C. Yao, Y. Zhang, G. Chen, Q. Yuan, and J. Xu, "Hydrodynamics and Mass Transfer of Oscillating Gas-Liquid Flow in Ultrasonic Microreactors," *AIChE J.*, vol. 62, pp. 1294–1307, 2016.

[82] Y. Yao, "Enhanceinent of mass transfer by ultrasound Application to adsorbent regeneration and food drying dehydration," *Ultrason. Sonochem.*, vol. 31, pp. 512–531, 2016.

[83] K. L. Harbaum and G. Houghton, "Effects of sonic vibrations on the rate of absorption of gases from bubble beds," *Chem. Eng. Sci.*, vol. 13, pp. 90–92, 1960.

References

[84] M. J. Jaeger and U. H. Kurzweg, "Determination of the longitudinal dispersion coefficient in flows subjected to high-frequency oscillations," *Phys. Fluids*, vol. 26, pp. 1380–1382, 1983.

[85] D. Brannock and J. Kubie, "Velocity of long bubbles in oscillating vertical pipes," *Int. J. Multiph. Flow*, vol. 22, pp. 1031–1034, 1996.

[86] S. Madani, O. Caballina, and M. Souhar, "Unsteady dynamics of Taylor bubble rising in vertical oscillating tubes," *Int. J. Multiph. Flow*, vol. 35, pp. 363–375, 2009.

[87] J. Kubie, "Velocity of long bubbles in horizontally oscillating vertical pipes," *Int. J. Multiph. Flow*, vol. 26, pp. 339–349, 2000.

[88] R. Krishna and J. Ellenberger, "Improving gas-liquid contacting in bubble columns by vibration excitement," *Int. J. Multiph. Flow*, vol. 28, pp. 1223–1234, 2002.

[89] J. Ellenberger and R. Krishna, "Improving mass transfer in gas – liquid dispersions by vibration excitement," *Chem. Eng. Sci.*, vol. 57, pp. 4809–4815, 2002.

[90] R. Krishna and J. Ellenberger, "Influence of low-frequency vibrations on bubble and drop sizes formed at a single orifice," *Chem. Eng. Process.*, vol. 42, pp. 15–21, 2003.

[91] J. Ellenberger, J. M. Van Baten, and R. Krishna, "Intensification of bubble columns by vibration excitement," *Catal. Today*, vol. 79–80, pp. 181–188, 2003.

[92] J. Ellenberger and R. Krishna, "Shaken, not stirred, bubble column reactors: Enhancement of mass transfer by vibration excitement," *Chem. Eng. Sci.*, vol. 58, pp. 705–710, 2003.

[93] C. M. Dillon, S. M. Ghiaasiaan, S. I. Abdel-Khalik, S. M. Jeter, and D. L. Sadowski, "Two-phase pressure drop in a horizontal thin annulus: Effects of channel vibration and wall gas injection," *Exp. Therm. Fluid Sci.*, vol. 30, pp. 67–78, 2005.

[94] C. O. Vandu, J. Ellenberger, and R. Krishna, "Hydrodynamics and mass, transfer in an upflow monolith loop reactor," *Chem. Eng. Process. Process Intensif.*, vol. 44, pp. 363–374, 2005.

[95] A. Hashmi, G. Yu, M. Reilly-Collette, G. Heiman, and J. Xu, "Oscillating bubbles: a versatile tool for lab on a chip applications.," *Lab Chip*, vol. 12, pp. 4216–4227, 2012.

[96] D. Fernandez Rivas, P. Cintas, and H. J. G. E. Gardeniers, "Merging microfluidics and sonochemistry: towards greener and more efficient micro-sono-reactors," *Chem. Commun.*, vol. 48, p. 10935, 2012.

138

[97]   D. Polezhaev, P. Duru, and F. Plouraboué, "Enhanced evaporation from an oscillating liquid in a capillary tube," *Int. J. Heat Mass Transf.*, vol. 95, pp. 288–295, 2016.

[98]   Z. Dong *et al.*, "A high-power ultrasonic microreactor and its application in gas–liquid mass transfer intensification," *Lab Chip*, vol. 15, pp. 1145–1152, 2015.

[99]   F. Fairbrother and A. E. Stubb, "Studies in Electro-endosmosis, Part VI. The bubble-tube method of measurement," *J. Chem. Soc.*, vol. 1, pp. 527–529, 1935.

[100]   G. I. Taylor, "Deposition of a viscous fluid on the wall of a tube," *J. Fluid Mech.*, vol. 10, pp. 161–165, 1961.

[101]   R. N. Marchessault and S. G. Mason, "Flow of entrapped bubbles through a capillary," *Ind. Eng. Chem. Res.*, vol. 52, pp. 79–84, 1960.

[102]   F. P. Bretherton, "The motion of long bubbles in tubes," *J. Fluid Mech.*, vol. 10, pp. 166–188, 1961.

[103]   a Karnis, H. L. Goldsmith, and S. G. Mason, "The flow of suspensions through tubes: V. Inertial effects," *Can. J. Chem. Eng.*, vol. 44, pp. 181–193, 1966.

[104]   G. F. Teletzke, "Thin liquid films: Molecular theory and hydrodynamic implications," University of Minnesota, 1983.

[105]   S. Irandoust and B. Andersson, "Liquid film in Taylor flow through a capillary," *Ind. Eng. Chem. Res.*, vol. 28, pp. 1684–1688, 1989.

[106]   P. Aussillous and D. Quéré, "Quick deposition of a fluid on the wall of a tube," *Phys. Fluids*, vol. 12, pp. 2367–2371, 2000.

[107]   M. T. Kreutzer, F. Kapteijn, J. A. Moulijn, C. R. Kleijn, and J. J. Heiszwolf, "Inertial and interfacial effects on pressure drop of Taylor flow in capillaries," *AIChE J.*, vol. 51, pp. 2428–2440, 2005.

[108]   M. Heil, "Finite Reynolds number effects in the Bretherton problem," *Phys. Fluids*, vol. 13, pp. 2517–2521, 2001.

[109]   Y. Han and N. Shikazono, "Measurement of the liquid film thickness in micro tube slug flow," *Int. J. Heat Fluid Flow*, vol. 30, pp. 842–853, 2009.

[110]   Y. J. Youn, K. Muramatsu, Y. Han, and N. Shikazono, "The effect of initial flow velocity on

References

the liquid film thickness in micro tube accelerated slug flow," *Int. J. Multiph. Flow*, vol. 73, pp. 108–117, 2015.

[111] A. K. Singhal and W. H. Somerton, "Two-phase flow through a non-circular capillary at low Reynolds numbers," *J. Can. Pet. Technol.*, vol. 9, p. 197, 1970.

[112] Y. Han and N. Shikazono, "Measurement of liquid film thickness in micro square channel," *Int. J. Multiph. Flow*, vol. 35, pp. 896–903, 2009.

[113] Y. Chaoqun, Z. Yuchao, Y. Chunbo, D. Minhui, D. Zhengya, and C. Guangwen, "Characteristics of slug flow with inertial effects in a rectangular microchannel," *Chem. Eng. Sci.*, vol. 95, pp. 246–256, 2013.

[114] M. J. F. Warnier, E. V Rebrov, M. H. J. M. de Croon, V. Hessel, and J. C. Schouten, "Gas hold-up and liquid film thickness in Taylor flow in rectangular microchannels," *Chem. Eng. J.*, vol. 135, Suppl, pp. S153–S158, 2008.

[115] L. a. Feldkamp, L. C. Davis, and J. W. Kress, "Practical cone-beam algorithm," *J. Opt. Soc. Am. A*, vol. 1, pp. 612–619, 1984.

[116] E. T. White and R. H. Beardmore, "The velocity of rise of single cylindrical air bubbles through liquids contained in vertical tubes," *Chem. Eng. Sci.*, vol. 17, pp. 351–361, 1962.

[117] P. H. Calderbank and A. C. Lochiel, "Mass transfer coefficients, velocities and shapes of carbon dioxide bubbles in free rise through distilled water," *Chem. Eng. Sci.*, vol. 19, pp. 485–503, 1964.

[118] R. M. Griffith, "Mass transfer from drops and bubbles," *Chem. Eng. Sci.*, vol. 12, pp. 198–213, 1960.

[119] R. Higbie, "The rate of absorption of a pure gas into a still liquid during short periods of exposure," *Transactions of the American Institute of Chemical Engineers*, vol. 31. pp. 365–389, 1935.

[120] R. E. Treybal, *Mass Transfer Operations*, Third Ed. New York: McGraw-Hill, 1980.

[121] R. B. Bird, W. E. Stewart, and E. N. Lightfood, *Transport Phenomena*, Second Ed. John Wiley and Sons Inc., 2002.

[122] J. R. Thome, V. Dupont, and A. M. Jacobi, "Heat transfer model for evaporation in

microchannels. Part I: Presentation of the model," *Int. J. Heat Mass Transf.*, vol. 47, pp. 3375–3385, 2004.

[123] Y. Han and N. Shikazono, "The effect of bubble acceleration on the liquid film thickness in micro tubes," *Int. J. Heat Fluid Flow*, vol. 31, pp. 630–639, 2010.

[124] M. M. G. Eain, V. Egan, and J. Punch, "Film thickness measurements in liquid–liquid slug flow regimes," *Int. J. Heat Fluid Flow*, vol. 44, pp. 515–523, 2013.

[125] J. A. Howard and P. A. Walsh, "Review and extensions to film thickness and relative bubble drift velocity prediction methods in laminar Taylor or slug flows ," *Int. J. Multiph. Flow* , vol. 55, pp. 32–42, 2013.

[126] S. Boden, M. Haghnegahdar, and U. Hampel, "X-ray microtomography of Taylor bubbles with mass transfer and surfactants in capillary twophase flow," in *Advances in Mathematical Fluid Mechanics*, Basel: Springer International Publishing AG, 2017, pp. 589–608.

[127] J. Ratulowski and H. Chang, "Transport of gas bubbles in capillaries," *Phys. Fluids A Fluid Dyn.*, vol. 1, pp. 1642–1655, 1989.

[128] T. Hazuku, N. Fukamachi, T. Takamasa, T. Hibiki, and M. Ishii, "Measurement of liquid film in microchannels using a laser focus displacement meter," *Exp. Fluids*, vol. 38, pp. 780–788, 2005.

[129] T. Takamasa and K. Kobayashi, "Measuring interfacial waves on film flowing down tube inner wall using laser focus displacement meter," *Int. J. Multiph. Flow*, vol. 26, pp. 1493–1507, 2000.

[130] R. Kurimoto, K. Hayashi, and A. Tomiyama, "Terminal velocities of clean and fully-contaminated drops in vertical pipes," *Int. J. Multiph. Flow*, vol. 49, pp. 8–23, 2013.

[131] P. Daripa and G. Paşa, "The thickening effect of interfacial surfactant in the drag-out coating problem," *J. Stat. Mech. Theory Exp.*, vol. 2009, p. L07002, 2009.

[132] T. N. Swaminathan, K. Mukundakrishnan, P. S. Ayyaswamy, and D. M. Eckmann, "Effect of a soluble surfactant on a finite sized bubble motion in a blood vessel," *J. Fluid Mech.*, vol. 642, pp. 509–539, 2010.

[133] A. Q. Shen, B. Gleason, G. H. McKinley, and H. A. Stone, "Fiber coating with surfactant

solutions," *Phys. Fluids*, vol. 14, pp. 4055–4068, 2002.

[134] L.-H. Chen and Y.-L. Lee, "Adsorption behavior of surfactants and mass transfer in single-drop extraction," *AIChE J.*, vol. 46, pp. 160–168, 2000.

[135] Y. L. Lee, "Surfactants effects on mass transfer during drop-formation and drop falling stages," *AIChE J.*, vol. 49, pp. 1859–1869, 2003.

[136] S. Y. Lin, K. McKeigue, and C. Maldarelli, "Diffusion controlled surfactant adsorption studied by pendant drop digitisation," vol. 36, pp. 1785–1795, 1990.

[137] K. J. Stebe, S. Y. Lin, and C. Maldarelli, "Remobilizing surfactant retarded fluid particle interfaces. 1. Stress-free conditions at the interfaces of micellar solutions of surfactants with fast sorption kinetics," *Phys. Fluids A-Fluid Dyn.*, vol. 3, pp. 3–20, 1991.

[138] K. J. Stebe and C. Maldarelli, "Remobilizing surfactant retarded fluid particle interfaces," *J. Colloid Interface Sci.*, vol. 163, pp. 177–189, 1994.

[139] M. Haghnegahdar, S. Boden, and U. Hampel, "Mass transfer measurement in a square milli-channel and comparison with results from a circular channel," *Int. J. Heat Mass Transf.*, vol. 101, pp. 251–260, 2016.

[140] M. Haghnegahdar, S. Boden, and U. Hampel, "Investigation of surfactant effect on the bubble shape and mass transfer in a milli-channel using high-resolution microfocus X-ray imaging," *Int. J. Multiph. Flow*, vol. 87, pp. 184–196, 2016.

[141] M. Haghnegahdar, S. Boden, and U. Hampel, "Investigation of mass transfer in milli-channels using high-resolution microfocus X-ray imaging," *Int. J. Heat Mass Transf.*, vol. 93, pp. 653–664, 2016.

List of publications

Peer-reviewed articles

Haghnegahdar, Mohammadreza, Stephan Boden, and Uwe Hampel. 2017. "Experimental analysis of Taylor bubble behavior and mass transfer during lateral oscillation of a vertical milli-channel." Chemical Engineering Journal 326:308–17.

Boden, Stephan, **Mohammadreza Haghnegahdar**, and Uwe Hampel. 2017a. "Measurement of Taylor bubble shape in square channel by microfocus X-ray computed tomography for investigation of mass transfer." Flow Measurement and Instrumentation 53:49–55.

Boden, Stephan, **Mohammadreza Haghnegahdar**, and Uwe Hampel. 2017b. "X-Ray microtomography of Taylor bubbles with mass transfer and surfactants in capillary two-phase flow." Advances in Mathematical Fluid Mechanics Basel: Springer, 589-608.

Haghnegahdar, Mohammadreza, Stephan Boden, and Uwe Hampel. 2016a. "Investigation of mass transfer in milli-channels using high-resolution microfocus X-ray imaging." International Journal of Heat and Mass Transfer 93:653–64.

Haghnegahdar, Mohammadreza, Stephan Boden, and Uwe Hampel. 2016b. "Mass transfer measurement in a square milli-channel and comparison with results from a circular channel." International Journal of Heat and Mass Transfer 101:251–60.

Haghnegahdar, Mohammadreza, Stephan Boden, and Uwe Hampel. 2016c. "Investigation of surfactant effect on the bubble shape and mass transfer in a milli-channel using high-resolution microfocus X-ray imaging." International Journal of Multiphase Flow 87:184–96.

Oral presentations at conferences

Haghnegahdar, Mohammadreza, Stephan Boden, and Uwe Hampel. "Experimental study on the influence of horizontal channel vibration on the mass transfer rate of bubbles in milli-channels." GLS 13, Aug. 2017, Belgium.

Haghnegahdar, Mohammadreza, Stephan Boden, and Uwe Hampel. "Investigation of surfactant effect on the bubble shape and mass transfer in milli-channels." DEFI 2016, Oct. 2016, France.

Haghnegahdar, Mohammadreza, Stephan Boden, and Uwe Hampel. "Investigation of influence of channel vibration on the dissolution rate of single bubbles in milli-channels." CHISA 2016, Aug. 2016, Czech republic.

Haghnegahdar, Mohammadreza, Stephan Boden, and Uwe Hampel. "Experimental investigation of Taylor bubble dissolution in milli-channels." ICMF 2016, May, 2016, Italy.

Haghnegahdar, Mohammadreza, Stephan Boden, and Uwe Hampel. "Mass transfer measurement in a Square Milli-Channel using high-resolution microfocus X-ray imaging." International Conference Transport Processes at Fluidic Interfaces, Oct. 2015, Germany.

Poster presentations at conferences

Haghnegahdar, Mohammadreza, Stephan Boden, and Uwe Hampel. "Analysis of Taylor bubble motion during horizontal oscillation of vertical small channels." WCCE 10, Oct. 2017, Spain.

Haghnegahdar, Mohammadreza, Stephan Boden, and Uwe Hampel. "Experimental investigation on the influence of surfactant concentration on the bubble shape and mass transfer in a small channel." 14th multiphase flow conference, Nov. 2016, Germany.

Haghnegahdar, Mohammadreza, Stephan Boden, and Uwe Hampel. "Experimental study on the mass transfer of a CO_2 Taylor bubble using X-ray microfucos tomography." ECCE 10, Sep. 2015, France.

Boden, Stephan, **Mohammadreza Haghnegahdar**, and Uwe Hampel. "X-ray tomographic measurement of Taylor bubble shape for investigation of mass transfer." ISPT 7, Sep. 2015, Germany.

Further publications

Haghnegahdar, Mohammadreza, Mohammad Sadegh Hatamipour, and Amir Rahimi. 2011a. "Mathematical modeling of CO_2 capture in a semi-dry spouted bed reactor." Separation and Purification Technology 80(3):509–18.

Haghnegahdar, Mohammadreza, Amir Rahimi, and Mohammad Sadegh Hatamipour. 2011b. "A rate equation for $Ca(OH)_2$ and CO_2 reaction in a spouted bed reactor at low gas concentrations." Chemical Engineering Research and Design 89(6):616–20.

Rahimi, Amir, Mohammad Sadegh Hatamipour, Mohsen Gholami, and **Mohammadreza Haghnegahdar**. 2011c. "Non-isothermal modeling of the flue gas desulphurization process using a semi-dry spouted bed reactor." Chemical Engineering Research and Design 89(6):777–84.

Haghnegahdar, Mohammadreza, Mohammad Sadegh Hatamipour, and Amir Rahimi. 2010. "Removal of carbon dioxide in an experimental powder-particle spouted bed reactor." Separation and Purification Technology 72(3):288–93.